

University of Strathclyde

Department of Pure and Applied Chemistry

Plasmonic Metal Nanoparticles: Synthesis and Applications

By

Christopher R. Steven

A thesis presented to the Department of Pure and Applied
Chemistry in fulfilment of the requirements for the degree of
Doctor of Philosophy.

2017

This thesis is the result of the author's original research. It has been composed by the author and has not been previously submitted for examination which has led to the award of a degree.

The copyright of this thesis belongs to the author under the terms of the United Kingdom Copyright Acts as qualified by University of Strathclyde Regulation 3.50. Due acknowledgement must always be made of the use of any material contained in, or derived from, this thesis.

Signed:

Date:

Acknowledgements

First of all, I would like to thank my supervisors, Duncan Graham and Karen Faulds, for their guidance and supervision throughout the project. I would also like to express my gratitude for the opportunities they made available to collaborate with other researchers and visit other universities internationally.

Thanks go to BBI Solutions for funding the project and providing a much valued industrial perspective to the work. Thanks in particular to Stephen Carmichael, Steven Lamont, Darren Rowles and Nikki Robinson who were involved in various parts of the project.

I would like to extend my thanks to David Palmer for all his support with the computer simulation work, for his patience in helping me with the practical work and teaching me about this area of chemistry. I would also like to express my gratitude to Kwang W. Oh and his research group at SUNY-Buffalo. Their hosting of my visit to Buffalo and later assistance that they gave enabled my work on microfluidic systems.

I would like to acknowledge everyone in the Centre for Molecular Nanometrology who all helped me in my studies, contributed to the work in this thesis and created a great environment in which to study and do research. In particular I would like to mention Jonathan Simpson, for all his assistance with the lectin work and for always making time to help, and Lee Barrett, for all of his patience and guidance through trying to develop the binding induced DNA assembly assay.

Finally, I would like to thank Claire Forsyth for all her support throughout my PhD and in writing my thesis.

Abstract

Plasmonic metal nanoparticles are widely exploited in academia and industry for use in various assay types. In collaboration with an industrial partner, BBI Solutions, the work here details investigations into the production and use of the plasmonic nanoparticles. The work was split into two themes. The first of these was flow chemistry of nanoparticles, covering a microfluidic assay platform and continuous colloid production.

In chapter one, a novel microfluidic assay platform was developed which facilitated the transfer of multiple, sequential bench-top procedures into a single device. This allowed the rapid detection of a sugar binding protein to be demonstrated. The microfluidic system included all pre-detection steps involved in employing the specific aggregation of functionalised silver nanoparticles. Straightforward detection of the protein was demonstrated at concentrations lower than those achieved using comparable methods in the literature.

In the second chapter, a novel bench-top scale continuous reactor for the production of gold nanoparticles was developed. It was found that the continuous stirred tank reactor was generally unsuitable for this synthesis. A laminar tubular reactor was more successful but fouling of the reactor material was a significant obstacle to production of good quality colloid. In both cases, nanoparticles produced in a batch synthesis were of more consistent quality. This suggested that further work was needed to develop a competitive continuous production method.

The second research theme was development of a novel nanoparticle assembly assay, based on DNA assembly. In chapter three it was found that current tools for the understanding of dynamic DNA structure were limited. This led to the first use of an existing coarse grain model to determine thermodynamic properties of DNA assembly. Analysis showed that the results were comparable with the best simulation models shown in the literature, while being generated much more quickly and at less computational expense.

Table of Contents

1	Lab-on-a-Chip Plasmonic Detection of a Protein	
1.1	Abstract	1
1.2	Introduction	2
1.2.1	Microfluidics	3
1.2.1.1	Mixing in Microfluidic Devices	5
1.2.1.2	Transferring Reactions from Batch to Microreactors	12
1.2.1.3	Electrical Circuit Analogy for Device Design	13
1.2.2	Lectins	17
1.2.2.1	Carbohydrate Chemistry	20
1.2.2.2	Lectins and Microfluidics	22
1.2.3	Plasmonic Nanoparticles	22
1.2.3.1	Silver Nanoparticle Colloid Synthesis	24
1.2.4	Raman Scattering Assay for Lectin Detection	25
1.2.4.1	SERS and Microfluidics	27
1.2.5	Colourimetric Nanoparticle Assay for Lectin Detection	28
1.3	Aims	29
1.4	Results and Discussion	30
1.4.1	Microfluidic Design, Modelling and Testing	30
1.4.1.1	Design Basis of the Device and AutoCAD model	30
1.4.1.2	Modelling the Device using Electrical Circuit and COMSOL Simulation	34
1.4.1.3	Experimentally testing Flow Control and Mixing in the Device	48
1.4.2	Running the Device for Colloid Synthesis and PEG Conjugation	54
1.4.3	Raman Spectroscopy On-Chip	61
1.4.4	SERS Detection of ConA	66
1.4.5	Experimental Plasmonic Extinction Assay	68
1.5	Conclusions	75
1.6	Further work	77

1.7	Experimental	80
1.7.1	Reagents	80
1.7.2	Batch Nanoparticle Preparation	80
1.7.3	Carbohydrate Linker Preparation	80
1.7.4	Instrumental Analysis	82
1.7.5	Designing the Microfluidic Device	83
1.7.6	Running the Microfluidic Device	86
1.7.7	Fluorescence Imaging	87
1.7.8	Flow Ratio Test	87
1.8	Appendix A: Diffusion Mixing in the Microfluidic Device	89
1.9	Appendix B: Simulation of Fluid Flow through the SHM	91
1.10	Appendix C: Mixing in the SHM	102
1.11	References	104

2	Continuous Gold Colloid Production	
2.1	Abstract	114
2.2	Introduction	115
2.2.1	Gold Nanoparticle Production Methods	116
2.2.2	Measuring Nanoparticle Size	118
2.2.3	Continuous Gold Colloid Production in Literature	121
2.2.4	Reactor Configurations	124
2.2.4.1	Batch Reactors	125
2.2.4.2	Continuous Stirred Tank Reactor	126
2.2.4.3	Plug Flow Reactor	129
2.2.4.4	Laminar Tubular Reactor	131
2.3	Aims	133
2.4	Results and Discussion	134
2.4.1	Batch Production of Gold Colloid	134
2.4.1.1	Reducing Dissolved Oxygen Concentration and Colloid Quality	139
2.4.1.2	Extinction Spectroscopy for Small Colloids	143
2.4.2	Continuous Production	145
2.4.2.1	CSTR	145
2.4.2.2	Tubular Reactor	153
2.5	Conclusions	159
2.6	Future Work	161
2.7	Experimental	162
2.7.1	Chemicals and Characterisation	162
2.7.1.1	Solvents and Reagents	162
2.7.1.2	Extinction Spectroscopy	162
2.7.1.3	Dynamic Light Scattering Measurement	163
2.7.2	Batch Nanoparticle Synthesis	163
2.7.2.1	Citrate Reduced Nanoparticles	163
2.7.2.2	Borohydride Reduced Nanoparticles	163

2.7.2.3	Ascorbic Acid Grown Nanoparticles	164
2.7.2.4	BBI Colloid	164
2.7.3	Continuous Reactors	165
2.7.3.1	Citrate Reduction in a CSTR	165
2.7.3.2	Citrate Reduction in a CSTR- Longer Residence Time	165
2.7.3.3	Ascorbic Acid Growth in the CSTR	166
2.7.3.4	Ascorbic Acid Growth in a Tubular Reactor	166
2.7.3.5	Borohydride Reduction in a Tubular Reactor	167
2.7.3.6	BBI Colloid Reduction in a Tubular Reactor	167
2.7.4	Winkler Titration	167
2.8	References	168

3	Computer Simulation of a DNA Assembly Assay	
3.1	Abstract	174
3.2	Introduction	175
3.2.1	Simulation of DNA	178
3.2.2	Molecular Dynamics	179
3.2.3	Reducing Computational Requirements of Simulations	180
3.2.4	Determining Free Energy Change from Non-Equilibrium Simulations	183
3.2.5	Statistical Analysis	185
3.3	Aims	188
3.4	Results and Discussion	188
3.4.1	Changing the Pulled Group in SMD	193
3.4.2	Comparison with Experimental Data	198
3.4.3	Applying the 3SPN2 Model to the BINDA Assay	208
3.5	Conclusions	211
3.6	Future Work	212
3.7	Experimental	213
3.8	References	220

1 Lab-on-a-Chip

Plasmonic Detection of a Protein

1.1 Abstract

Flow chemistry and especially microfluidic systems can allow the performance of many simple lab functions, such as mixing, rapidly and efficiently on a lab-on-a-chip device. The ease of using these devices also reduces the operator input, making their use by non-specialists viable. To date, very few integrated systems have been developed that can perform sample preparation and analysis in a single lab-on-a-chip. The design of these devices can also be challenging and require extensive laboratory work.

In this chapter the development of a microfluidic system which could perform the detection of sugar binding proteins in solution is shown. The microfluidic system included all pre-detection steps involved in employing the specific aggregation of functionalised silver nanoparticles. Using an electrical circuit analogy, the system could be designed in circuit simulation software, reducing laboratory requirements and design costs. This design method also allowed stream splitting and mixing ratios to be specified at the design stage to match those developed in bench-top chemistry.

By monitoring the plasmon extinction of silver nanoparticles using off-line extinction spectroscopy, the detection of the proteins was facile at the point of use. Along with the design of the device, initial testing was demonstrated, proving its operability. Given the generic design principles and chemistry employed, the device could be employed in wide ranging analyses involving complex samples and multiple analytes.

1.2 Introduction

The use of microfluidics has grown greatly, especially in engineering and biomedical fields [1]. The technology allows experiments to be performed with accurate control over parameters, which can be difficult on a larger scale (fluid flow and heat transfer particularly). These experiments can be performed rapidly, efficiently and potentially cheaply.

Microfluidic lab-on-a-chip (LOC) type devices have been developed for a large variety of uses and can now encompass a number of traditional lab functions. The LOC concept is used to miniaturise a number of steps in a process and is used to replace bench-top procedures. This kind of microfluidic device is most widely used for analysis where sample preparation and analysis are combined on a single chip [2, 3]. This has the advantage of reducing reagent and analyte volumes required, automates the steps performed on the device and allows relatively complex analysis processes to be taken out of the traditional chemistry laboratory setting.

Work to employ the ability of microfluidics to take chemistry out of a traditional lab setting often focuses on the use of low-cost diagnostics, primarily paper microfluidics [4]. Recent developments to these technologies have greatly expanded the scope of chemistry performed on these devices [5, 6] but the capacity of these devices to completely replace the processes performed in a lab is limited. There is an apparent lack of devices which have developed the ability of LOC microfluidics to miniaturise and replace the most fundamental lab functions, in order to allow a full analysis to be performed on a microfluidic chip.

The LOC platform is one which, if properly applied to the challenges of a more decentralised model of analytical chemistry, can offer many advantages. The small footprint allows it to be transported and used easily, the low reagent requirements means including small reagent reservoirs for on-site testing is practical and, by employing solution phase chemistry, existing chemistry can be transferred to the new platform. Key challenges addressed here revolve around the central process of efficiently transferring chemistry into microfluidic devices. Due to limited mass

transfer in the small channels and poor control over stream mixing and combining ratios, current technologies often do not fully utilise the potential of the LOC platform, nor the existing technical solutions in the literature.

One particular class of analyte that would benefit from the advantages of such a LOC platform are lectins, a class of proteins which bind to carbohydrates. This is because lectins are key in many healthcare relevant targets which would benefit from rapid analysis results (e.g. cholera in water supplies, potential ricin in terrorist packages). In these examples, rapid reliable results are useful even when the quantification of results must be carried out at a later stage. The capability of detecting lectins rapidly by a non-specialist, in a resource limited environment is a useful addition to available analytical methods. Further to this, the sensitive, quantitative and rapid detection of these lectins in a traditional analytical laboratory setting, without requiring time consuming assay steps would also be a useful addition to the analytical chemistry toolset. Combining the capability to rapidly and sensitively detect lectins with the capacity for LOC to accelerate and simplify detection would therefore have great utility in both of these scenarios.

1.2.1 Microfluidics

Microfluidic devices are those which manipulate small scale fluid flow, typically this is done by containing fluid in channels between tens to hundreds of microns [7]. There are two main strands of research driving interest in these devices; the ability to facilitate the miniaturisation of a wide variety of chemical processes and the capacity to generate a platform for novel technologies. Their capabilities for developing new technologies has been widely explored in the biological sciences, e.g. where the size of the devices are a good match for the size of cells for trapping or for viability studies [8]. The focus of this project is on the former point, so there will be limited further information on the development of novel technological solutions based on microfluidic platforms.

Where miniaturisation can allow the development of a LOC, there are many advantages over bench-top chemistry. These are: a reduction in reagent consumption

and consequent waste generation, smaller overall footprint, reduced timescales (particularly where the LOC replaces sequential batch procedures), well defined reaction times and reduced operator requirements. For analytical procedures there are two main additional advantages: reduced sample requirements (a key feature when biological samples are being tested or sample is limited) and easy integration with existing optical detection methods. For this reason, microfluidics have found great use in both the high and low cost areas of analytical chemistry, more so than in other fields of chemistry, where the limitations of scale-up/ scale-out can hinder further development (compare 450 results on Web of Science for “microfluidics synthesis” and 2,350 for “microfluidics analytical”).

Numerous kinds of microfluidics exist for analytical applications, including paper devices bringing diagnostic tests to resource poor environments [6]; fluidic channel devices used for automated sampling e.g. in the Biacore system and digital microfluidics where discrete droplets can be handled and combined on an advanced instrument [9]. The area, therefore encompasses a huge variety of enabling technologies, so multiple potential solutions may be used solve a single problem.

In this chapter, the focus was on development of a device which was relatively easy to use and develop but which was capable of performing relatively complex chemistry. As outlined above, the paper type devices are among the most obvious technologies for this challenge but were discounted as having limited scope for facilitating chemical reactions on-device, despite being the easiest technology to use. Digital microfluidics and other types of novel microfluidic devices were also discounted as the required structure to control the flows through the device were relatively complex. However, these types of devices were extremely capable of reliable liquid dosing [10] and performing complex chemistry in an almost completely autonomous manner [11].

The most suitable type of microfluidic device to be taken forward for further consideration was the classical fluidic chip, where small micrometer scale channels are used to manipulate fluid flow. This is the closest to a direct analogue of flow

through pipelines and is the most intuitive to understand and apply. This type of device is the most widely applied but, for the objective of this work, presents two key challenges. These are overcoming the extremely laminar flow and translating batch chemistries into a lab-on-a-chip. In general, if these two challenges can be overcome then transition to a lab-on-a-chip should be possible with the numerous advantages outlined above.

1.2.1.1 Mixing in Microfluidic Devices

The first and most obvious problem in working with microreactors is the problem of mixing in microfluidic channels. This can be very slow, due to the laminar flow in the constrained dimensions and the very low flow rates. The Reynolds number (Re) gives the ratio of inertial to viscous forces in liquids; values in the single digits are common for microfluidics, well within the laminar flow regime, compared to 2000 for transition flow and in excess of 4000 for fully developed turbulent flow [12]. This means that without an external impetus for mixing, the two streams will remain in individual lamina with mixing only by molecular diffusion between them (a visual depiction of this is shown in figure 1.1). In this regime it would take a very long time (on the order of 10 -100 seconds) to obtain a homogeneous solution. This slow mixing can be a severe limitation for devices which are employed to carry out chemistry, as the reactions will be limited by how fast reactants can diffuse into one another. Practically this will limit the rate at which reactions can be completed on-chip, due to the limited channel lengths.



Figure 1.1: The cover of the journal Science from July 1999 showing an image of coloured laminae of fluid flowing through a microchannel with no mixing.

Reproduced from reference [13].

There are a large number of reports in the literature of various mixers in microfluidics, however these are often not fully exploited in reports of chemistry performed in LOC devices [14, 15] and many mixers exist encompassing a variety of mixing times. The possible strategies to facilitate mixing are extensive and far beyond the scope of this brief summary to comprehensively include. There are two alternatives for effective micromixing, termed passive and active [16]. The simpler of the two are passive mixers, which involve no additional external power and use only the inertia of the fluid as the driving force for mixing. These simple designs are the most widely used as they are relatively easily included in the design and add no additional complexity to the operation of the device. Active mixers, whilst undoubtedly effective, can add significant complexity to the design and use of a device and for this reason have not been included in this work.

The most basic mixer, the t-mixer, is often included in devices as the most practical solution for junctioning two streams together, but has also been evaluated as a mixer in its own right. Analysis of flow patterns generated by t-mixers indicated complex flow patterns which can reduce mixing effectiveness [17]. The t-mixer is included in the device designed here, as it is in most devices through the necessity of joining two

streams together. Whilst Re remains below 200, then the data from Dreher *et al.* indicate that the t-mixer does not operate as an effective mixing device. These results are summarised in figure 1.2 which shows a simulation of two fluids mixing after a t-mixer.

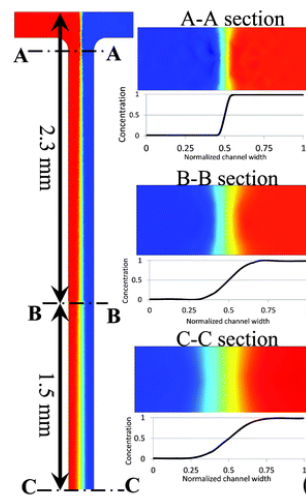


Figure 1.2: Flow pattern through a t-mixer at low Re , showing the mixing of a blue and red fluid. Reproduced from reference [18].

A second general strategy for creating conditions to improve mixing is to disrupt the flow of fluid down the microfluidic channel. In a macroscale pipeline, this would give small areas of turbulent flow or vortexing which mixes the liquid. In microfluidics, the extremely laminar flow can hamper this kind of mixing. Disruption can be facilitated by having a pillar block part of the channel [19], having a square wave pattern in the flow channel [20] or making a zig-zag channel [21] (images of these mixer types are shown in figures 1.3-1.5).

These have widely varying levels of success, with some designs reported not to enhance mixing significantly [20] to pillar arrays which are reported to improve mixing greatly over that from diffusion only [19]. The inclusion of a square wave pattern in the fluid stream did not cause any chaotic flow either by changing the path of the liquid around the pattern or by the swirl flow usually associated with rapid expansion/ contraction in a macroscale pipeline [22]. This is probably due to the very

low flow rates in the microfluidic system which means the flow pattern around the corners either involves only one side of the mixing boundary or creates dead zones of little or no flow in corners. This report of poorly enhanced mixing is supported by a further work using a square wave pattern [23] designed to operate on similar principles. Below a Reynolds number of 80, mixing was entirely by molecular diffusion.

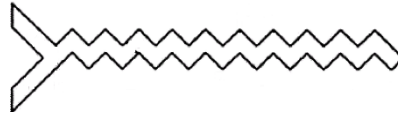


Figure 1.3: 2D drawing representation of a zig-zag mixing channel where two different fluids enter the channel at the entrances on the left. Reproduced from reference [21].

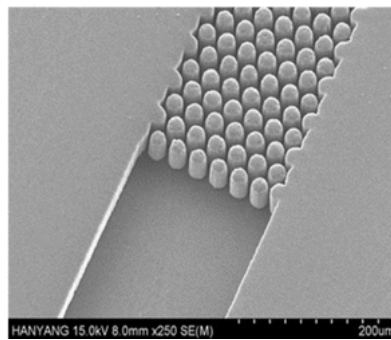


Figure 1.4: Micrograph of micro-pillars in a microfluidic channel. Reproduced from reference [24].

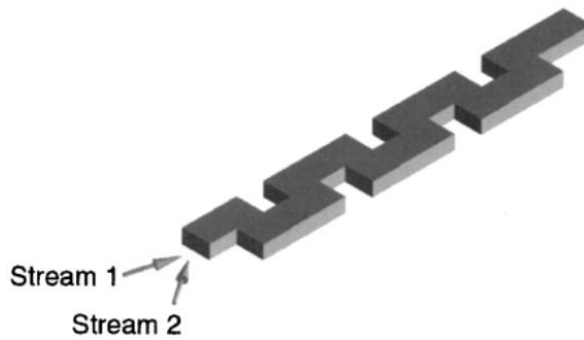


Figure 1.5: 3D drawing of a square wave mixer in a microfluidic channel. Reproduced from reference [23].

This square wave mixer concept can be extended by moving into a three dimensional pattern, as in a serpentine mixer [25] which was shown to be very effective across a range of Re . The three dimensional serpentine reactor was much more effective than its two dimensional equivalent at all conditions. Z-axis construction of Polydimethylsiloxane (PDMS) devices is possible by layering of PDMS sheets [26]. The 3D drawing in figure 1.6 shows how this mixer must be constructed in two layers. This adds a great deal of complexity and requires careful design of multiple masters on which to cast the PDMS. This is potentially unnecessary and reduces the robustness of the final design greatly.

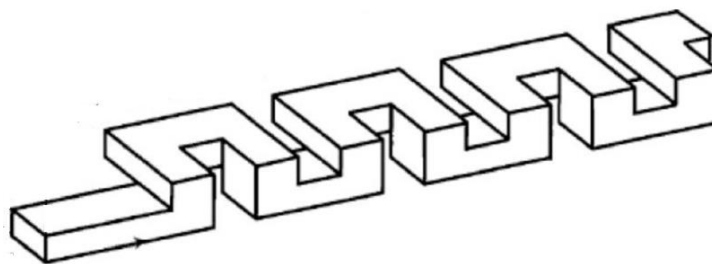


Figure 1.6: 3D drawing of the 3D serpentine mixer in a microfluidic channel. Reproduced from reference [27].

Flow focusing is an alternative strategy for the rapid mixing of liquid streams, be it by constricting flow in a channel to reduce diffusion distance or by using hydrodynamics to constrain a fluid flow between two laminae of a carrier liquid as shown in figure

1.7, [28, 29] again reducing the diffusion path length for homogenisation of the liquid stream. This can be extremely rapid with reports of mixing achieved in 8 μs and using low sample volumes [28]. This efficient mixing comes at the cost of increased equipment for the carrier fluid pumps. For in-line analysis, this method of mixing may be of particular interest because it allows the sample to be focused into a small area. For spectroscopic analysis, the light can be focused to interrogate a large fraction of the sample, increasing the efficiency of the detection.

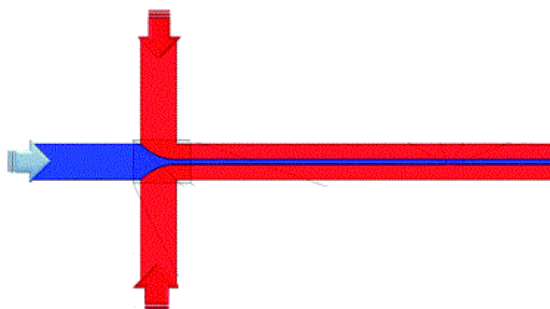


Figure 1.7: Drawing showing the general strategy of flow focusing, where the blue stream is the one with concentration gradient across its width. The red fluid is the immiscible carrier liquid. Reproduced from reference [30].

The final strategy for micromixing that is discussed here is the creation of chaotic flow patterns within microfluidics channels. These allow the fluid to fold together, increasing the surface area for diffusion and decreasing the average distance for diffusion to homogenise the stream.

The simplest method of generating this type of mixing is angled grooves along one wall of the device. This directs fluid along the grooves and creates rotational flow in the device. This lateral flow disrupts the laminae across the device and accelerates mixing. A more complex in-line passive mixer, designed to improve upon a simple array of angled grooves, is the staggered herringbone mixer (SHM)[31-33]. It consists of recessed offset herringbone designs patterned into the material of the microfluidic channel. The SHM differs from angled grooves because it establishes two separate rotational flow patterns in the channel. This mixes each side of the sample separately

but because the herringbone pattern is offset from the centre of the channel and the offset is changed every ten cycles, the full channel is mixed very rapidly.

A section of the staggered herring bone mixer is shown in figure 1.8. The dark blue block is the glass with the transparent red representing the PDMS of the device. The light blue colour represents the liquid flowing through the device. Figure 1.9 shows a full cycle of the SHM in a top down 2D representation. X' and Y' are the axes offset by 45° to represent the angle made with the channel by the SHM. The resistance down the grooves of the SHM will be significantly lower than continuing directly down the x axis. Figure 1.10 shows a simulation of how the fluids are folded together in the SHM.

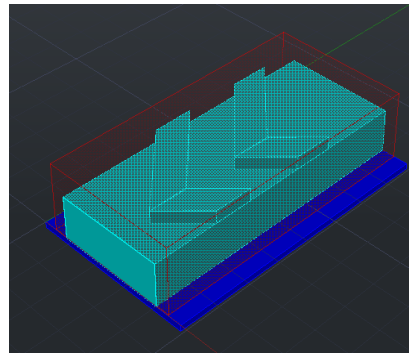


Figure 1.8: Diagram of a channel with a staggered herringbone mixer. The light blue element is the fluid flowing through the channel.

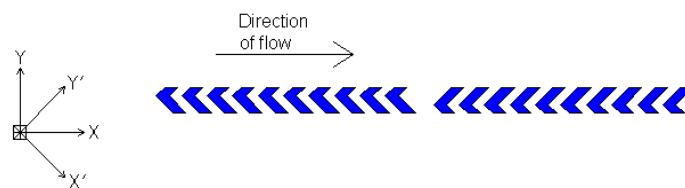


Figure 1.9: Top-down 2D representation of the SHM. Note the second axes x' and y' shown to indicate the angle of the SHM with the direction of flow.

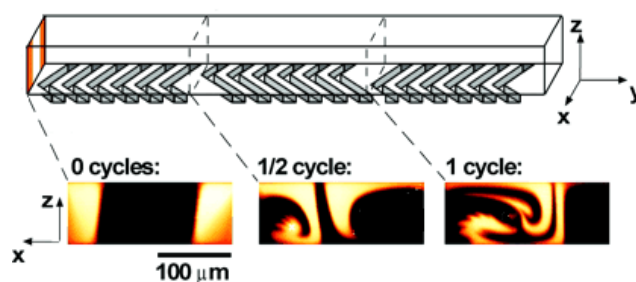


Figure 1.10: Simulation showing how laminae mix at successive stages in the SHM. The cross-sections shown show how fluids are folded together, reducing the characteristic mixing length. Reproduced from reference [31].

Of the possible mixing strategies, the most applicable are those which result in very rapid mixing (particularly at low Reynolds numbers) and which do not add complexity to using the device. The square wave and zigzag mixers demonstrated little effect on mixing at low Re so should be discounted. Both the 3D serpentine channel and flow focusing are very effective but required devices which are more complex to make and use. The chaotic micromixers are therefore the most suitable for this kind of device. Of the chaotic mixers the SHM is proven to be the most effective and has been studied widely and is now routinely used. The characteristic mixing time of the SHM is not discussed in the original work but mixing is completed within around 0.5 cm [31]. For a representative velocity of 5 mm/s, this gives a mixing time in the order of seconds. As discussed below, this is a good match for the rate of the chemical reactions performed on-chip. This makes the SHM ideal for use in the device developed here.

1.2.1.2 Transferring Reactions from Batch to Microreactors

The second major challenge in employing microfluidic technology for the type of LOC under investigation here, is designing systems to effectively perform the chemistry required on-chip. Previous reports in literature have relied upon binary mixes of reagents [20] or on single solution reactions with thermal activation of the reaction

[34]. Both of these strategies are suitable for specific types of chemistry and some reactions may be adapted to fit this limited scope.

However, it is often the case that efficient bench-top chemistry has been developed which relies on mixing different volumes of reagents together. This work focuses on development of a LOC to facilitate the ready application of existing chemistry to microfluidic platforms, in order to benefit from the advantages of these microsystems. To this end, the re-optimisation of bench-top chemistry is not a reasonable step to take for transfer of every process to a microfluidic platform. It would be far better if the sequential steps used in bench-top chemistry could be transferred more directly into microfluidic devices.

Flow through LOC devices can be driven in two different ways; either by applying positive pressure at the inlet, to push reagents through the device or by negative pressure to draw reagents through the device. Positive pressure devices have an inherent solution to transferring stoichiometric mixes into microfluidics, as the flow rate at each inlet is independently controlled by separate pumps. This simple solution to the problem of moving unequal mixing steps into LOC devices is at the cost of having multiple pumps, which incurs significant expense. Negative pressure would be a more desirable regime to use, as it requires less infrastructure to operate. To achieve unequal flows through the device with this method of driving the fluid flow, some method for manipulating the parameters of the device and calculating the results was required. This is discussed below.

1.2.1.3 Electrical Circuit Analogy for Device Design

In the extremely laminar system of microfluidic devices, the Hagen-Poiseuille equation can be used to give an analytical description of fluid flow, which can be used to calculate flow rates through a device.

$$Q = \frac{\Delta P \pi r^4}{8 \mu L}$$

Where Q is the volumetric flow rate, ΔP is the pressure drop, r is the channel radius, μ is the viscosity of the liquid and L is the channel length.

For a constant pressure drop, the equation shows that the flow rate is proportional to the radius of a circular duct to the 4th power and inversely proportional to the length of the channel. In microfluidic systems these are both parameters of the device which can be controlled. For different relative flow rates through the device, changing the radius becomes more difficult, due to the fabrication methods used. This leaves channel length as the most easily controlled variable to manipulate flow rate through a negative pressure device.

For a mixture of two reagents this relationship is easily employed: the flow rates will be inversely proportional to the length of the channels, so a flow rate can be lowered by lengthening a channel. For more complex LOC applications this becomes more difficult to model, particularly where stream splitting junctions are involved. This makes it difficult to employ the Hagen-Poiseuille directly, for anything but the most straightforward devices.


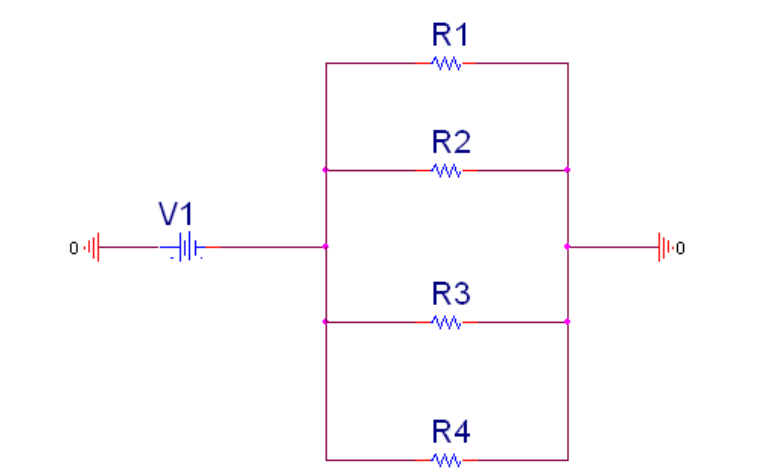
Since the Hagen-Poiseuille equation is difficult to apply directly to more complex LOC applications, some method of modelling flow rates in a device would be very useful. Multiphysics engines using finite element analysis would be the most comprehensive way to do this, as they can represent laminar flow accurately, but this type of simulation is computationally expensive. A computationally inexpensive and readily alternative solution exists, in the form of the electrical circuit analogy. Where fluid flow in the system is laminar and incompressible, the Hagen-Poiseuille equation can be compared to Ohm's law, which relates electrical current, voltage and resistance. The equations are compared below in table 1.1 with the Hagen-Poiseuille equation given for flow in a circular pipe [12].

Table 1.1: Electrical circuit/ microfluidic analogy equations.

	Ohm's law	Hagen-Poiseuille
Resistance	$R_e = \rho_r \frac{L}{A} \text{ (Pouillet's law)}$ <p>[35] R_e is electrical resistance; ρ_r is the peak resistivity; L is the length of the conductive material; A is the cross sectional area</p>	$R_h = \frac{8\mu L}{\pi r^4}$ <p>R_h is hydraulic resistance; μ is the dynamic viscosity; L is the length of the flow channel; r is the radius of the circular pipe</p>
Flow rate	$I = \frac{V}{R_e}$ <p>I is the electrical current; V is the voltage</p>	$Q = \frac{\Delta P}{R_h}$ <p>Q is the volumetric flow rate; ΔP is the pressure differential</p>

If voltage is viewed as the potential difference between two points in an electrical circuit, it can be seen that the two systems are equivalent. The comparison also allows us to calculate total stream resistance as would be done for an electrical circuit using series/parallel resistors as in table 1.2.

Table 1.2: Combining series/ parallel resistance equations.

Series resistance		R_{total} $= R_1$ $+ R_2$ $+ R_3$ $+ \dots$ $+ R_n$
Parallel resistance		$\frac{1}{R_{total}}$ $= \frac{1}{R_1}$ $+ \frac{1}{R_2}$ $+ \frac{1}{R_3}$ $+ \dots$ $+ \frac{1}{R_n}$

This is useful because circuit simulation software is readily available and can be run quickly on a desktop computer. By making it possible to rapidly model the flow rates through a complex LOC, with multiple inlets and stream splits, the circuit simulation software allows the use of an iterative approach to designing devices. This approach is very rapid and inexpensive. The resulting designs allow us to readily transfer relative flow rates into a microfluidic device driven by negative pressure. In this way the electrical circuit analogy and associated simulation tools allow LOCs to be designed which maintain mixing ratios from bench-top chemistry and operate with lower costs, by requiring only one pump.

The concept of a device using channel length to control flow rates has previously only been reported in relation to a device used to generate a concentration gradient of

some components or mixes of multiple components [36-40]. It is useful in these terms as a means to generate concentration gradients for the study of biological and chemical processes. The work shown below is the first to use this concept to facilitate the rapid, facile transfer of chemistry from bench-top to LOC, by employing circuit simulations to control mixing ratios for reagents on-chip.

1.2.2 Lectins

In order to develop the LOC for protein detection, an initial target was required. Initially the target was narrowed to a class of proteins called lectins, which are proteins which bind to carbohydrates. As outlined below, they are a highly relevant class of proteins for healthcare analysis and their interaction with carbohydrates has previously been used as a method for detection. They are found widely in nature and are involved in multiple interactions where they serve a variety of purposes [41-43]. Lectins comprise multiple protein sub units which each bind to a single carbohydrate residue. In nature they are key, as carbohydrates are found widely, both free and as residues on proteins and cells. In biological systems the interaction of lectins with these carbohydrates is key to many processes. These include cholera infection, initially mediated by interaction between a lectin toxin and a carbohydrate residue (GM1) on the gut wall [44]; ricin agglutination, the ability of a lectin component in ricin to attach to blood cells and cause blood clots [45] and influenza infection, which is initiated on a cellular level by adhesion between a lectin on the virus and sialic acid residues on cells [46]. This extensive array of interactions extends far beyond the initial disease stages and toxic effects outlined above, but it is for their role in these processes that lectins are of great interest in healthcare diagnostics. As lectin/carbohydrate interactions are often at the start of a disease cycle, they are useful for detecting early stage disease or potential infections, rather than diagnostic targets associated with later stage infection and illness.

As well as being important in native processes as outlined above, lectins have been widely employed as a tool for investigation of biological processes. As outlined above,

carbohydrates are widely found in biological systems so using lectins to target or label these is a common strategy for advancing knowledge of these systems. They have been used in the detection of serum glucose for diabetes monitoring [47] and as cellular markers for multiple types of cancer [48].

Many of the lectins identified above as potential diagnostic targets have acute biological activity and the potential to cause harm. For this reason, it is common to use plant lectins as a model for developing detection systems, before advancing into the detection of more relevant targets. Of these plant lectins, concanavalin A (ConA) is often used as a well characterised lectin to further the understanding of carbohydrate/ lectin interactions [49, 50] and the properties of lectins in general [51]. ConA has high specificity for glucose so is often used as a tool in the study and monitoring of blood sugar in diabetics [47]. Whilst ConA itself has relatively low relevance as a diagnostic target, both its wide use as a probe in the study of diabetes and its position as a standard model for lectin studies, make it a useful target for the development of a lectin detection system.

ConA will bind to mannose and glucose but will not bind to the very similar galactose. Glucose is a C2 epimer of mannose and a C4 epimer of galactose, as shown in figure 1.11. The selective binding between these molecules exhibits how specific the binding can be, distinguishing between different stereoisomers of the same molecule. Lectins have a complex structure with multiple binding loops; the amino acids expressed in these residues define the specificity of the binding. A monomer of ConA is composed of 237 amino acid residues and has a single carbohydrate binding site. ConA adopts a dimeric structure below pH 6 and a tetrameric structure at around pH 7 [52]. At a physiological pH, ConA will have an agglutinating effect because it can form these tetramers. ConA is also a metalloprotein as it requires Ca^{2+} and some transition metal ion (usually Mn^{2+}) to adopt an appropriate structure for binding. The tetrameric crystal structure of ConA is shown in figure 1.12, with a calcium ion in the binding pocket [53]. The binding sites are at the corners of the tetramer. The binding sites are within the loops of the protein (loops shown in red below), with the α -helix,

β -sheets and other structures shown in grey (these are not directly involved in the binding).

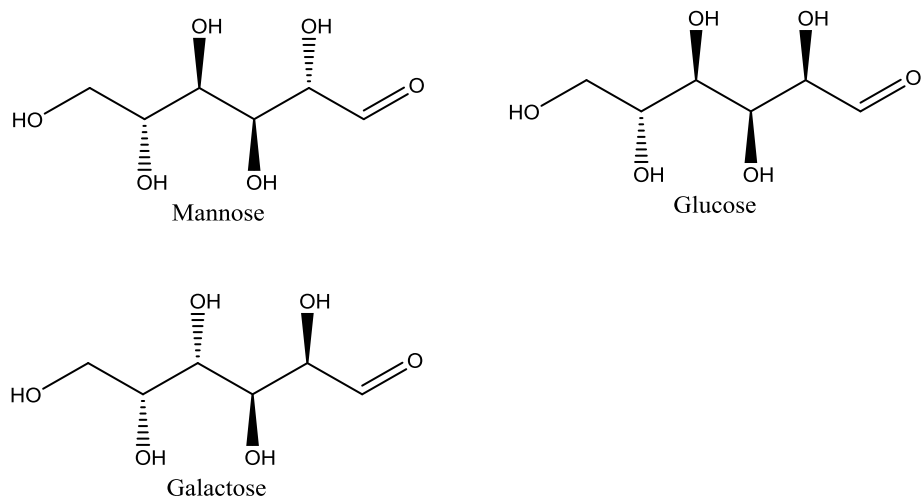


Figure 1.11: The open-chain structure of mannose, glucose and galactose.

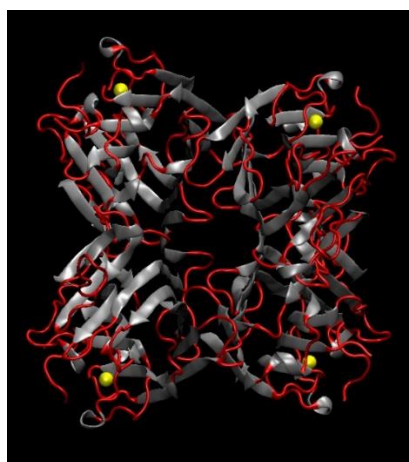


Figure 1.12: The crystal structure of the lectin ConA with the loops in the structure shown in red and the other structures shown in grey as arrows. Metal ions (Ca^{2+}) are shown in yellow in the binding pocket.

1.2.2.1 Carbohydrate Chemistry

To employ ConA as a model detection target for lectins in general, some understanding of carbohydrate chemistry and how this leads to a specific interaction is required. As described briefly above, lectins bind to specific carbohydrates, depending on the lectin in question. This selective binding arises because of the chemistry of the carbohydrate to which the lectin binds. The chemistry of carbohydrates is complex and wide ranging and several different forms are accessible to even single sugar molecules (monosaccharides), ConA effectively binds to these simple monosaccharides, however other lectins show specificity for more complex carbohydrate patterns or residues, such as the GM1 residue to which cholera toxin binds [44] or the GD1b and GT1b gangliosides to which tetanus toxin binds [54].

Structures of these monosaccharides include open-chain, five membered heterocycles (furanose) and six membered heterocycles (pyranose) structures; an example of each of these structures is given for glucose in figure 1.13. In addition, there are several chiral sites in glucose and these can give rise to several stereoisomers. L-glucose is not found in nature and only D-glucose is used as an energy source and is expressed as carbohydrate residues on cells. For this reason, only D-glucose is of interest as a molecule for binding to ConA. In solution this will adopt an equilibrium mixture of 38% α -pyranose, 62% β -pyranose, 0.5% α -furanose, 0.5% β -furanose and 0.002% straight chain [42]. Of these only the β -pyranose form will effectively bind to ConA [55]. All of these structures are shown in figure 1.14.

Other carbohydrates such as mannose will have higher specificity for the ConA and will displace glucose from the binding site when both are in solution. This is due to the addition of a favourable interaction with the changed orientation around the C2 position in mannose as compared to glucose. This means that it is not possible to differentiate between the interaction of ConA and mannose or glucose, without further experiments. Glucose, mannose, methylmannose and methylglucose are the most common sugars that bind to ConA [56]. As a consequence, the method developed in this chapter will not be highly specific for a glucose/ ConA interaction,

due to the multiple binding partners of ConA and of the simple monosaccharides. Hence, it's real-world utility will be limited.

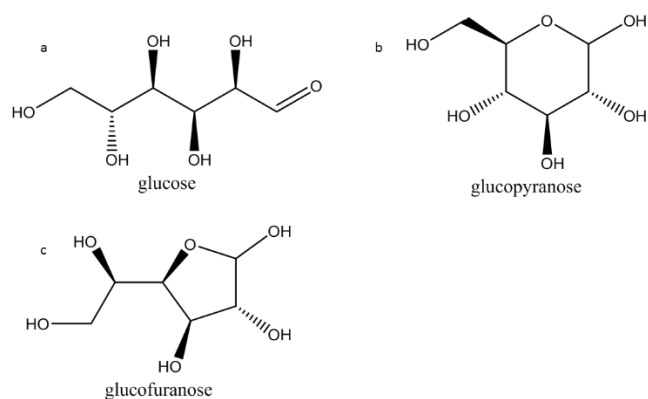


Figure 1.13: Structure of open-chain glucose (a), glucopyranose (b) and glucofuranose (c).

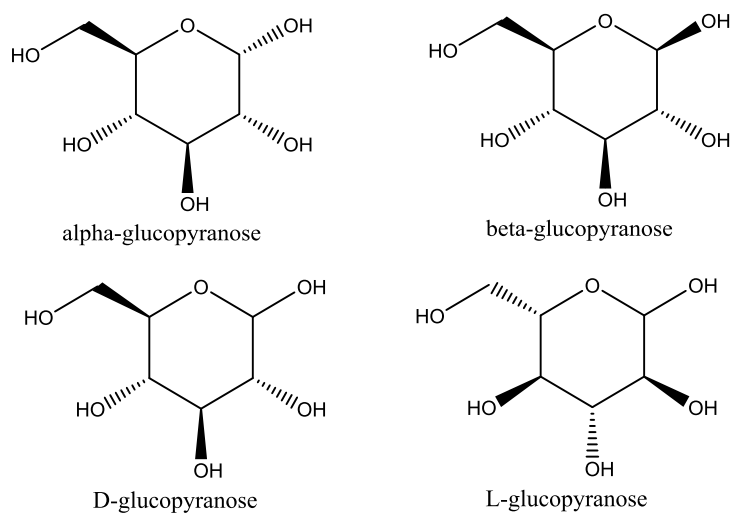


Figure 1.14: The isomers of glucopyranose accessible in solution.

For this work it is sufficient to say that lectins are a highly relevant class of proteins, that can interact very specifically with sugars. The detection of ConA will give a good representation of detection of many proteins in this class, with limitations on specificity due to the relatively simple monosaccharides to which it binds.

1.2.2.2 Lectins and Microfluidics

Complementary works that exist in the literature are relatively numerous, due to the extensive interest in microfluidics as an enabling technology. Key examples include a surface based microfluidic analysis using the lectin/ carbohydrate interaction to profile post-translational glycosylation in a protein sample [57] and a sandwich type assay for detecting glycosylated prostate specific antigen [58]. This is of interest as it is an attempt to detect the same interaction but with inverted roles; the lectin is the sensing probe and the carbohydrate the target. In using a surface assay, the need for mixing is somewhat reduced as the sensing probe is fixed. The glycosylated proteins for detection must also be tagged fluorescently, through an initial biotinylation, hence adding several benchtop chemistry steps to the on-chip detection. Lectins have also been detected in ELISA type formats in microfluidics [59] with antibodies as the sensing probe, again showing the prevalence of surface bound assays in the detection of proteins in microfluidics.

1.2.3 Plasmonic Nanoparticles

To highlight the ability to transfer existing chemistry into the LOC device, two existing analytical techniques which have previously been successfully employed for detection of ConA will be shown. This allows the development of two separate assay formats, namely surface enhanced Raman spectroscopy (SERS) [60] and a plasmonic nanoparticle colourimetric assay [61]. This is in keeping with the potential for a sensitive quantitative assay in the laboratory setting (SERS) and a robust rapid assay for point-of-use results (colourimetric assay). Since both of these rely on plasmonic nanoparticles to facilitate the assay, the key physical and chemical properties of these, and why they lend themselves towards use as a tool for analysis is outlined.

The key property of nanoparticles made of certain metals making them useful in analysis is the interaction of these particles with light. Due to their size, these nanoparticles exhibit optical properties not normally observed on the scale of bulk metal. Many of these are associated with the oscillation of delocalised electrons in

the nanoparticle under the influence of the magnetic field of a photon; this oscillation of the electrons is termed the surface plasmon and a diagrammatic representation of this is shown in figure 1.15. Due to the size of the nanoparticles and their geometry, the plasmon oscillation cannot propagate across the surface and so is termed a localised surface plasmon. Figure 1.16 shows a diagram representing a particle of 40nm (a typical size for colloidal nanoparticles) and a wave of 400nm wavelength (the shortest wavelength in the visible spectrum) together for scale. It can clearly be seen that the light wave will not be able to induce any plasmon propagation along the nanoparticle as the particle is smaller than the wavelength of the incident light. This simple assumption of the plasmon as a dipole will hold for particles where the size is much smaller than the wavelength of the incident photon [62].

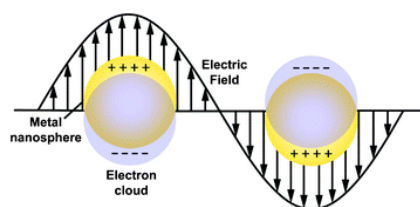


Figure 1.15: Diagram showing how the electric field of light can distort the electrons within a metal nanosphere. Reproduced from reference [63].

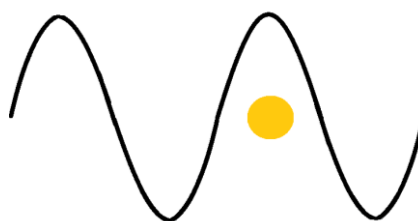


Figure 1.16: Diagram of 40nm particle and 400nm wave together for scale.

This electron oscillation has a resonance with the frequency of the photon; defined by the plasma frequency of the metal electrons, the geometry of the structure and the dielectric constant of the material around the nanoparticle [62]. At the localised surface plasmon resonance (LSPR) frequency, the absorption, scattering and other

optical properties of the particle are enhanced. This gives rise to a distinctive colour, as photons around the LSPR value are scattered and absorbed to a greater degree than photons not matching the LSPR value. The observed colour is very strong with molar extinction coefficients for the metal nanoparticles around $10^9 \text{ M}^{-1} \text{ cm}^{-1}$ compared with $10^4 - 10^5 \text{ M}^{-1} \text{ cm}^{-1}$ for strongly absorbing dyes [64]. The high extinction of the nanoparticles makes them ideal for colourimetric assays as the colour can be detected at much lower concentrations with nanoparticles than with a dye.

Where these plasmonic nanoparticles are within approximately one diameter of another, the effective geometry of the particles and therefore the behaviour of the plasmon changes. This can be detected through the plasmon overlap as the plasmon resonant frequency becomes that of the new particle ensemble, not that of individual nanoparticles [65, 66].

SERS also utilises the enhanced optical properties afforded by a LSPR, in this case to enhance a specific type of scattering event called Raman scattering [67]. A brief introduction to Raman scattering is given in the Raman Scattering Assay section below.

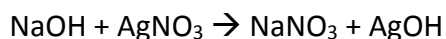
Plasmonic nanoparticles are typically made of silver or gold but other plasmonically active metals can be used. Gold and silver have different characteristics as substrates but both can easily be surface modified, using chemistry based on the bonding between the metal and sulfur [68], nitrogen [60] or oxygen atoms [69]. This allows for a variety of uses and also allows production of more stable colloids, as the surface modifications help prevent aggregation.

1.2.3.1 Silver Nanoparticle Colloid Synthesis

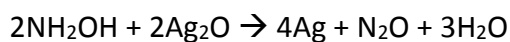
Silver colloid was employed in this chapter. The chemistry behind the formation of this colloid is outlined below. The colloid employed throughout was of the type prepared by Leopold and Lendl [70] using a basic solution of hydroxylamine as the reducing agent. The basic equation for the formation is detailed in literature as [71]:



With a possible side reaction between the silver nitrate used and sodium hydroxide giving silver oxide as a final product, due to the favourable reaction shown in the second step below [72].



This silver oxide then goes on to react with the hydroxylamine to be reduced by the following reaction



The overall reaction to form metallic silver is accelerated by the surface of the colloidal silver and, after the initial nucleation, should proceed quickly. In the case of both the reaction with the ionic silver liberated from silver nitrate and the reduction of silver oxide the product of the oxidation of the hydroxylamine is gaseous and will leave the reaction vessel. The counter ion to the soluble silver ion (nitrate when using silver nitrate) is left to cap the metallic silver formed along with other ions in solution including chloride [73].

1.2.4 Raman Scattering Assay for Lectin Detection

Using plasmonic metal nanoparticles, two types of assay were formed that relied upon the aggregation state of the nanoparticles. These were the colourimetric assay, detailed below and a SERS detection.

Raman scattering is an inelastic scattering of light by a molecule. Most scattered light is scattered elastically (Rayleigh scattering), i.e. the energy of the photon is conserved throughout the process and the incident and scattered photon have the same wavelength. A small number of photons are scattered inelastically, i.e. energy is

transferred to or from the molecule during the process. As the scattered photon interacts with the electrons of the molecule, they form a very short lived intermediate at a virtual energy level. If the molecule has vibrational states which result in a polarisability change, the scattered photon can transfer energy to the molecule to increase the vibrational energy to one of these levels. The scattered photon can then be detected and the change in energy measured (Raman shift). Raman shift values correspond to vibrational energies of specific functional groups so specific peaks can be assigned to parts of the molecule. Different peaks in the Raman spectrum will correspond to each of the Raman active vibrations in the molecule, building up a fingerprint of the molecule.

A primary difficulty in practical application of Raman to low concentration detection is the inherent weakness of the technique. Very few photons are Raman scattered so for analytical techniques, steps often have to be taken to maximise the response. This can be done instrumentally by choice of interrogating laser wavelength and power but this can pose problems through photo-degradation. The signal from Raman active molecules can be enhanced by the extremely high electromagnetic fields between two metal nanoparticles. This is termed surface enhanced Raman scattering and can result in large enhancements over Raman scattering [74].

By attaching a Raman active reporter, a great increase in signal can be observed on aggregation of the metal nanoparticles to generate hotspots. By controlling this aggregation in response to a target molecule, a SERS assay can be developed and is the basis of assays in literature [60, 75]. In the detection outlined by Craig *et al* [60], a linker molecule functionalised with a carbohydrate can be conjugated to silver nanoparticles through a terminal thiol. Alongside this functionalised linker molecule, a Raman active dye can be conjugated to the nanoparticle. When the carbohydrate/ConA interaction causes aggregation, areas of high SERS enhancement are formed and result in a large increase in the SERS signal observed. The difference between the low signal from unaggregated nanoparticles and the high signal from the aggregated system, is sufficient to discriminate between the two states and the change is in

proportion to the concentration of the ConA. Figure 1.17 shows how functionalised nanoparticles can aggregate in response to a molecule such as ConA

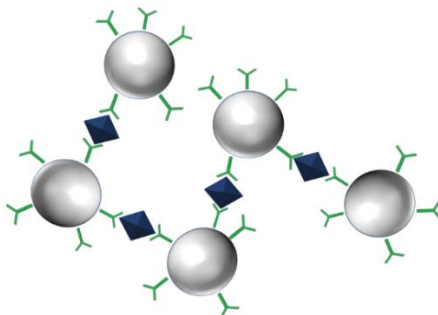


Figure 1.17: Picture showing how nanoparticles with carbohydrate linker molecules (green) can aggregate in response to target lectins (blue).

1.2.4.1 SERS and Microfluidics

Microfluidic systems have widely been employed with SERS as a platform for Raman detection. This is because the size of the microchannel allows for efficient interrogation with a laser beam. One early work identified four key advantages of using a microfluidic system over a cuvette based system [76]: reduction of variability in mixing time; elimination of variable scattering geometry; extreme reduction of local heating effects and reduction in the effect of photo-dissociation of the sample. For these reasons the stability of the SERS signal from the microfluidic device was significantly better than the other two systems.

More recent applications of this approach using off-chip prepared nanoparticles have covered allowing open channels of colloid to adsorb gas phase analytes from the atmosphere for detection [77]; droplet based microfluidics for the detection of the Raman dye crystal violet [76] and for the label free detection of bacteria in samples [78]. The variety of applications shows the perceived advantages of combining SERS and microfluidics. There are relatively few evident examples where the advantages of SERS detection have been coupled with the LOC concept. The few that do exist have not fully exploited efficient mixing [20], have not completely utilised the

capability of performing stepwise reactions [15] or have taken a different approach and targeted the efficient use of surface bound assays in the micro-channels [38].

1.2.5 Colourimetric Nanoparticle Assay for Lectin Detection

The LSPR which was detailed briefly above, causes an enhancement of the interactions between the electrons of the nanostructure and photons in resonance with the plasmon frequency. This enhancement applies to both absorbed photons and scattered photons; the combination of these two possible events is called extinction. Since the extinction is enhanced around the LSPR it results in a distinct colour of nanoparticles, depending on the suspending medium, size and shape. This colour is evident as a relatively narrow band on the extinction spectrum of the colloid, as shown for silver particles in different dielectric media in figure 1.18.

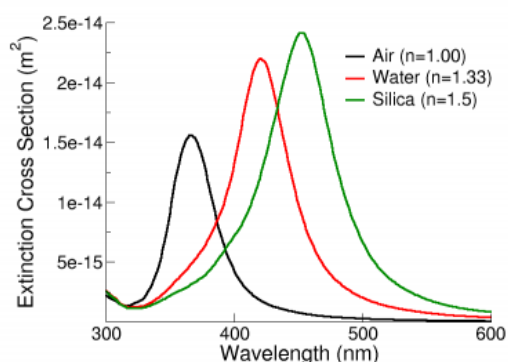


Figure 1.18: The extinction profile of a silver nanosphere in different dielectric media. The typical extinction profile is evident, along with the extinction maximum at around 410 nm in water. Reproduced from NanoComposix technical data.

Since this colour is dependent upon both the dielectric constant of the medium which suspends the nanoparticles and the size and geometry of the nanoparticles, there are two strategies which can be used to employ LSPR extinction in sensing. The first of these is to use the LSPR as an indicator for the changing dielectric medium [79], as it would be in a surface plasmon resonance sensor.

The second potential way is to use the extinction of the nanoparticles as an indicator for the state of aggregation. It has been shown before that plasmons from metal nanoparticles can interact over ranges of tens of nanometres [80] (much more than the optimal separation for SERS). When these plasmons interact, they give rise to a new plasmon relating to the effective geometry of the structure. This will be red-shifted compared to the extinction from single nanoparticles and the extinction peak will appear to broaden.

The emergence of this new plasmon mode will correlate to the extent of aggregation and can be used to quantify the concentration of the lectin causing the specific aggregation.

1.3 Aims

The aim of this research is to develop a device which is capable of a complete detection of a lectin in solution, for a sample-in, answer-out analysis. The overall aim will be to perform all the steps involved in a bench-top detection of a lectin in a single microfluidic chip. The motivation is to simplify the detection process at the point-of-use and obtain a result very rapidly. Reproducing the results of a batch analysis with the on-chip detection are key. Improvement of the process performed on-chip is not targeted here.

The device will use metal nanoparticle based detection and synthesise colloid to take advantage of the in-situ production of small volumes of fresh colloid. There are multiple microfluidic devices and synthesis methods for metal nanoparticles in the literature so existing synthesis will be employed. The device should generate nanoparticle colloid, of sufficient quality, on-chip.

Key to this research is the integration of multiple steps on chip and functionalisation of the nanoparticles is the second stage after synthesis. The device will be used to functionalise the freshly formed colloid to match functional nanoparticles used in batch detection. Detection will be off- or on-chip and using the same methods as a

bench-top assay. The device should perform the whole process in less than five minutes with less than millilitre volumes of reagents in process.

1.4 Results and Discussion

1.4.1 Microfluidic Design, Modelling and Testing

1.4.1.1 Design Basis of the Device and AutoCAD model

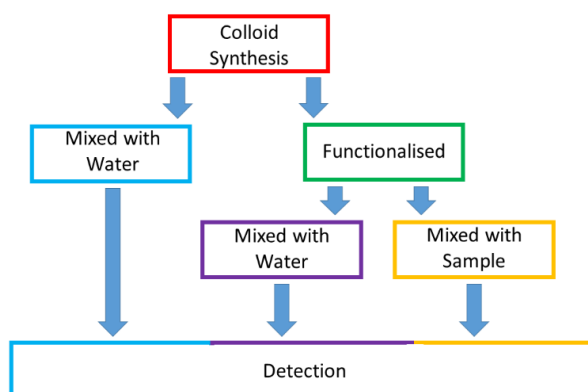


Figure 1.19: Block flow diagram showing the main sections of the device linking together. The light blue and purple streams are used as control channels and could be used for real time control for the main sample detection in the yellow section.

The initial design for the microfluidic device was to make silver nanoparticles then functionalise them with a carbohydrate linker and a Raman dye, before adding a lectin sample to be tested. Finally, a SERS spectrum was to be obtained. All steps were carried out under flow conditions and in a single, integrated, device. The colloid stream produced was to be split and mixed with water to obtain a reference spectrum and similarly the functionalised colloid would be split and mixed with water to obtain a control spectrum without any sample. The block flow diagram (figure 1.19) below shows the main features of the device.

The electrical circuit analogy detailed in the introduction was used, so that the flow rates through the device would be implicitly built in. The ratios in which the reagents were to be mixed were based upon those observed in batch experiments. To reduce the requirement for heating (which would add to the complexity of designing and using the device), a room temperature reduction was employed. The Leopold and

Lendl method of reducing silver nitrate with hydroxylamine hydrochloride under basic conditions at ambient temperature [6] was selected as a method proven to give stable, readily functionalised colloid [81]. A mixing ratio of 9 parts hydroxylamine hydrochloride (1.67×10^{-3} M) and sodium hydroxide (3.33×10^{-3} M) solution to 1 part silver nitrate (1×10^{-2} M) solution was reported in the original paper. The newly formed colloid was then to be functionalised by a polyethylene glycol (PEG) based carbohydrate linker. Functionalisation of silver surfaces with PEG has been shown before; the PEG allows rapid organisation of the molecules into an ordered monolayer [82-84]. The PEG molecule was also capable of being functionalised with a carbohydrate off-line before use. This functionalisation stream was to be mixed with the colloid at a ratio of 1 part linker to 10 parts colloid. The sample for analysis was then to be mixed with the functionalised colloid; the optimum for this ratio was unknown but a target of approximately 1 part sample to 1 part functional colloid stream was chosen. The synthesis of the carbohydrate-PEG linker was achieved by the widely used amide coupling of an aminated sugar and carboxylic acid terminated PEG (full details are given in the experimental section). The inlet streams and their desired ratios to one another are detailed below in table 1.3.

Table 1.3: Relative flow rates through the microfluidic system.

	Inlet flow	Relative flow rate
Colloid production	AgNO ₃	1
	NaOH/ hydroxylamine	9
Functionalization	PEG linker	1
Colloid dilution	Water	3.7
Functionalized colloid dilution	Water	3.7
Sample mixing	Sample	3.7

A first attempt to design the circuit in AutoCAD is shown below with colours to indicate the major component of each stream (figure 1.20 and table 1.4).

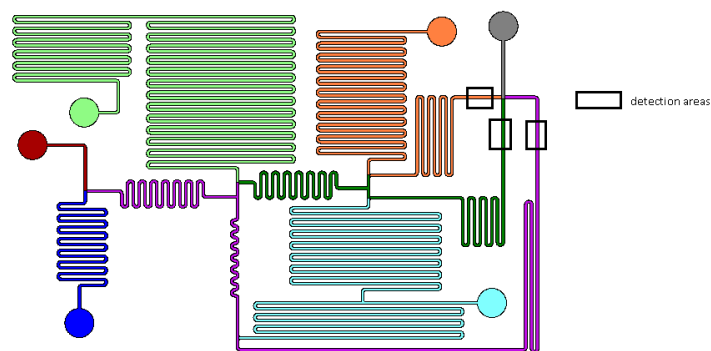










Figure 1.20: Colour coded CAD drawing of the microfluidic device. Colours correspond to those shown in table 1.4. Fluid flows from the coloured inlet towards the common outlet (grey).

Table 1.4: Major stream components in the microfluidic device.

Colour	Stream component
	AgNO ₃ solution
	Hydroxylamine hydrochloride/ NaOH solution
	Colloid
	PEG-carbohydrate solution
	Carbohydrate functionalized colloid
	Water
	Sample
	Waste

1.4.1.2 Modelling the Device using Electrical Circuit and COMSOL Simulation

The basic circuit simulation model is shown in figure 1.21; all inlets and stream junctions are in the same positions for comparison with figure 1.20. Ground symbols represent inlets and the current source (I1), represents the pump.

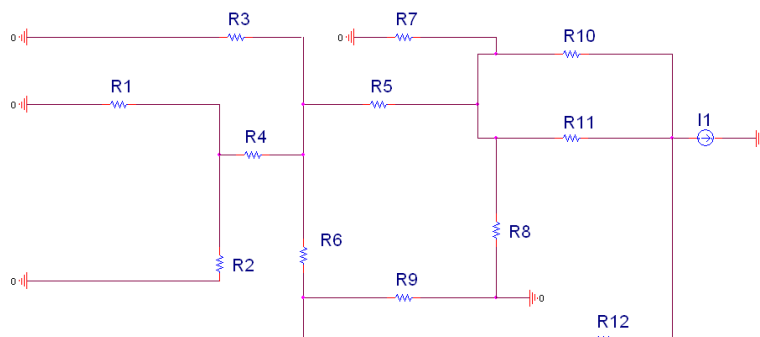


Figure 1.21: Circuit simulation representation of the analogous electrical circuit.

Resistors represent the equivalent channels and the current source simulates a pump. Channel layout and position of the sample inlets corresponds to figure 1.20.

Two main limitations must be considered when transferring the conceptual design into the circuit simulation and on to a practical design. These are the time required for each step and the limited surface area on the silicon wafers to be used for making the devices. Ideally, the channels could be any length but the mixing stages of R4, R5, R10, R11 and R12 required some minimum length of time for the reactions to complete. The synthesis of colloid (R4) in particular required to reach completion in the mixing stage for the device to operate effectively. In the usual batch synthesis, the silver nitrate is added drop-wise to a solution of hydroxylamine hydrochloride and sodium hydroxide. The first drop will have a very different stoichiometric amount of hydroxylamine to react with compared to the last given that the hydroxylamine is not in a large excess [71]. No report appears to detail how the colloid develops over time but Leopold and Lendl original method suggests a 20 minute period after addition was complete [70]. It was also observed that upon addition of silver nitrate, initially the development of colour appeared to be instantaneous. It was not therefore clear how long, after mixing it would take for silver nitrate to react with a stoichiometric amount of hydroxylamine. In light of the apparently instant

development of the colour, associated with the nanoparticle plasmon, this was assumed to be complete within seconds on-chip.

For functionalisation of the colloid, the thiol bond to the silver should form very quickly (in orders of milliseconds to minutes [85]). Initial coordination to the silver however will be disordered and it will take time for a cohesive monolayer to form, this may result in poor specificity of interaction if the carbohydrate molecule is not presented well on the surface for interaction with the lectin. This could only reasonably be assessed by testing the functionality and specificity of the formed carbohydrate conjugates in the lectin detection assay. Again, this step was assumed to complete in the order of seconds.

For practical production of the device, the available surface area on the silicon wafer to be patterned limited the length of very high resistance channels and those further downstream, as there was a finite footprint available for all channels. From previous works and practical advice given, the channels were made 200 μm wide by 70 μm tall. Total flow rate at the outlet was 200 $\mu\text{L}/\text{hr}$. This allowed for relatively straightforward fabrication and workable timescales for flow through typical devices.

With these considerations to the practicality of the final device in mind, the development of the circuit simulation model was broadly carried out as follows:

- An initial circuit simulation model was made, with assumed values used for resistors which could not have values rationally designed.
- The time through the two key mixing steps on the device was checked by calculation. If necessary, this was lengthened to give a reasonable value.
- These new values were used to inform the channel lengths in an AutoCAD drawing of the device. Where space was limited or designed resistances proved impractical, these were modified and fed back into the circuit simulation model.

- This iterative cycle was repeated until the AutoCAD model was practically feasible, matched the circuit simulation model and gave values close to those required from the conceptual design.

Rational design of several resistor values was possible from the ratios in table 1.3 and for the basis of the model, R1 (the hydroxylamine inlet) was set as 1 k Ω . The silver nitrate flow was 1/9th of the hydroxylamine inlet flow, so the channel resistance (R2) was 9 times higher at 9 k Ω . Other resistors that could have relative values assigned at this stage were the final mixing stages before detection (R10, R11 and R12) which were all set equal to give comparable mixing times and R7, R8 and R9, which were again all equal for the control channels to be comparable to the sample.

The next resistance assigned to continue to develop the model was R4, the mixing stage to synthesise the colloid. Through the iterative design process above, this was determined at 5.2 k Ω to give a mixing time of 14 seconds and a design which fitted with the AutoCAD model. This also allows sufficient time for good mixing with the SHM which had a characteristic mixing time around one second.

R3 was to be a very long channel for consistency with the conceptual design but this was limited due to the space on the AutoCAD model. R3 was set at 70 k Ω

R5 was also set equal to 5.2 k Ω , since this gave a reasonable mixing time of 20 seconds for functionalisation and fitted well onto the wafer.

R6 was equal 10.4 k Ω , to give 1/3rd of the colloid being bypassed to the control channel, without functionalisation.

R7, R8 and R9 were equal to the total upstream resistance at the junction, since the conceptual design called for a 1:1 mix with the functional colloid solution and sample. This was 26.9 k Ω .

R10, R11 and R12 were arbitrary since there are no further streams to be added and to facilitate the longest possible mixing time before detection, these were designed to use all the available space left in the AutoCAD model. This was 8.1 k Ω .

Flow rate was modelled by a D.C. supply of 200 A at the outlet, with all inlets as ground points. The final resistances in the circuit simulation model are shown in figure 1.22. Currents are shown in a separate table for clarity (table 1.5).

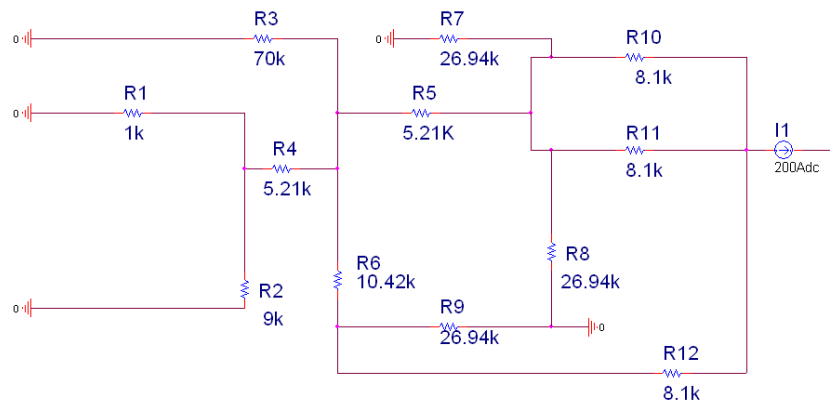


Figure 1.22: Circuit simulation with relative resistances in ohms shown beneath each resistor. Channel layout and position of the sample inlets corresponds to figure 1.20.

Table 1.5: Current flow through the circuit simulation model shown in figure 1.22.

Resistor number	Current (A)
R1	82.26
R2	9.14
R3	7.98
R4	91.40
R5	66.25
R6	33.13
R7	33.54
R8	33.54
R9	33.54
R10	66.67
R11	66.67
R12	66.67

On the AutoCAD model of the device, R1 was equivalent to 5384 μm . Other lengths were then scaled accordingly for the device and the physical lengths corresponding to the modelled resistances are shown in table 1.6. Additional pressure drop from the large number of turns was neglected, as previous work had shown that at very low Re in microfluidic devices even very sharp channel turns had no effect on the resistance of the channel [86].

Table 1.6: Actual channel lengths used in the microfluidic device.

Resistor number	Length (μm)
R1	5400
R2	48500
R3	376900
R4	28100
R5	28100
R6	56100
R7	145000
R8	145000
R9	145000
R10	43600
R11	43600
R12	43600

If a voltage source was included in place of a current source, it was possible to obtain a simulated value for the resistance of the whole device. The current through the voltage source represents the current flow through the whole device; using Ohm's law from above the total effective resistance of the circuit can be expressed as:

$$R_e = \frac{V}{I}$$

With a 1 V D.C. power supply was attached to the circuit, the resistance of the device could be obtained as the current over the whole device was equal to that over the power supply as shown in figure 1.23.

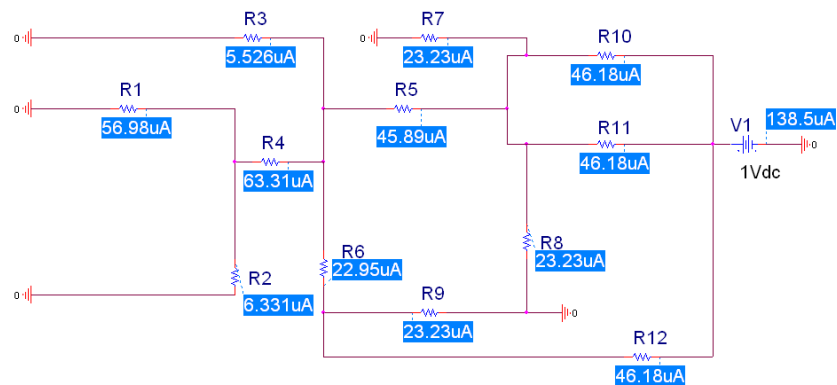


Figure 1.23: Circuit simulation of the device with a 1 V D.C. supply attached, showing current through each resistor with a blue background.

Total effective resistance of the circuit was 7.22 kΩ which was equal to an effective channel length of $7.22 \times R1$, or 38873 μm when expressed as a physical length.

The Hagen- Poiseuille equation was then applied to obtain a value for the pressure drop through the fluidic resistance. As the microfluidic device had a rectangular cross section, the fluidic resistance term is given by [87]:

$$R_h = \frac{12\mu L}{wh^3} \left[1 - \frac{h}{w} \left(\frac{192}{\pi^5} \sum_{n=1,3,5}^{\infty} \frac{1}{n^5} \tanh\left(\frac{n\pi w}{2h}\right) \right) \right]^{-1}$$

Symbol	Meaning	Value
μ	Dynamic viscosity of fluid (taken as water)	8.9×10^{-4} Pa.s
L	Length of flow channel	38873 μm
w	Width of flow channel	200 μm
h	Height of flow channel	70 μm

Clipping the summation of the hyperbolic tangent function to the third term, the following is obtained:

$$\begin{aligned} \sum_{n=1,3,5}^{\infty} \frac{1}{n^5} \tanh\left(\frac{n\pi w}{2h}\right) &\approx \frac{1}{1^5} \tanh\left(\frac{200\pi}{140}\right) + \frac{1}{3^5} \tanh\left(\frac{600\pi}{140}\right) + \frac{1}{5^5} \tanh\left(\frac{1000\pi}{140}\right) \\ &= 0.07817 + 0.00094958 + 0.0001192896 = 0.079 \text{ to 2 sf} \end{aligned}$$

Since the third term represents only 0.15 % of the final value, it was assumed that the shortened series gave a good estimate of the resistance.

$$\begin{aligned} R_h &= \frac{12\mu L}{wh^3} [1 - 0.35(0.627 \times 0.0792)]^{-1} \\ R_h &= \frac{12\mu L}{0.9826 \times wh^3} = \frac{4.1516364 \times 10^{-4}}{6.740636 \times 10^{-17}} = 6.159 \times 10^{12} \frac{\text{Pa.s}}{\text{m}^3} \end{aligned}$$

The pressure drop generated from inlet to outlet is then:

$$\begin{aligned} \Delta P &= Q \times R_h \\ &= (5.556 \times 10^{-11}) \times (6.159 \times 10^{12}) \end{aligned}$$

$$= 342 \text{ Pa}$$

This pressure differential was easily within the range of commercially available syringe pumps (typical value for a syringe pump is 138,000 Pa).

To check the validity of the assumption made in using the electrical/ microfluidic circuit analogy it was confirmed that the flow in the system remained laminar and incompressible. Addressing the compressibility of the liquid first, even over pressures of hundreds of bar, the change in volume of water is less than 1% [88]. For flow to be laminar, Re must be less than approximately 1700 [89]. Reynolds number for a circular pipe is related to the diameter of the pipe- to make the equation below applicable to this system, the diameter was replaced with the effective diameter for the rectangular flow channels in the microfluidic device [89].

$$Re = \frac{\rho v d_e}{\mu}$$

$$d_e = \frac{4A}{P}$$

Symbol	Meaning	Value
ρ	Fluid density (taken as water)	998 kg.m ⁻³
v	Fluid velocity (peak velocity in device)	3.97 × 10 ⁻³ m/s
d_e	Effective diameter (As defined above)	1.03 × 10 ⁻⁴ m
μ	Dynamic viscosity (taken as water)	8.9 × 10 ⁻⁴ Pa.s
A	Cross sectional area of flow channel	1.4 × 10 ⁻⁸ m ²
P	Wetted perimeter	5.4 × 10 ⁻⁴ m

$$Re = \frac{998 \times (3.97 \times 10^{-3}) \times (1.03 \times 10^{-4})}{(8.9 \times 10^{-4})}$$

$$= 0.458$$

This very low Re indicated highly laminar flow and that the device will closely match the circuit simulation model in operation.

With the validity of the design principles tested and the completed circuit simulation and AutoCAD models, the implicit flow control aspect of the device had been

successfully designed. The challenge of overcoming the poor mixing remained to be addressed. With the highly laminar flow in the device, mixing without the SHM would be too slow for practical use of the device.

The SHM design was imprinted to a depth of 20 μm , slightly deeper than in literature [31], and was assumed not to affect the resistance of the mixing channels. This assumption may not be valid since the mixing channels are a significant fraction of the channel height and therefore represent a significant change in the effective diameter in the fluidic resistance of the channel. Effects from this are minimised, since the three mixing stages just prior to SERS detection shown by the red boxes in figure 1.24 are all equal and so should have no net change on the flow rate of one stream over another. The mixing of functionalising agent and colloid and the mixing stage to form colloid (orange boxes in figure 1.24) may change the flow ratios between streams slightly, if the SHM has an impact on the resistance. The SHM used consisted of 10 patterned herringbones in each half cycle; equal to the design shown in figure 1.9. The SHM was patterned for the full length of the mixing zones indicated in figure 1.24. The necessity of the SHM is supported by appendix A, which shows how slow nanoparticle mixing can be by diffusion.

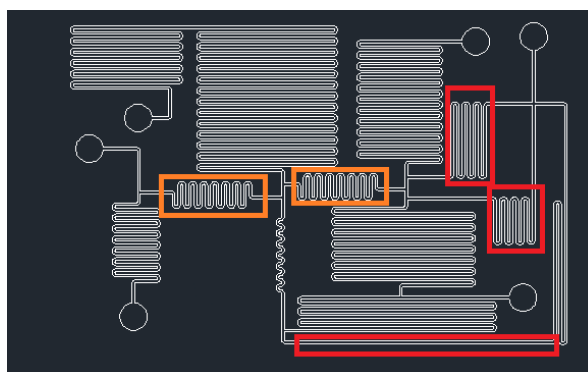


Figure 1.24: CAD drawing of the microfluidic device with mixing zones highlighted. The orange blocks are equivalent sections for making colloid then functionalising. The red blocks are equivalent mixing zones before detection.

To determine what effect the SHM would have on the fluid flow in the system, the pressure drop and flow pattern through the herring bone mixer was modelled and

compared to a standard channel in Comsol 4.0 multiphysics engine. The herringbone mixer and rectangular channel were modelled in the inbuilt CAD system, as a single element of water at 25 °C. Meshing was left as standard free tetrahedron with a maximum element size of 25 μm and a minimum of 4.5 μm . The laminar flow physics model was used, with no slip conditions at the walls under a static simulation. Inlet conditions were defined as a laminar average flow rate of 0.004 m/s (200 $\mu\text{L/hr}$ through a duct 70 μm by 200 μm) and outlet was defined as at zero pressure. The main channel was given a length of 250 μm . The simulation output gave the velocity component in the three dimensions, Reynolds number, pressure and vorticity. Key results for the x- flow component (across the width of the channel) and the pressure drop across the channel are shown in figures 1.25-1.27, with the full simulation results shown in appendix B.

Addressing the x- flow within the channel, this was a good indication of the effectiveness of the SHM geometry used in this device. Higher fluid velocities across the width of the device indicate better potential mixing across the laminar boundaries in the device.

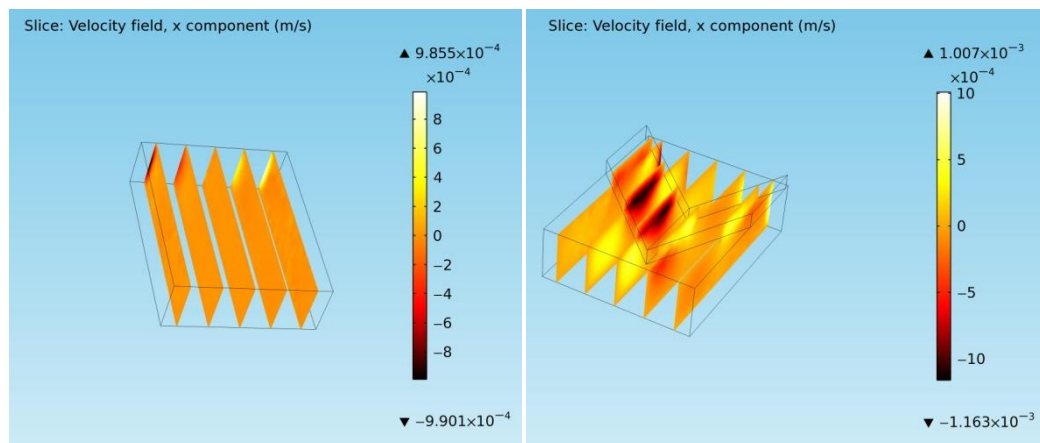


Figure 1.25: Comsol model of the x-component of fluid velocity in a normal rectangular channel (left) and the SHM (right). Fluid moving to the right is light and

has a positive value, fluid moving to the left is dark and has a negative value. Scale bars on the right show maximum and minimum values.

The SHM model in figure 1.25 showed much more variation in the flow velocity across the width of the channel than the rectangular channel. This indicated that the mixer would operate effectively, as per previous reports. Flow was diverted along the SHM towards walls of the channel, creating the helical flow. Flow in the rectangular channel showed almost no flow across the width of the channel, except for a very small area of high velocity at the end of the channel which appeared to be an artefact of the model.

The flow in the SHM can be further visualised using an isosurface plot of velocity, which is shown below in figure 1.26.

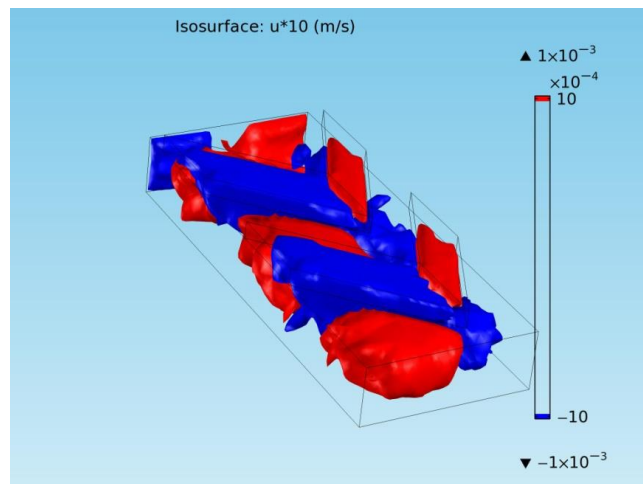


Figure 1.26: x-axis isosurface in a double SHM showing fluid moving to the right of the channel in red and fluid moving to the left in blue. The scale bar shows the boundary speed in m/s for each coloured volume.

The model in figure 1.26 was expanded to include a second SHM; to demonstrate how the fluid moves between the two patterned mixers. In this simulation output, any blue surface contains fluid elements that are moving to the left at 10^{-3} m/s or greater and red surfaces contain fluid moving to the right at the same velocity. The graphic clearly shows flow being diverted towards the walls of the channel in the

patterned SHM. This representation also shows the fluid rotating back to the center of the channel after the patterned mixer. Importantly, the fluid did not seem to cross the full channel in any simulation but remained confined in a helical flow on one side of the SHM. This was significant as it suggested that not alternating the offset of the SHM about the center of the channel would give poor mixing across the full width of the channel.

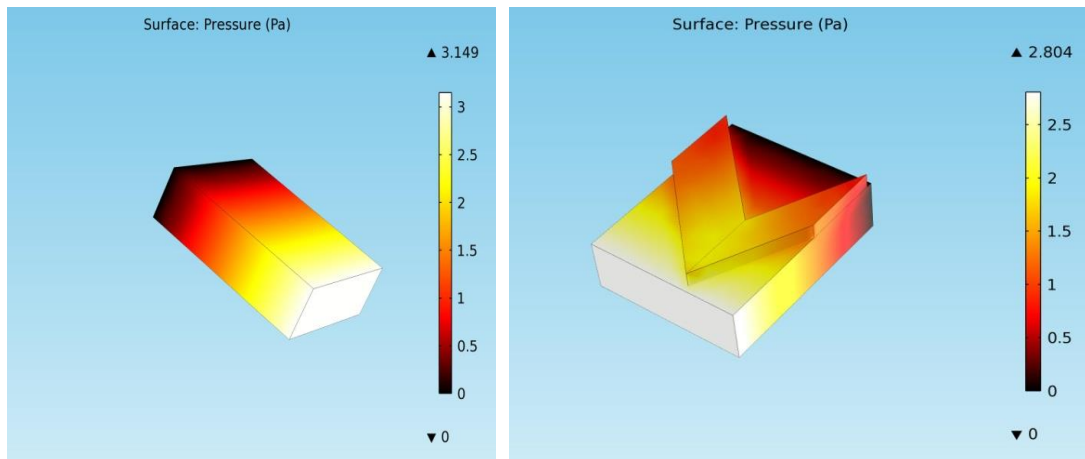


Figure 1.27: Surface pressure for a rectangular channel (left) and a SHM element (right). Maximum pressure is at the inlet and shown in white. Minimum pressure is shown at the outlet and shown in black. The scale bar shows the maximum and minimum pressures in the simulation.

The pressure drop along the length of the channel is given in figure 1.27 as a plot of the surface pressure; in this representation key information is given in the scale bar on the right of the figure. This shows the highest and lowest surface pressure in the simulation. Since the outlet pressure was constrained at 0 Pa at the outlet, the simulation must apply a maximum pressure to the inlet fluid for the values to be consistent. The maximum pressure in this simulation was therefore the pressure need to drive the fluid through the channel, or the pressure drop of the modelled channel. The pressure drop for the SHM was around 90% of that for the rectangular channel. This was consistent with the cross-sectional area of the channel being higher in the SHM. It was not clear without a much more advanced model, how this would scale with the large number of SHM elements present in the actual device. In any

case, the SHM appeared to have some effect on the pressure drop along a channel in the device. This is minimised in the device by making relative mixing zones equal but could still give rise to some deviation from flow rates predicted in the circuit simulation model. The changed pressure drop will have an associated change in resistance term, altering the flow through the mixing stages.

1.4.1.3 Experimentally testing Flow Control and Mixing in the Device

With the simulations of the device having indicated consistent flow rates through the device and the achievement of mixing, the device was then fabricated using the lithography techniques detailed in the experimental section. A picture of a completed device is shown in figure 1.28, which includes a one pound coin for scale.

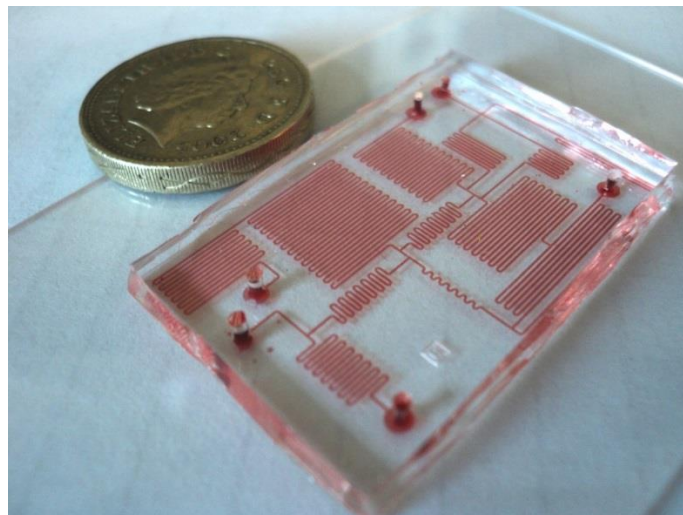


Figure 1.28: A completed device with red dye in the flow channels and a £1 coin for scale.

With the device fabricated, it was then necessary to practically test the device. Conformity of the actual device to the modelled flow rates was checked by introducing a red dye to each inlet successively. When this was run with water at all other inlets, the dilution of the dye could be measured from the absorption spectra. Performing this for every inlet meant that the fraction of the total flow rate through each inlet could be calculated and is shown in figure 1.29. Whilst there is some

difference and reasonable variation from device to device (indicated by the standard deviation error bars), overall the match between the circuit modelled current and the actual device flow rates was good. This practically indicated that the electrical circuit analogy was appropriate for designing lab-on-a-chip devices and that the electrical circuit simulator predicted correct values for the flow rates through the device. This supports previous calculations, which showed that the electrical circuit analogy was applicable. It also proved that the devices designed in this way can be fabricated to high enough precision so that the simulated values can be achieved. The predicted change in channel resistance for the mixing stages appeared to have little effect on the flow rates through the device.

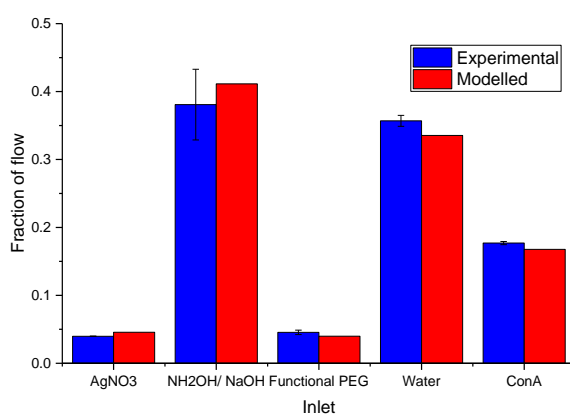


Figure 1.29: Comparison of the fraction of flow through each inlet of the complete device for experimental values (blue) and modelled values (red). Values shown for the experimental result are the average of five devices, with error bars of one standard deviation.

As the flow rate control through the device had been achieved and matched well to modelled values, it was necessary to show that the SHM achieved efficient mixing. Fluorescence microscopy was used to check the mixing in the channels was complete and how rapid mixing was. Fluorescein sodium salt was introduced at the hydroxylamine inlet and images taken at the points indicated below in figure 1.30.

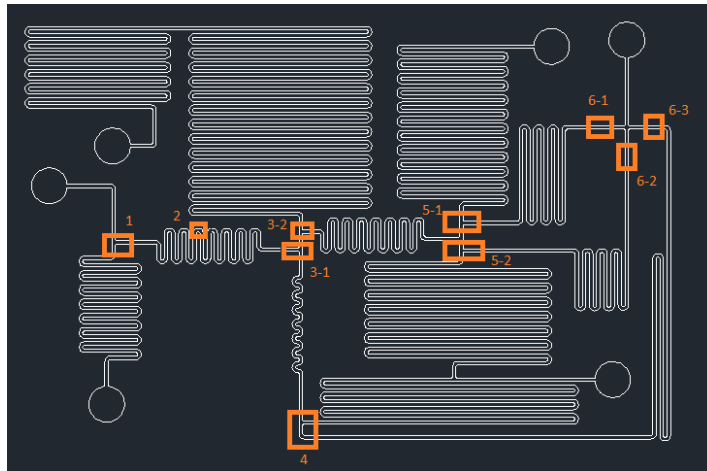


Figure 1.30: CAD drawing of the device with fluorescent image detection regions shown in orange. Numbered labels correspond to images in figures 31-36.

The sections shown in figure 1.31-1.36 encompassed the junctions of all streams and the end of each stream and the mixing after the colloid formation. Images were checked with the ImageJ program to establish the standard deviation of the pixel intensity across the channel. A single line of pixels 45 long to cover channel width and 1 pixel thick was positioned across the start or end of a channel as appropriate and a histogram plotted in ImageJ. The program also provided basic statistical information about the region. No processing was used on these images before analysis. For clarity the images shown below have been contrast enhanced to display the laminar boundaries more clearly.

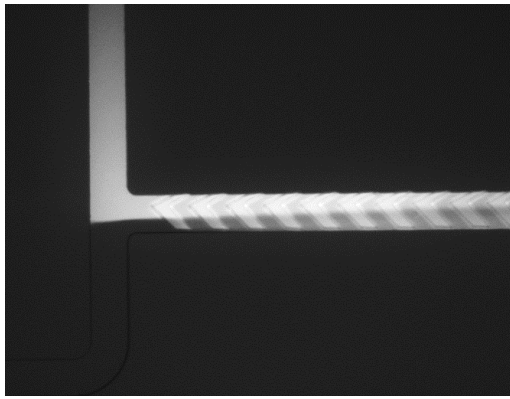


Figure 1.31: Fluorescence image of region 1 showing mixing around a junction of a fluorescent stream and water.

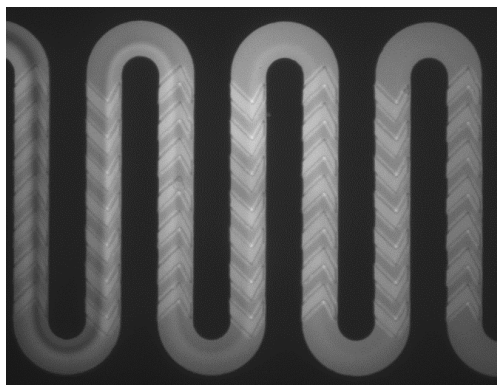


Figure 1.32: Fluorescence image of region 2 showing mixing progression along the SHM mixing region.

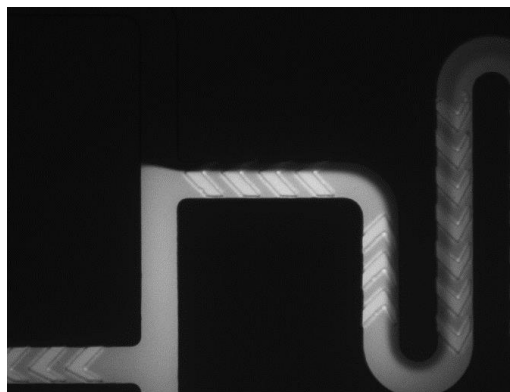


Figure 1.33: Fluorescence image of regions 3-1 showing the end of an SHM mixing zone and 3-2 showing the junction between a fluorescent stream and water.

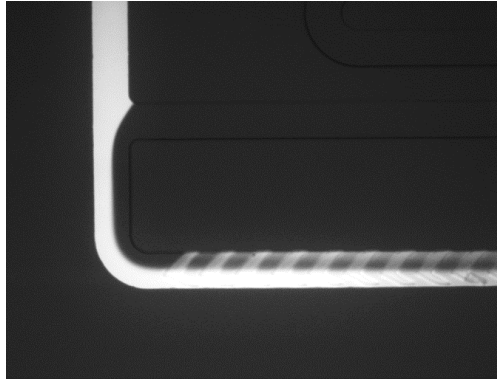


Figure 1.34: Fluorescence image of region 4 showing the junction between a fluorescent stream and water.

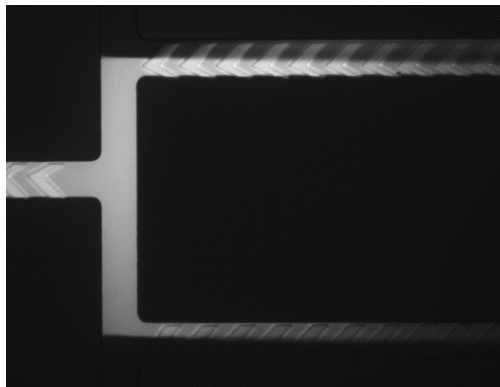


Figure 1.35: Fluorescence image of regions 5-1 and 5-2, each showing the junction between a fluorescent stream and water.

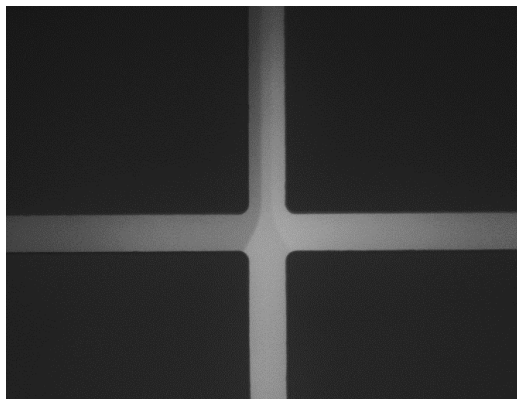


Figure 1.36: Fluorescence image of regions 6-1, 6-2 and 6-3 showing the end of each detection stream before transfer to to common outlet (top of imge).

Table 1.7: Fluorescence region, with mean pixel intensities, standard deviation, maximum and minimum values. All values correspond to the static images in figures 1.31-1.36.

Region	Mean pixel intensity	standard deviation	minimum value	maximum value
1	70	30 (41%)	31	100
2	105	6 (6%)	93	115
3-1	135	3 (2%)	128	140
3-2	120	40 (33%)	39	143
4	80	40 (50%)	32	121
5-1	80	40 (50%)	36	122
5-2	50	20 (40%)	32	121
6-1	57	2(4%)	47	60
6-2	69	2 (3%)	63	72
6-3	68	2(2%)	65	71

Qualitatively from the pictures and quantitatively from the fluorescence image analysis in table 1.7, it appeared that the mixing was very effective. The two streams being mixed were in clearly distinct laminae before the SHM, as confirmed by the standard deviation which was around half of the mean value in many cases. Using fluorescence images 1 and 2, the SHM is confirmed to have completed mixing to greater than 90% in two seconds. Comparable timescales to literature reports on the

SHM. After a limited number of SHM cycles (region 2) the standard deviation was already greatly reduced, both in terms of the absolute value and as a percentage of the mean value. After the complete mixing cycle in all cases the standard deviation was reduced to a low level and a value which was lower than the standard deviation in the inlet fluorescein stream in region 1 (standard deviation 4.0, 4% of mean).

In keeping with the Comsol model shown in figure 1.26, the SHM appeared to constrain the fluid within one side of the SHM. This is demonstrated by the clear boundaries in the fluorescence images (particularly evident in figure 1.32), and suggested that each side of the channel is homogenised separately from the other helical flow. This allowed development of a simple mathematical model, as to which orientation the SHM should be used in for most rapid mixing; this model is shown in appendix C.

1.4.2 Running the Device for Colloid Synthesis and PEG Conjugation

Since the device appeared to match the modelled parameters, it was then appropriate to address the chemistry it was designed to perform. The first key step in the device was the production of silver nanoparticles and this was tested first. Connecting the silver nitrate and hydroxylamine inlets to reagent reservoirs and leaving all other inlets blocked, the device was run to form silver nanoparticles. These were then taken off-line for analysis by extinction spectroscopy, dynamic light scattering sizing and zeta potential measurement.

The extinction spectra (figure 1.37) showed the typical plasmon peak of colloidal silver at approximately 400 nm. Compared to batch prepared silver nanoparticles, the extinction of the on-chip particles was very similar. There were some slight differences but the magnitude of the difference in the particles was small. The plasmon extinction of the on-chip particles was slightly narrower, suggesting lower sizing dispersity than in batch synthesis. The peak extinction occurred at a longer wavelength, indicating larger particle size. The presence of a plasmon extinction was

a good indication of colloidal silver being formed after mixing of reagents on-chip. The narrow extinction from the on-chip preparation was a good indication of high quality colloid being generated and which would be suitable for both analysis by SERS and aggregation colourimetric assays.

The bar charts in figures 1.38 and 1.39 show the average results for extinction maximum and the full width at half maximum height (fwhm) respectively. The average peak extinction of the on-chip prepared colloid was very slightly larger. However, results were well within one standard deviation of each other, suggesting a that the statistical difference may be weak. The standard deviation was approximately the same for both preparation methods, indicating that the variation from device to device was similar to batch to batch variation. The average fwhm was lower for the on-chip preparation than the batch prepared nanoparticles, indicating that the on-chip preparation gives a more monodisperse nanoparticle colloid. The standard deviation was higher showing that the device to device variation is relatively high, in terms of the consistency of colloid formed over the full run-time of the experiment.

The extinction of the nanoparticles indicated that the size of nanoparticles from batch and microfluidic synthesis was very similar. Colloid made in microfluidic synthesis had a lower fwhm on average but showed less consistency in the fwhm measured, possibly caused by unstable flow at start-up generating different distributions. No investigation was made here into the stability of the batch prepared colloid but this is relevant information for comparison with the on-chip preparation. The large batches prepared off-chip are used for a large number of experiments, so variation

in the properties of the colloid over time would be a useful comparison with the device to device variation observed here.

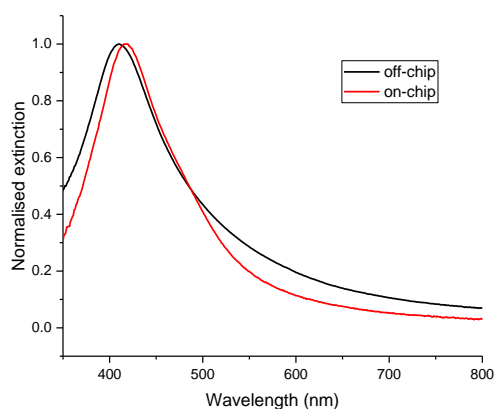


Figure 1.37: Extinction spectra of hydroxylamine reduced silver nanoparticles made on-chip (red) and off-chip (black). Spectra are results from representative single experiments.

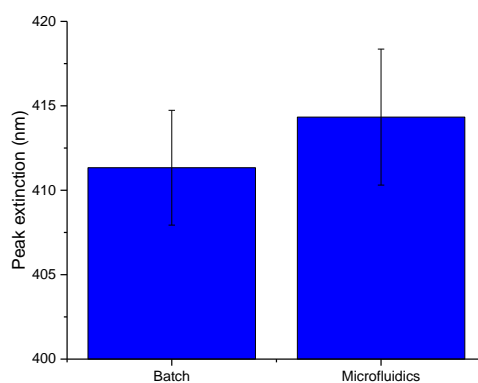


Figure 1.38: Peak extinction of hydroxylamine reduced silver nanoparticles formed in batch synthesis (off-chip) and on-chip. Results are the average of results from three separate batches and three separate devices. Error bars are one standard deviation.

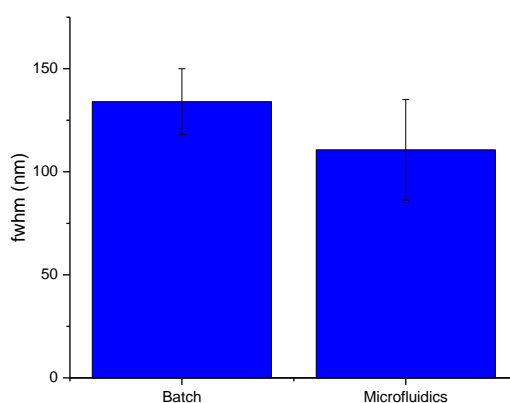


Figure 1.39: Fwhm of hydroxylamine reduced silver nanoparticles formed in batch synthesis (off-chip) and on-chip. Results are the average of results from three separate batches and three separate devices. Error bars are one standard deviation.

To support the information obtained through extinction spectroscopy experiments, DLS sizing experiments were also carried out. This gave an explicit measure of the hydrodynamic radius and the dispersity of a colloid batch could also be determined. DLS results corresponding to the extinction spectra are shown in figure 1.40. The intensity distribution showed a slightly higher proportion of smaller particles in the on-chip prepared particles and that on-chip, the minor particle size was smaller (9 nm on-chip and 12 nm off-chip). Both show a larger peak at 68 nm but this constituted up a higher proportion of the particles in the off-chip prepared particles. Due to the multimodal distribution observed in these samples, caution should be exercised in drawing extensive conclusions from the data. Since it is an intensity distribution, there will be a bias in the data towards larger particles being over-represented. The z-average size (the single figure size result from DLS) was 62.1 ± 9.5 nm for the batch preparation and 41.0 ± 4.4 nm for the microfluidic colloid. These results are shown in figure 1.41.

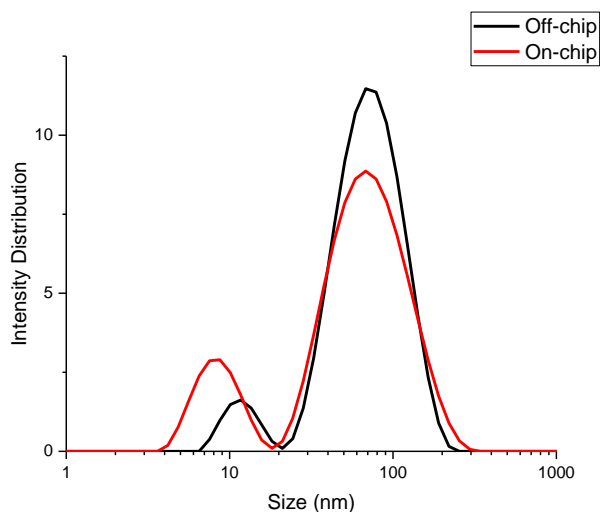


Figure 1.40: Intensity weighted DLS size distribution results for both batch (black) and on-chip (red) prepared hydroxylamine reduced silver particles. Size distribution is for a single batch experiment and from a single device.

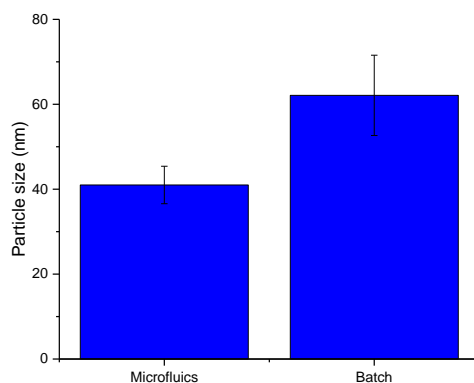


Figure 1.41: Z-average size of hydroxylamine reduced silver particles prepared in batch and on-chip synthesis. Results are the average of results from three separate batches and three separate devices. Error bars are one standard deviation.

The results showed that there was some variation between the two colloids, particularly in the size as indicated by DLS. Plasmonically the colloid formed on-chip is very similar to that made in a traditional batch method. Zeta potential was recorded for both groups and was the same at -46 mV for both. The DLS and

extinction results gave slightly different conclusions regarding the particle size. The difference in extinction between batch and microfluidic colloid was only slight, indicating that the metallic core of the nanoparticle is very similar between the two methods. The apparent larger particle size indicated by the DLS could be contributed to by two causes. Firstly, the batch nanoparticles may have a larger hydrodynamic radius due to a thicker stern layer of ions. Secondly, the batch colloid size may have increased in size over time due to Ostwald ripening. This where the small particles will merge into the larger particles and could be the reason for the reduced intensity of the small peak in the batch colloid DLS.

Importantly, when using the devices to conduct the protein detection, the device to device variation was similar to batch to batch variation. This means that the reliability of the detection should be similar to a batch assay, as a major contribution to the variability in nanoparticle based assays is the quality of the colloid used.

To confirm that the functionalisation of silver nanoparticles with PEG was effectively carried out in the microfluidic device, the device was run with the sample inlet blocked (i.e. only silver nitrate, hydroxylamine and PEG linker were run through the device). As a control for these experiments, the PEG sample was replaced with water (blank). An initial test of the functionalisation was to measure the size by DLS. There were some problems with this relatively straight forward measurement however. As shown above hydroxylamine reduced silver nanoparticles have a very high polydispersity and multimodal distribution when measured by DLS. This means the integral calculations to determine the z-average size from the photon correlation counts may not give a good representation of the true size. The measurement did give some indication of the functionalisation state by showing the increase in size as the PEG molecule conjugates to the surface. The PEG molecule ($M_w = 635 \text{ g mol}^{-1}$), in a straight chain conformation, was about 5 nm in length, so the increased hydrodynamic radius should be visible in the z-average size.

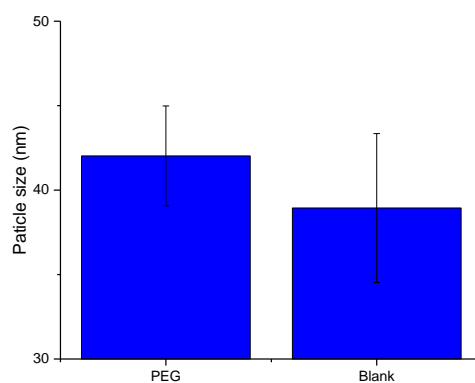


Figure 1.42: Z-average size for hydroxylamine reduced silver particles prepared and functionalised on-chip with PEG and with no conjugation (blank). Results are the average of results from three separate batches and three separate devices. Error bars are one standard deviation.

For these device prepared colloids, the particle size is plotted in figure 1.42. The z-average size of the blank sample (with no PEG) was 39.0 ± 4.4 nm, with PEG the size was 42.0 ± 3.0 nm, an increase of 3 nm. The standard deviation of both samples was similar to this difference so the statistical significance of this difference is likely to be weak. However, it did tentatively indicate that the PEG had attached to the surface.

As the DLS sizing results uncertainly indicated an increase in size with PEG conjugation, a second test of PEG conjugation was conducted. This relied on the protective ability of the PEG molecule. It is known that addition of excess salt can cause the non-specific aggregation of silver nanoparticles, however protection by PEG can prevent this. Aggregation is indicated by the generation of new plasmon modes which cause a broadening and flattening of the observed plasmon extinction. This spectral change can be quantified by plotting the ratio of extinction at 600 nm to the plasmon maximum extinction (figure 1.43); higher ratios indicate a more aggregated colloid. This ratio for the prepared PEG sample showed a slight increase over the blank sample, possibly due to some slight aggregation during the functionalisation or the change in surface chemistry. Addition of 50 mM NaCl to the colloids showed a significant difference in response between the PEG sample and the blank. With no protective functionalisation, the ratio of 600 to plasmon extinction for

the blank sample increased greatly. The PEG sample, with the same NaCl concentration, showed no significant change over the sample without salt. This indicated that the bare colloid non-specifically aggregated with the salt but the PEG protected colloid did not.

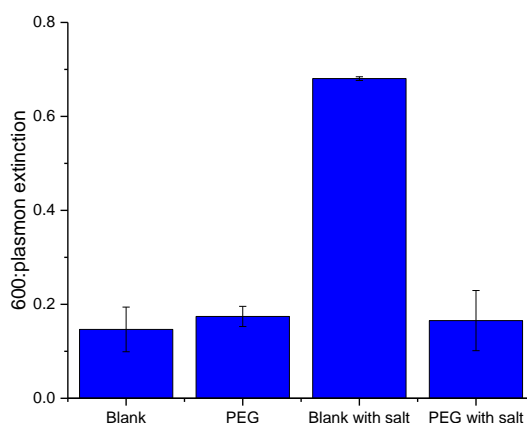


Figure 1.43: 600: plasmon ratio for hydroxylamine reduced silver nanoparticle samples prepared on-chip with PEG and blank control, both with and without 50 mM sodium chloride. Ratios are the average of three devices for each condition with error bars of one standard deviation.

Combining these two results it can be concluded that the PEG does functionalise the silver colloid in the device, as a size increase was observed along with a great increase in the stability at high salt concentrations.

1.4.3 Raman Spectroscopy On-Chip

Having shown that the in-line mixer and controlled flow rate ratios facilitated functionalisation with PEG, the functionalisation with a Raman reporter molecule and detection of this on-chip by Raman spectroscopy was then tested.

Initially only a Raman active dye was added through the functionalisation stream (i.e. no PEG linker included). Experiments were conducted to test whether this could be detected by SERS or normal Raman spectroscopy on-chip. The dye used was a

benzotriazole dye prepared in the research group [90], named as RB1 (structure shown in figure 1.44 with the IUPAC name).

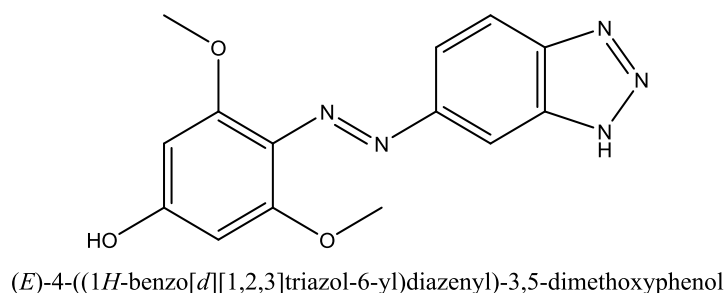


Figure 1.44: Structure of the RB1 dye used in Raman experiments with the full chemical name.

The normal Raman spectra of RB1 (figure 1.45) showed a peak from PDMS at 1400 cm^{-1} [91] and two sharp peaks, observed in all samples with low Raman counts, at 1450 cm^{-1} and just above 1500 cm^{-1} . Off-chip, in a glass cuvette, only the sharp peaks at 1450 cm^{-1} and just above 1500 cm^{-1} were present. No peaks from RB1 were evident in the Raman spectra. As the two sharp peaks are very sharp, they likely do not correspond to a Raman scattering peak. The lines were observed at the same Raman shift, excluding the possibility of cosmic rays. They are therefore likely to be incident light from the room or an interrogating laser light sideband which is entering the laser optics.

With the silver nanoparticles to act as an enhancing substrate, the Raman spectra of RB1 could easily be observed as shown in figure 1.46. The quadrant stretching modes at around 1600 cm^{-1} and the vibrational modes involving the aromatic ring and azo group at 1360 cm^{-1} being the most obvious signature peaks of the dye [90]. On-chip, it could be seen that the PDMS peak at near 1400 cm^{-1} , had much greater counts than was observed without nanoparticles (greater than 20,000 counts with the silver nanoparticles compared with 500 counts with only the RB1 solution). This indicated that the SERS signal from the PDMS was observed, caused by silver nanoparticles at the top surface of the microfluidic channel. The strongest RB1 signal was observed at

the top of the channel and coincides with strongest PDMS signal, suggesting aggregation at this surface.

Adding RB1 into the device to functionalise the on-chip prepared colloid appeared to work relatively well, as the surface enhanced signal was observed on-chip. Using the device, it was possible to prepare colloid, immediately functionalise it with a Raman reporter on-chip and detect the dye on-chip using an inverted microscope set up. The SERS enhancement appeared to be greater on-chip than off-chip (compare 42,000 counts on-chip compared with 15,000 counts off-chip for the same concentration in figure 1.46).

Fouling of the microfluidic device was severe, as can be seen in figure 1.47, where all of the mixing channels with silver nanoparticles are darkened and the mixing stage for formation of silver nanoparticles presents almost a solid black colouring (highlighted in red). This fouling may be the reason for the higher counts on-chip than off-chip, as the fouling material is aggregated, giving a very high enhancement factors, whereas the off-chip cuvette sample was unaggregated. Some back flow is evidenced by the slight discolouration in the water channels (light brown colour evident in the channels, highlighted in the purple square).

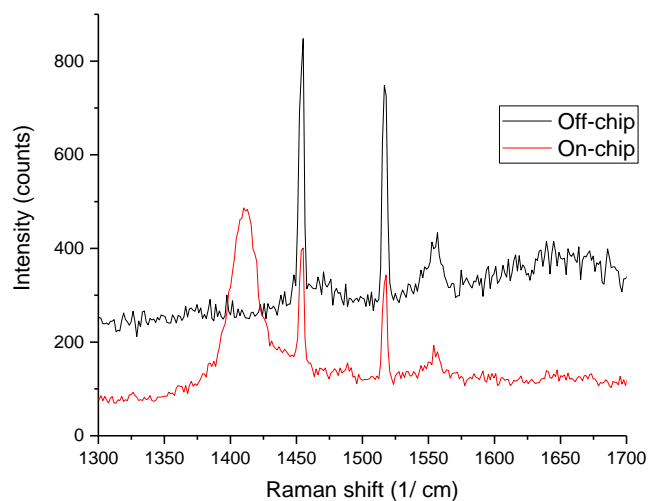


Figure 1.45: Raman spectra of 1 μ M RB1 solutions taken off- and on-chip. One accumulation of 1 s was used with interrogation at 532 nm. Both are single representative spectra.

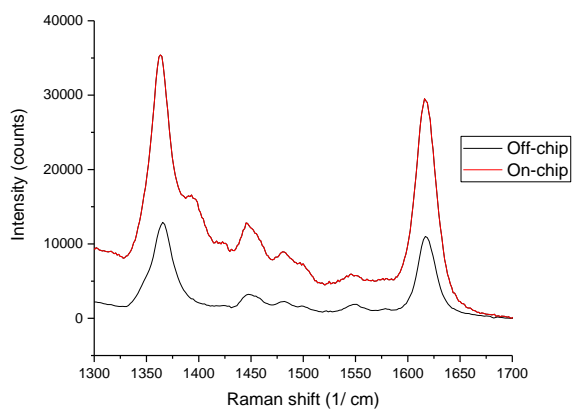


Figure 1.46: SERS spectra of 1 μ M RB1 with hydroxylamine reduced silver nanoparticles taken both off- and on-chip. On-chip samples used nanoparticles prepared on-chip. Off-chip experiments used batch prepared nanoparticles. One

accumulation of 1 s was used with interrogation at 532 nm. Both are single representative spectra.

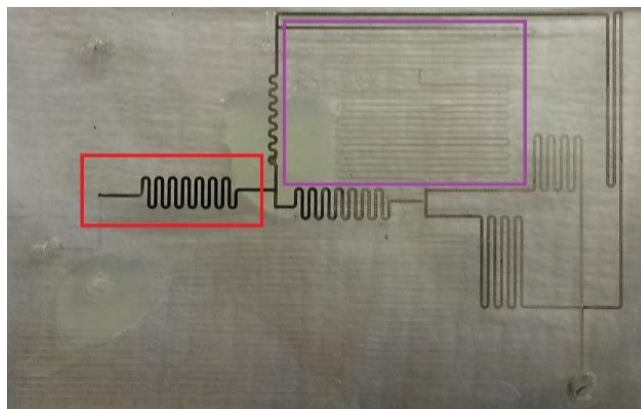


Figure 1.47: Picture of microfluidic device after use showing fouling of the channels by silver nanoparticles. The mixing zone to form silver nanoparticles is highlighted in the red square and the water inlet in the purple square. Note the inversion about the horizontal axis compared to above diagrams of the device.

The available evidence points to the formed nanoparticles fouling the PDMS surfaces of the channel, creating a slug of material that acted as a very effective enhancing surface. This process is shown in figure 1.48.

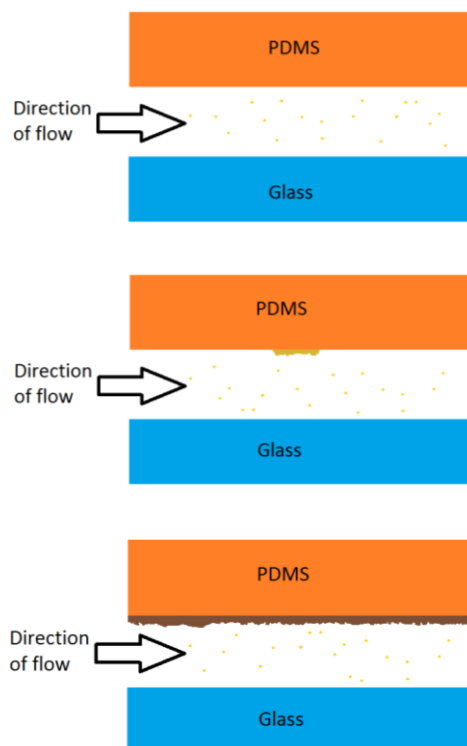


Figure 1.48: The forming silver colloid flows through the channel (a), as it flows over the PDMS it adheres to the surface (b). After some time, a film of the accumulated silver nanoparticles builds up which acts as an effective enhancing substrate but discolours the channel and eventually appeared to block flow through the device (c).

This fouling has been noted in other such devices making gold and silver nanoparticles in a microflow reactor [92], [93]. No solution has been proposed and different materials appeared to have no effect. From observations here, the adhesion to PDMS seems to be more significant than to the glass.

1.4.4 SERS Detection of ConA

The first assay attempted on-chip was an “off to on” SERS assay, this was performed by including both the carbohydrate PEG linker and RB1. The sample was also introduced. With ConA in the sample, aggregation should give a higher enhancement and higher Raman counts than without ConA.

In practice, the fouling of the device by the silver, highlighted above, severely limited the functionality of the detection on-chip. Due to the non-specific aggregation of the silver nanoparticles in the fouling material, the Raman spectra on-chip was always high and increased with time. The spectra obtained from the on-chip measurements was similar to that shown in figure 1.46. Across multiple devices, no increase in signal was observed between the control and sample channels. Due to the fouling, measurements on-chip for the “off to on” assay were not successful.

Since the on-chip measurements could not facilitate detection of ConA, the device was run and the produced sample taken off-chip for cuvette SERS analysis. This still allows all the preparation steps to be carried out but does not allow for the detection of a control and sample with the same device. Flow rate though the device had to be increased to 200 $\mu\text{L}/\text{min}$ to allow a cuvette full of sample to be collected in a reasonable time. SERS response was much weaker from the collected sample than was detected on-chip. There was no relation between the peak intensity at 1620 cm^{-1} and the presence of 100 nM ConA in the sample as shown in figure 1.49. Counts were slightly higher for the blank than the ConA sample. It was noted that there was an obvious visual difference between the two samples, with the ConA sample having a grey colouration associated with aggregation. This was supported by the extinction spectroscopy measurements on the same samples as shown in figure 1.50. The 600 nm extinction to plasmon ratio showed a clear distinction between the blank and ConA sample.

Running the device in this configuration was not ideal, as the control channels act as bypass channels for some colloid to avoid functionalisation and mixing with the ConA. Even with these problems the extinction measurement seemed to allow detection of the ConA, where the SERS measurement could not discriminate between the two.

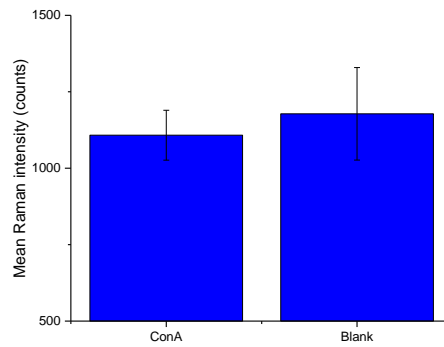


Figure 1.49: Raman counts at 1620 cm^{-1} for glucose functionalised, hydroxylamine reduced silver nanoparticle samples with 100 nM ConA and with no ConA (blank). Samples were prepared on-chip and taken off-chip for Raman analysis in a glass cuvette. Values shown are the average of three devices, with error bars of one standard deviation.

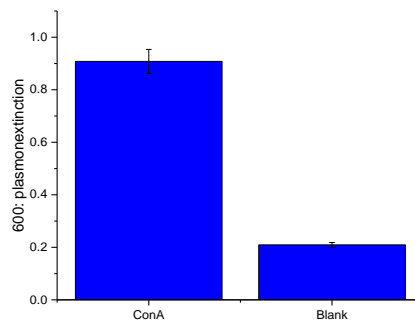


Figure 1.50: 600: plasmon extinction ratio for glucose functionalised, hydroxylamine reduced silver nanoparticle samples with 100 nM ConA and with no ConA. Samples were prepared on-chip and taken off-chip for extinction analysis. Values shown are the average of three devices, with error bars of one standard deviation.

1.4.5 Experimental Plasmonic Extinction Assay

With the extinction detection observed to be the more robust measurement, the device was used for this assay. The Raman dye was excluded and the detection would be achieved by monitoring the extinction of the colloid.

One of the limitations of employing an extinction method in place of a SERS measurement was the loss of the ability to interrogate the sample on-chip. Whereas the interrogating laser for SERS could be focused within a channel, there was no such capability available for extinction measurements. This meant that samples could not be analysed on-chip and instead were taken off-line for analysis in a cuvette based spectrometer. Due to the analysis being performed off-chip, the control channels designed into the device were redundant and could adversely affect the device operation by causing some colloid to bypass conjugation or mixing with samples. The control channels were cut off and sealed to simplify the device to that shown in figure 1.51.

The effluent from the device was collected and the extinction measured by a standard bench-top instrument. By removing some stream splits and the water inlet, the flow through the device was altered and a new circuit simulation model was made to represent this. Figure 1.52 shows this simulation. Importantly the functionalisation and sample inlets proportionally decreased in relation to the colloid flow.

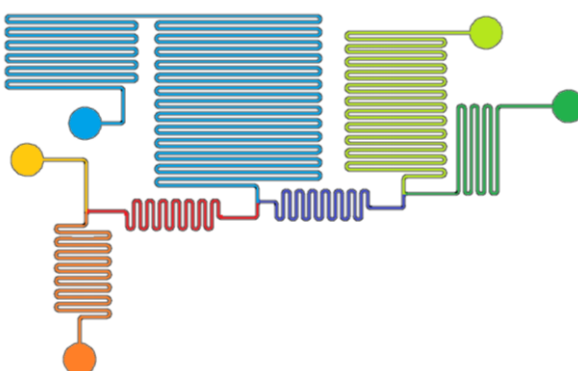


Figure 1.51: Coloured CAD drawing of the device with the control channels removed.

Silver nitrate is added in the orange channel, basic hydroxylamine in the yellow to form colloid in the red. Functionalising agent is added in the blue and conjugated in the dark blue area. Finally, the sample is added in the green and mixed with the colloid in the dark green.

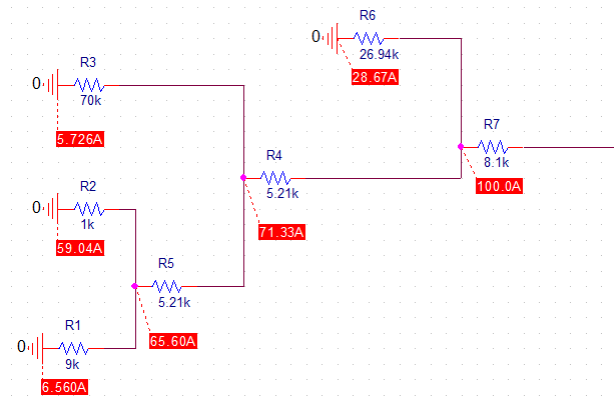


Figure 1.52: Circuit simulation model of the device with control channels removed. Resistances are shown, as are the currents in red for a total current of 100 A (current source not shown). The overall layout of the stream inlets corresponds to that in figure 1.51.

Adjusting to the cuvette based system required an increase in flow rate to generate a sufficient sample volume in a reasonable time. The flow rate was increased to 200 $\mu\text{L}/\text{min}$. To check that the device still matched the simulated values with the increased flow rate and new device configuration, the flow rates were tested again by introducing a dye to each inlet and calculating the fraction of total flow through each inlet. Results are shown in figure 1.53. The error from device to device was higher in this configuration but the average flow through each inlet was still a good match for that modelled in circuit simulation. It is possible that the increased variation from the model value was a result of the increased Re , which will increase the observed effects from elements such as the SHM and channel bends. Flow was still laminar but Re was increased to 28.

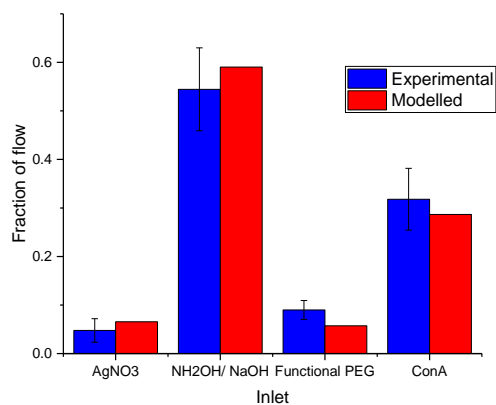


Figure 1.53: Comparison of the fraction of flow through each inlet of the reduced device shown in figures 1.51 and 1.52. Experimental values are given in blue with modelled values in red. Values shown for the experimental result are the average of five devices, with error bars of one standard deviation.

Running the complete device in this configuration and performing the detection was carried out. As a control to check that the specificity of the interaction was maintained, a second carbohydrate was conjugated to the nanoparticles. The two sugars are very similar so were challenging to discriminate through the on-chip preparation and interaction. Nanoparticles functionalised with glucose (glu-NP), or galactose (gal-NP) were prepared on-chip. ConA has a binding affinity for glucose but not galactose, so only glu-NP particles should exhibit aggregation with the lectin. Extinction spectra were taken for the glu-NP, both with and without ConA, and gal-NP with ConA (figure 1.54). The glu-NP without ConA have very similar extinction spectra to the gal-NP mixed with ConA. This demonstrates that the gal-NP do not interact significantly with ConA. In contrast, the extinction spectrum of the glu-NP broadens substantially and red-shifts with the addition of ConA, indicating aggregation.

This result was emphasised further when the ratio between extinction at 600 nm and plasmon extinction was calculated (Figure 1.55). It was evident that the gal-NP had little association with the ConA, as the ratio of 600 nm: plasmon maximum extinction remained similar to that for the sample with no ConA. The specificity of the

carbohydrate functionalised nanoparticles was shown by the strong interaction between only the glu-NP and ConA. This again highlighted that the silver nanoparticles could effectively be functionalized on-chip, due to the efficient mixing and the full preparation method maintained the specificity of the nanoparticles sensors. The functionalisation was extensive enough to protect the silver nanoparticles from non-specific aggregation in the metal ion contain buffer.

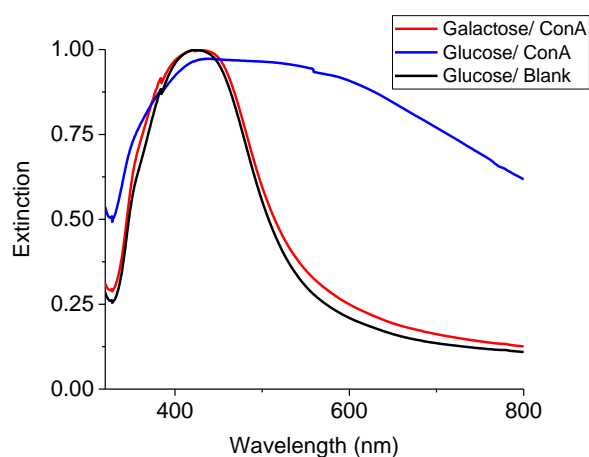


Figure 1.54: Extinction spectra for glucose (blue) and galactose (red) functionalised hydroxylamine reduced silver particles with 50 nM ConA and glucose functionalised hydroxylamine reduced silver particles with no ConA (black). Assay was performed on-chip and taken for off-line analysis. Results are for single representative spectra.

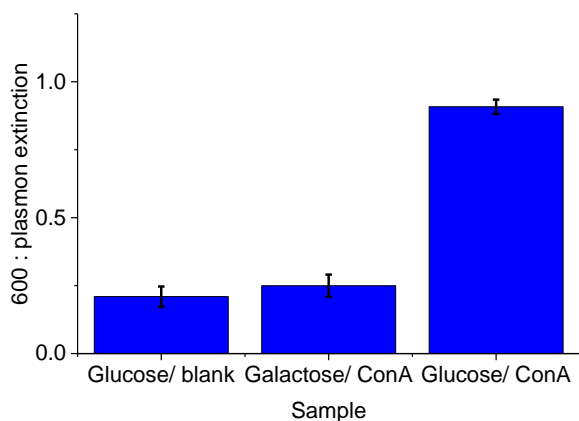


Figure 1.55: 600 nm plasmon extinction for galactose and glucose functionalised hydroxylamine reduced silver particles with 50 nM ConA and glucose functionalised hydroxylamine reduced silver particles with no ConA (blank). Assay was performed on-chip then taken for off-line analysis. Results are averages of three devices for each condition. Error bars are one standard deviation.

The ConA concentration demonstrated here was similar to the best detection limit shown for previous assays for ConA and exceeded the detection limit shown when using silver nanoparticles [94] (100 nM for silver, 40 nM for gold). The detection showed that the chemistry for preparation and functionalisation of metal nanoparticle biosensors can readily be transferred to a lab-on-a-chip, with no loss in sensitivity. The extensive aggregation with the ConA and glucose nanoparticles was evident visually by the change in colour. This suggests that an instrument free, qualitative detection employable at point of sampling could be viable using this device.

Since the on-chip detection had been demonstrated at lower concentrations than the previous limit for silver nanoparticles, a concentration study was carried out both on-chip and off-chip to see how the two compared. Off-chip, the ratio of 600 nm extinction to plasmon maximum is well represented by a linear trend between 0 nM and 80 nM. At 100 nM the ratio decreased, as shown in figure 1.56, caused by the formation of aggregates which precipitated from suspension.

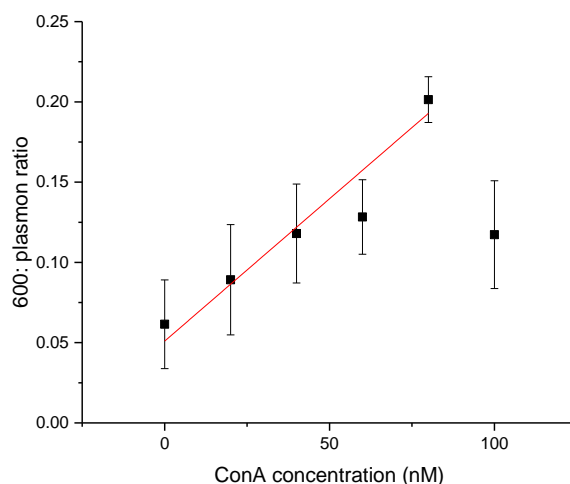


Figure 1.56: Concentration curve of 600: plasmon ratio for glucose functionalised hydroxylamine reduced silver particles with ConA concentration, as determined in off-chip experiments. The linear trend is shown for points between 0 and 80 nM. Results are the average of three experiments with error bars of one standard deviation.

Initially covering the same range using on-chip detection, no obvious linear range was observed. Instead a step change was evident, with lower ratios below 45 nM and higher ratios above this value. This is shown in figure 1.57.

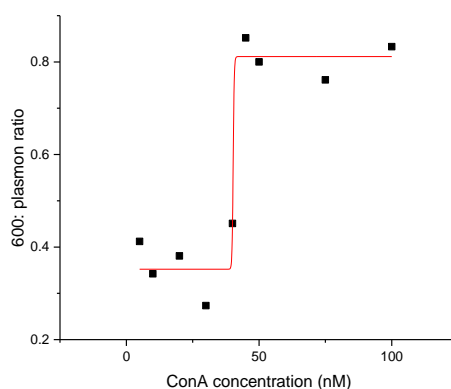


Figure 1.57: Concentration curve of 600: plasmon ratio glucose functionalised hydroxylamine reduced silver particles with ConA concentration. The assay was

performed on-chip then taken for off-line analysis. The step change trend is plotted for all points. Results are for a single device at each concentration.

The current analytical response of the on-chip assay falls short of what would be required for performing a quantitative assay. These results demonstrated that the on-chip ConA assay does however offer the capability of performing a qualitative assay for detection of the protein at concentrations above 45 nM.

The failure of the on-chip assay to reproduce the analytical response of the off-chip assay was likely due to the chemistry employed, rather than an inherent limitation of the LOC concept. In the on-chip assay, the preparation of the carbohydrate PEG linker requires excess aminated sugar and the reaction product was used without clean-up. Off-chip, the nanoparticle probes are purified from reagents and side products by centrifugation but an equivalent technique was not employed on the LOC device.

1.5 Conclusions

This work has demonstrated the development of a microfluidic device for the integration of all steps in detection of a lectin. At the point-of-use, results could be obtained within less than five minutes of introducing the protein sample, significantly accelerating analysis time over bench-top scale chemistry. Initial results appeared comparable to batch results with some challenges around analytical response, probably due to difficulty in separation of the functionalised nanoparticles.

These results show the electrical circuit analogy can be used to ease the transfer of bench-top chemistry to a lab-on-a-chip device. This represents one of a limited number of demonstrations of how computationally inexpensive simulations can inform design of negative pressure microfluidic devices, greatly reducing the experimental cost and simplifying the transition to a LOC device. A device was designed and modelled for the generation of silver colloid, functionalisation and detection of ConA. This was the first report effectively combining electrical circuit modelling and passive mixers to allow a full analytical procedure to be carried out on-

chip. Practical testing proved the utility of these models and the capability of accurate fabrication to match designs in final devices.

Silver nanoparticles could be formed on-chip and were very similar to those formed in traditional batch chemistry. The chemistry and mixing ratio were directly transferred from the bench-top work into the LOC device, requiring no modification. Conjugation with both a PEG based linker and Raman reporter molecule were demonstrated on-chip, allowing very rapid generation of small volumes of functional nanoparticle conjugates.

The conjugation of the Raman reporter RB1 also showed the utility of the device in performing the complete detection of a Raman active species in the device. The inclusion of colloid synthesis makes the on-chip procedure very efficient in terms of material and time use. For detection of the Raman signal from an analyte, the aggregation of nanoparticles in the device means that high SERS enhancements can be obtained, without the requirement to add an aggregating agent.

The SERS detection of ConA using on-chip preparation proved challenging, with problems facing both on-chip detection and removing on-chip prepared samples for off-chip analysis due to the noted non-specific aggregation of the formed colloid.

ConA was however sensitively and rapidly detected at a concentration of 50 nM, with all pre-detection steps being performed on-chip with very little operator input. The on-chip preparation maintained the high selectivity of the interaction, allowing distinction of different epimers of the interacting sugar. Employing off-line analysis negated some of the advantages of the LOC analysis but the device still allowed all pre-detection steps to be carried out in less than five minutes and allowed very efficient use of materials, as reagents were all consumed as required, not in large batches. The LOC device also allowed the full procedure to be carried out without any physical handling such as pipetting or measuring.

1.6 Further work

Specifically relating to the ConA detection assay, the most obvious next development is further investigation into the analytical response of the assay performed on device. This would further inform the comparison between the assay performed on the LOC and on the bench-top. The calculated limit of detection and development of an on-chip assay with a greater linear range would be useful in determining the applicability of the LOC to performing assays. Both a sufficiently low limit of detection (visual or instrumental) and a reliable response are essential for the LOC to perform useful chemistry.

The analytical response is likely to be improved in terms of the linearity of response and the detection limit by tuning the chemistry of the assay for use in the lab-on-a-chip. In the work shown above, optimal linker concentrations in the final device were not determined. The linker preparation, which is most often carried out with the PEG substrate bound to the nanoparticles could be improved by addition of a clean-up step. This is likely to reduce the excess free carbohydrate in the final solution and could be done by either dialysis or chromatography.

Modification of either the chemistry on-chip or the reactor materials to allow both assays to be performed on-chip would be a longer term target for the ConA detection. This would allow the full advantages of the designed device including lower reagent consumption and in-built control channels to be realised. It is likely that a successful SERS assay would have a lower detection limit than a comparable nanoparticle colourimetric assay and would therefore be more useful for a highly sensitive laboratory detection. The colourimetric aggregation assay could be enhanced by using a smaller optical system (such as a fibre optic probe and portable detector) which permits focus of the interrogating light into the microfluidic channel.

As a further proof of the concepts shown here and to show applicability to further bioanalysis, a device for the detection of a target DNA sequence was designed but not fabricated. The device is shown below in figure 1.58. This design was larger than the ConA device and was intended to utilise the maximum amount of space available

on the printed wafer, but still be useable in only a single device. The intent of this device was to make a colloidal nanoparticle stream and split it in two; two separate single strand DNA sequences could then be conjugated to the nanoparticles rapidly using low pH conjugation. These probes would be complementary to a target DNA strand and would hybridise. The presence of multiple probes on each nanoparticle would cause aggregation with hybridisation to the target DNA. The detection method proposed was the same as for the ConA assay shown above.

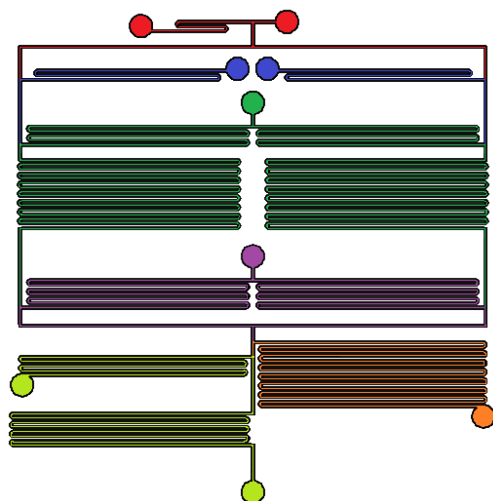


Figure 1.58: Drawing for the DNA detection device. Silver colloid is produced in the red section and is functionalised in the dark blue. The mix is then conditioned with buffers in the dark green, purple and orange sections. Sample is introduced in the lime green section.

As shown in figure 1.58, colloid was to be produced by hydroxylamine reduction in the red section, before being split and mixed with two separate DNA probe sequences in the dark blue areas. The mixture was then conditioned with a low pH citrate buffer in the dark green section and allowed to mix. A neutralizing phosphate buffer was then added in the purple section before the two nanoparticle streams were recombined. A DNA hybridisation buffer was to be added in the orange section and the DNA sample would be added in the light green stream.

The main challenges predicted for this design were the multiple buffer conditioning steps and sequential long mixing steps to functionalise the colloid and then allow probe-target hybridisation. If successful, this would have further shown the applicability of the combination of nanoparticle aggregation assays and LOC microfluidics. Batch experiments were run to determine how successful the assay could be with the limited time for mixing on-chip and the lack of any clean up steps. It was found that with around 650 DNA probes per nanoparticle, the assay could be run without any centrifuge steps and still showed aggregation with 10 nM target and no aggregation with a non-complementary control, as evidenced in figure 1.59.

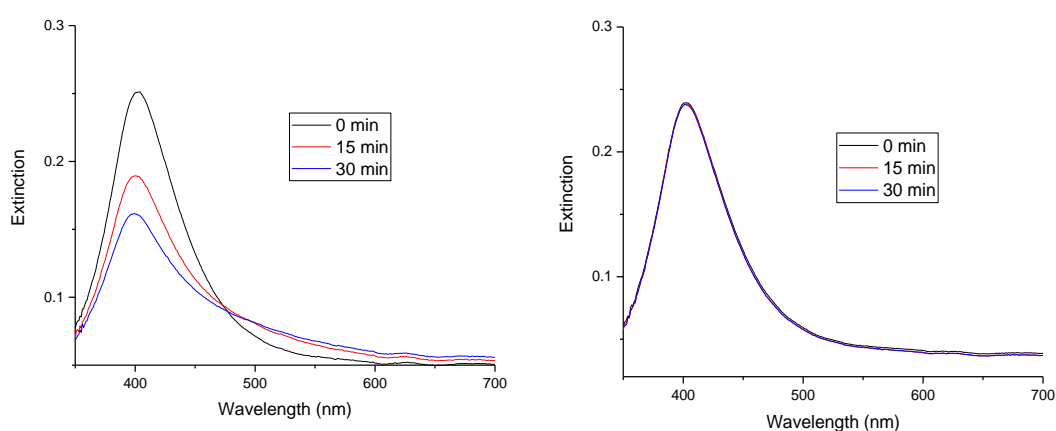


Figure 1.59: Comparison of nanoparticle DNA probes with complementary sequence (left) and non-complementary control (right) over time. Results are preliminary and are given for single experiments.

The fabrication and construction of this device should be relatively similar to the ConA detection device and operation should be similar. It would prove the applicability of the lab-on-a-chip device with nanoparticle aggregation assays to a more demanding assay, requiring multiple buffering steps and conjugation and hybridisation events.

1.7 Experimental

1.7.1 Reagents

All chemical reagents were purchased from Sigma Aldrich and were of the highest quality available. Concanavalin A was type vi, also obtained from Sigma Aldrich. Reagents and the lectin were used as obtained with no pre-treatment. Food grade red colouring was used in determining mixing ratios in chip. Thiolated DNA sequences were obtained from ATDBio and were purified by HPLC.

1.7.2 Batch Nanoparticle Preparation

Hydroxylamine reduced silver nanoparticles were prepared as reported by Leopold and Lendl [70]. The nanoparticles were used as prepared after being left overnight for the particles to ripen.

1.7.3 Carbohydrate Linker Preparation

To prepare a suitable functional ligand, thiol/carboxyl heterobifunctional polyethylene glycol, was coupled to an aminated carbohydrate by amide coupling with 1-ethyl-3-(3-dimethylaminopropyl)carbodiimide / *N*-hydroxysulfosuccinimide chemistry. The use of aminated sugars allows conjugates with different surface glycans to be prepared; in this case both galactosamine and glucosamine were used. The overall reaction scheme is shown in figure E1.1 for the preparation of a glucose linker.

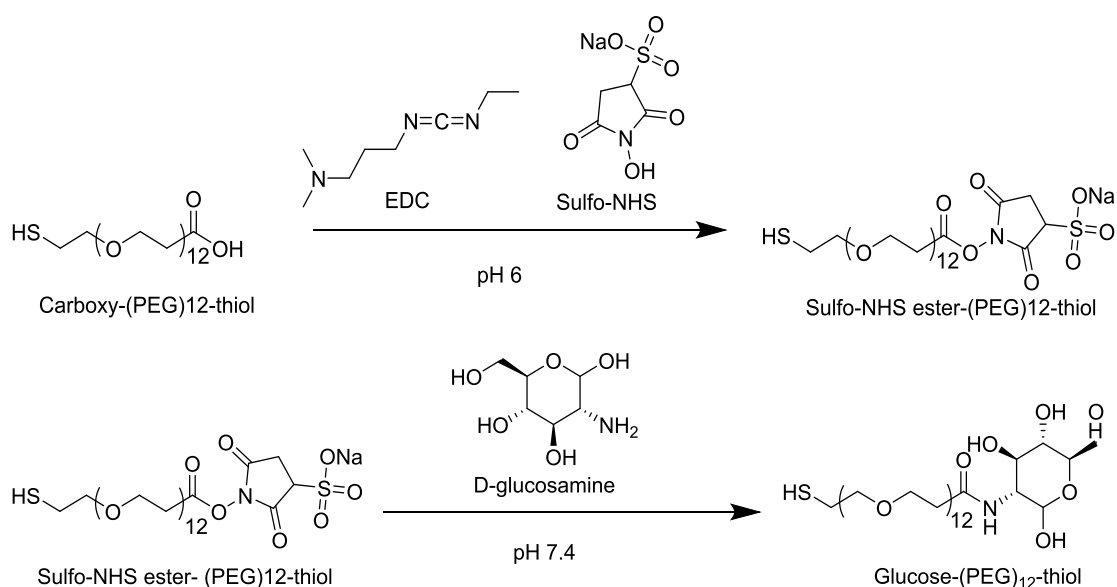


Figure E1.1: Schematic showing the preparation of a carbohydrate linker with glucose via amide coupling of carboxylic acid terminated PEG and aminated carbohydrate.

Carbohydrate conjugates were prepared on a 1.7 mL scale. Five separate solutions were prepared and are detailed below.

100 μL of carboxy-PEG₁₂-thiol solution was initially prepared in a 10 mM pH 6 MES buffer (10 mM carboxy-PEG₁₂-thiol, 0.6 mg in 100 μL).

500 μL of a solution of the hydrochloride salt of an aminated carbohydrate was prepared in a 10 mM pH 7.4 HEPES buffer (156 mM aminated sugar, 16.8mg in 500 μL).

200 μL of a 1-Ethyl-3-(3-dimethylaminopropyl)carbodiimide (EDC) solution in 10 mM pH 6 MES buffer was prepared (151 mM EDC, 4.7 mg in 200 μL).

200 μL of an N-Hydroxysulfosuccinimide sodium salt (sulfo-NHS) solution in 10 mM pH 6 MES buffer was prepared (225 mM sulfo-NHS, 9.8 mg in 200 μL).

700 μL of a sodium hydroxide solution in doubly distilled water was prepared (10 mM sodium hydroxide, 0.28 mg in 700 μL).

Both the ECD and sulfo-NHS solutions were added to the PEG solution and mixed for 1 hour. The aminated sugar solution was added and mixed for a further hour. The sodium hydroxide solution was then added to raise the pH to 7.5-8 and mixed for 16 hours.

1.7.4 Instrumental Analysis

Dynamic light scattering results were recorded in a Malvern ZS zetasizer with a 633 nm laser. The number of runs per sample was determined by the in-built software. Results presented are the intensity size distribution directly from the instrument. Where single sizes are quoted these are the z-average size and are calculated by a standard method reported to conform to ISO 13321.

Zeta potential measurements were recorded in a Malvern ZS zetasizer with a 633 nm laser. The number of runs per sample was determined by the in-built software. Potentials presented are the results of the zeta distribution directly from the instrument.

UV-Visible spectrophotometry was carried out using a dual-beam Cary-Win UV 300 spectrometer recording extinction between 800 – 300 nm with a resolution of 0.5 nm.

Disposable poly(methyl methacrylate) cuvettes were used for DLS, zeta potential and extinction measurements. Samples were made up to 400 μ L for extinction measurements and 600 μ L for zetasizer measurements. Samples prepared on-chip were used as obtained from the device. Where comparison was made with batch prepared particles, dilutions were used to match those measured on-chip.

Fluorescent microscopy was performed on the microfluidic chip with an Olympus MVX10 microscope and images taken with the instrument software.

Raman measurements for on-chip experiments were taken using a Renishaw InVia system coupled to an inverted microscope with a 20x long working distance

objective. The laser interrogation power was 20 mW at a wavelength of 514.5 nm using an argon laser. For the spectra produced, one interrogation of 1 second was used. Spectral resolution was less than 2 wavenumbers and the static scan used was centred at 1360 cm^{-1} . The same set up was used for off-chip measurements but a glass cuvette was used for the solutions obtained directly from the device. For comparison with batch prepared particles, the colloid was diluted to match the ratios measured on-chip and the corresponding final concentrations.

1.7.5 Designing the Microfluidic Device

A rough design of a corresponding electrical circuit was designed in cadence orCAD electrical circuit simulator. Design drawings were then made using Autodesk AutoCAD for initial designs of a microfluidic device. Channels were $200\text{ }\mu\text{m}$ wide and terminated in a 1 mm diameter hole that could be punched to form an inlet. The channel was to be $70\text{ }\mu\text{m}$ tall and the mixing pattern was to be imprinted to a $20\text{ }\mu\text{m}$ depth. Designs were restricted to a surface of 39 mm by 25 mm to ensure they would fit on a silicon wafer comfortably. Designs were then block coloured such that areas to be raised in the master mold (i.e. channel interior) were transparent and other areas were dark. The design was then printed onto a transparency by CAD/ Art services Inc. to generate the photo mask.

In a clean room with orange lighting to prevent premature photoreaction in photoresist solutions, a silicon wafer was washed in hydrofluoric acid for five minutes. The wafer was then rinsed thoroughly in deionised (DI) water, acetone, methanol and DI water again before being dried under nitrogen flow. The wafer was then spin coated in SU-8 2000 series photoresist solution from MicroChem Corp. The rotational velocity was given by instructions provided with the photoresist solution. For the first coating on which the main channels would be developed SU-8 2050 was spun at 2300rpm for 30 seconds with a pre-spin of 500rpm for 30 seconds. This was then soft baked at 65°C for 3 minutes then 9 minutes at 95°C ; exposed under the

mask for 42 seconds to UV light (wavelength 365 nm) in a Karl Suss mjb4 mask aligner before a post exposure bake at 65°C for 2 minutes then 7 minutes at 95°C.

The wafer was then spin coated in SU-8 2015 at 2100 rpm for 30 seconds with a pre-spin of 500 rpm for 30 seconds to generate the layer for mixing channels to be developed on. This was then soft baked for 4 minutes at 95°C; exposed under the mask for 26 seconds to UV light (wavelength 365 nm) in a Karl Suss mjb4 mask aligner before a post exposure bake for 5 minutes at 95°C. The wafer was then developed in the SU-8 developer solution for 10 minutes with constant agitation before moving the wafer to fresh solution for one further minute. The wafer was then rinsed in isopropyl alcohol and dried under nitrogen. Channels were checked under a white light optical microscope for defects and the height of the features were measured by a KLA Tencor alpha step 500.

To facilitate the matching of the two layers accurately a line mark was used on each of the layers as shown in figure E1.2.

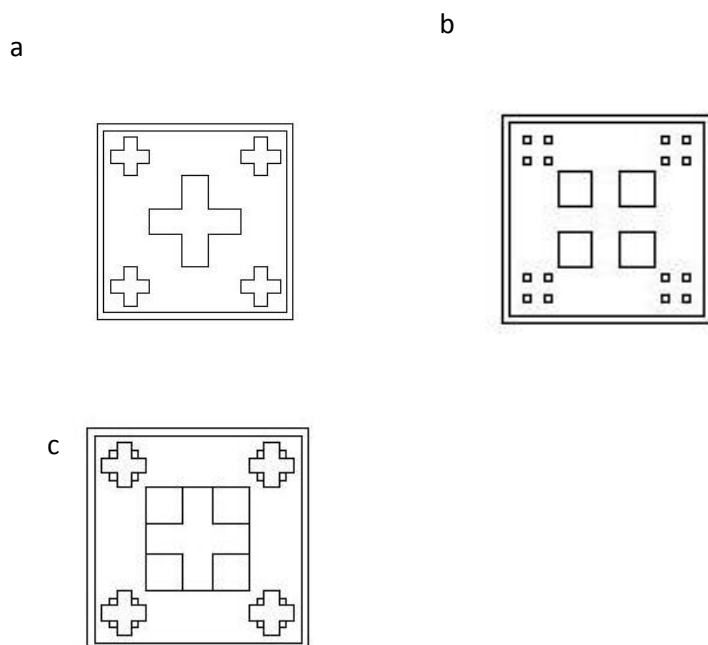


Figure E1.2: Line marks used in the exposure of the device showing (a) bottom layer mark, (b) top layer mark and (c) combined line mark. The bottom layer mark is imprinted in several places on the base SU-8 layer and the top photomask is aligned using the top layer mark before exposure.

The wafers were then left overnight in a vacuum desiccator with 1H,1H,2H,2H-perfluorooctyltriethoxysilane. 30 minutes was sufficient for evaporation and reaction with the wafer surface; the wafer was now suitable for use as a mold since the PDMS could be cast into it and removed relatively easily due to the fluorinated surface of the wafer.

PDMS solution was prepared by mixing 10 parts of sylgard 184 with 1 part of its curing agent, both from Dow Corning Corp., for a total weight of approximately 16 g. The mixed sylgard was then left for 30 minutes under vacuum to remove suspended air bubbles. The sylgard was then poured over the mold and heated for two hours at 80°C to cure the polymer. Once cured, the PDMS was slowly removed from the mold, inlet holes were punched and the device was cut from the excess PDMS. Removing

the PDMS from the mold too quickly can result in the SU-8 being damaged as is shown in figure E1.3, where the SU-8 can be seen in the corners of the PDMS cast SHM.

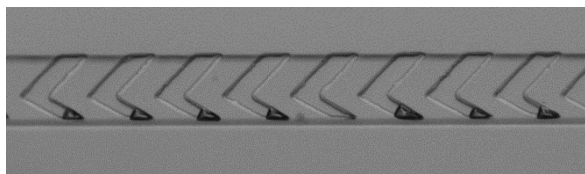


Figure E1.3: Image of broken SU-8 in the PDMS channels showing the potential effects of improper removal of devices from the master mold. Note also the minimal misalignment of the edges of the SHM with the channels.

Any adhering dust or particles were removed from the underside of the PDMS with sticky tape and a clean glass slide and the PDMS device were placed in an oxygen plasma cleaner for 30 seconds with a power of 100 W. This generated a reactive silanol surface on both, such that when they were placed together a permanent bond formed. The device was transferred to an oven at 120°C overnight

1.7.6 Running the Microfluidic Device

The outlet of the microfluidic device was connected to a syringe in a Cole-Parmer 74900 series syringe pump set to withdraw 200 μL / hr or 200 μL / min, as detailed in the text. Connections to the device were made by disposable plastic pipette tips glued in place with epoxy resin. This pipette tip was connected to the syringe by silicone tubing. Pipette tips similarly attached were used as reagent reservoirs for the device.

Solutions of each of the reagents were prepared fresh for each experiment. All were prepared on 10 mL scale, except the carbohydrate linker which was used as produced.

Sodium hydroxide/ hydroxylamine hydrochloride: 3.33 mM NaOH/ 1.67 mM NH_2OH .
HCl (1.3 mg NaOH/ 1.2 mg NH_2OH . HCl in 10 mL)

Silver nitrate: 10 mM AgNO_3 (17 mg AgNO_3 in 10 mL)

Carbohydrate linker: used as produced at approximately 0.6 mM

RB1 dye solution: 22 μM solution, prepared from stock solution kept at 4°C in the dark.

ConA: 200 nM ConA (0.2 mg in 10 mL of lectin testing buffer)

Lectin testing buffer for ConA: pH 7.4 HEPES buffer with 0.2 mM Ca^{2+} and 0.2 mM Mn^{2+} (3.3 mg $\text{Ca}(\text{NO}_3)_2$ and 3.6 $\text{Mn}(\text{NO}_3)_2$ in 100 mL HEPES buffer)

Around 500 μL of each of these was dispensed into the pipette tips attached to the respective inlets to the device just before turning on the syringe pump and beginning operation of the device.

1.7.7 Fluorescence Imaging

To test mixing in the device a 1 mg/ml solution of fluorescein sodium salt was added at the inlet used for silver nitrate. This meant that the fluorescein stream would mix with every other stream in normal operation. Fluorescence images could then be taken at each junction and the mixing qualitatively assessed using the images produced. Flow through the device in this experiment was maintained by a KDScientific 210 syringe pump set to withdraw 200 $\mu\text{L}/\text{hr}$ from the outlet.

Images could be quantitatively assessed by using imageJ software and analysing the average pixel brightness over a line one pixel broad, across the full channel width. This gives a figure for the mean pixel brightness and the standard deviation.

1.7.8 Flow Ratio Test

To test the mixing ratios on-chip, a red food colouring was introduced to each inlet successively. A suitably diluted stock of the red food colouring was prepared and used for all inlets. The stock and effluents from the device, with food colouring at different

inlets, were collected and analysed separately. By comparing the absorption value of the stock and different outputs from the device, the dilution ratio and hence contribution to total flow of an inlet could be calculated.

1.8 Appendix A: Diffusion Mixing in the Microfluidic Device

In this example two confluent streams of silver nanoparticles and a small functionalising molecule are present. Both streams are assumed to be pure at the start of the stream, be completely laminar and with no flow to assist mixing. Diffusion is therefore the only stream mixing force. The time for diffusive mixing is given by Einstein's equations of Brownian motion [95]:

$$t_{mix} = \frac{\text{mixing length}^2}{2 \times \text{diffusivity}}$$

Variable	value
mixing length	100 μm
diffusivity (typical small molecule) [96]	$5 \times 10^{-10} \text{ m}^2/\text{s}$
diffusivity (silver nanoparticles- 50 nm) [97]	$5 \times 10^{-12} \text{ m}^2/\text{s}$

Mixing time is given for the half channel width; assuming that the streams are mixing 1:1, and assuming Brownian motion to travel only across the channel width (i.e. neglect molecular diffusion in the vertical plane). The time for the silver nanoparticles to diffuse across the channel is 1000 seconds (17 minutes); the time for the small molecule is 9 seconds. A functionalised colloid stream is therefore obtained in a reasonable time potentially however the stream would be extremely inhomogeneous with the colloid stream only fully mixing after more than 17 minutes.

An approximate profile (figure AA.1) for the components in this representative stream can be plotted as time progresses. This represents how far across the channel the component can diffuse.

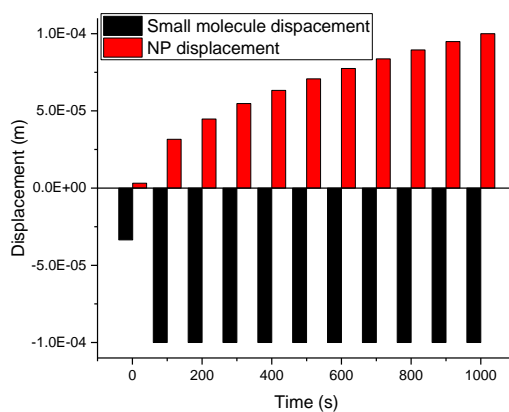


Figure AA.1: Displacement of nanoparticles and a small molecule from the centre line of the channel over time.

After approximately 9 seconds the small molecule has completely diffused from the initial laminar boundary at the centre line to the far wall of the device. However, the limiting boundary for the nanoparticles continues to change over time. This means that the concentration of nanoparticles within this volume is changing as a function of time and therefore displacement down the microfluidic channel. It is not possible to reliably make any SERS measurements or assumptions based on a homogeneous stream until mixing is complete. It is also not possible to compare between experiments without highly accurate recording of the downstream position and a very stable flow in the device. It is therefore highly impractical to use only diffusion mixing, especially for streams involving nanoparticles. Small molecule mixing is much more rapid.

This appendix assumes that all diffusion is in one direction; whereas it is equally likely for a molecule to diffuse back towards the centre or back into the side of the stream on which it started. It gives a value for a minimum time for mixing and at best an order of magnitude for how long this is likely to take. Since a mixing design is present within the device it can be assumed that the mixing due to diffusion is negligible in the short distances between confluence and SHM mixing.

1.9 Appendix B: Simulation of Fluid Flow through the SHM

As outlined in the main text, the herring bone mixer was modelled compared to a standard channel in Comsol 4.0 multiphysics engine. The herring bone mixer was modelled in the inbuilt CAD system as a single element of water at 25°C. Meshing was left as standard free tetrahedron with a maximum element size of 25 μm and a minimum of 4.5 μm . No mesh convergence was attempted so the chosen mesh parameters may still influence the obtained results. The laminar flow physics model was used with no slip conditions at the walls under a static simulation. Inlet conditions were defined as a laminar average flow rate of 0.004 m/s (200 $\mu\text{L}/\text{hr}$ through a duct 70 μm by 200 μm) and outlet was defined as at zero pressure. The main channel was given a length of 250 μm . The simulation output gave the velocity component in the three dimensions, Reynolds number, pressure and vorticity.

Note the change of axis for the Comsol simulation, as shown in figure AB.1, compared to models in the main text.

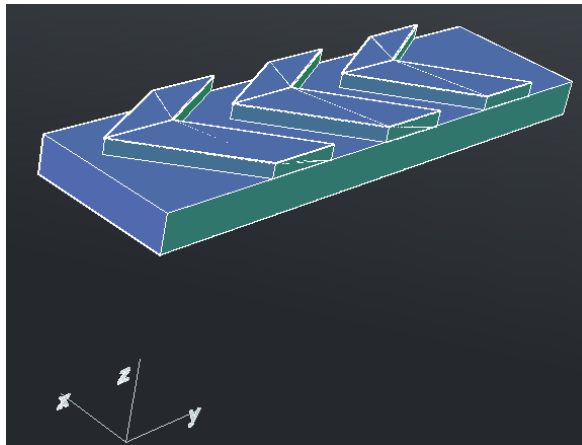


Figure AB.1: Axis system for Comsol simulation.

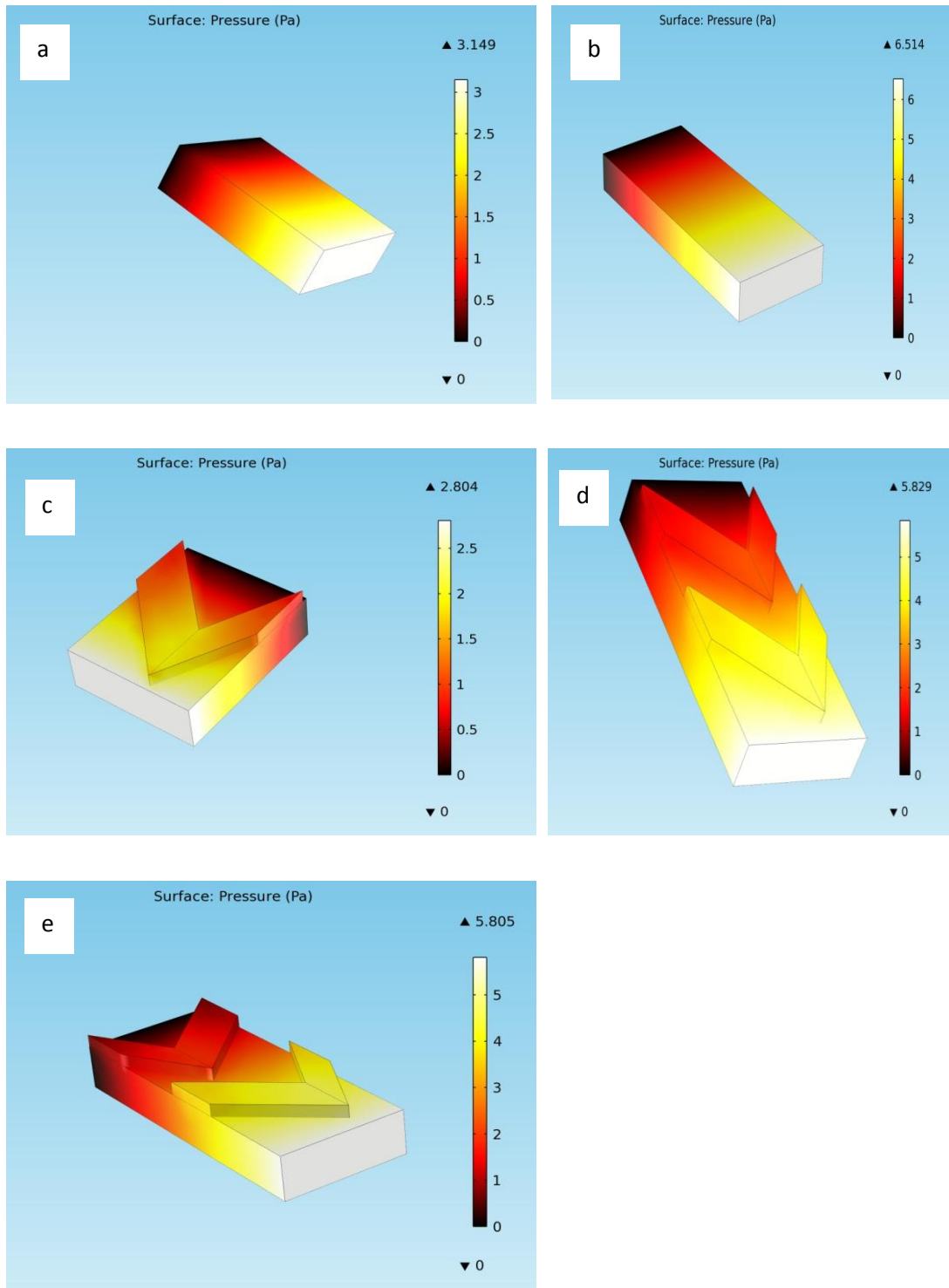


Figure AB.2: Pressure data from Comsol simulations showing (a) a short channel; (b) a longer channel; (c) a single SHM; (d) a double SHM and (e) an SHM junction. Light

colouring shows high pressure at the inlet while dark colours show low pressures at the outlet. Values on the right of the figures show maximum and minimum values.

Figure AB.2 shows the pressure output graphic from the simulation in Comsol 4.0. The fluid enters the volume element at the lightest colour on the thermal map under the highest pressure. The model then accounts for pressure drop along the channel length before leaving the element at the darkest point (zero pressure as defined in the simulation inputs). Since the pressure at the outlet is defined as zero in this element, it is possible to obtain directly the pressure drop across the simulation space from the peak pressure shown above the thermal gradient on the right of the models. The single and double channel (figure AB.2 a and b respectively) were used so that a direct comparison could be made between a rectangular duct and the same duct with various orientations of SHM. Comparing the short channel and the single SHM and the longer channel with the double SHM and junction SHM shows that the inclusion of SHM reduces the pressure drop to 90% of that for a duct. This is because the rotational advection flow is still within the laminar flow regime and does not cause any significant additional pressure drop along the channel length. The only relevant factor in the difference between the duct with and without the SHM appears to be the increase in the effective diameter by having the recessed SHM in the channel which acts to decrease the pressure drop (as stated in the main text, resistance and hence pressure drop is well described by a function of h^{-3}). Further work should account for this altered resistance in mixing channels to improve the devices designed using the electrical circuit analogy. It would also be useful to re-express the effective diameter in the SHM in the hydraulic resistance equation directly rather than by determination through experiment.

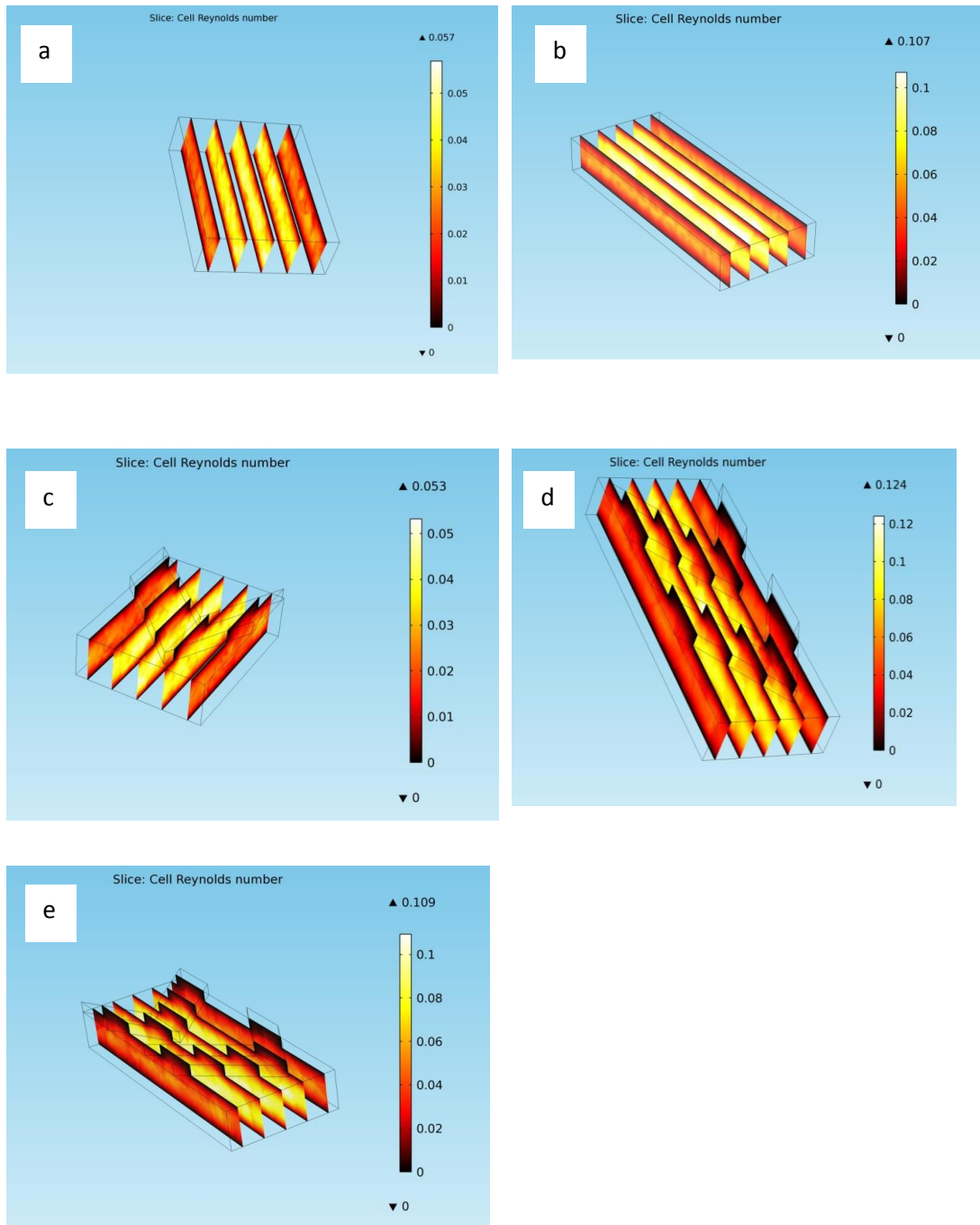
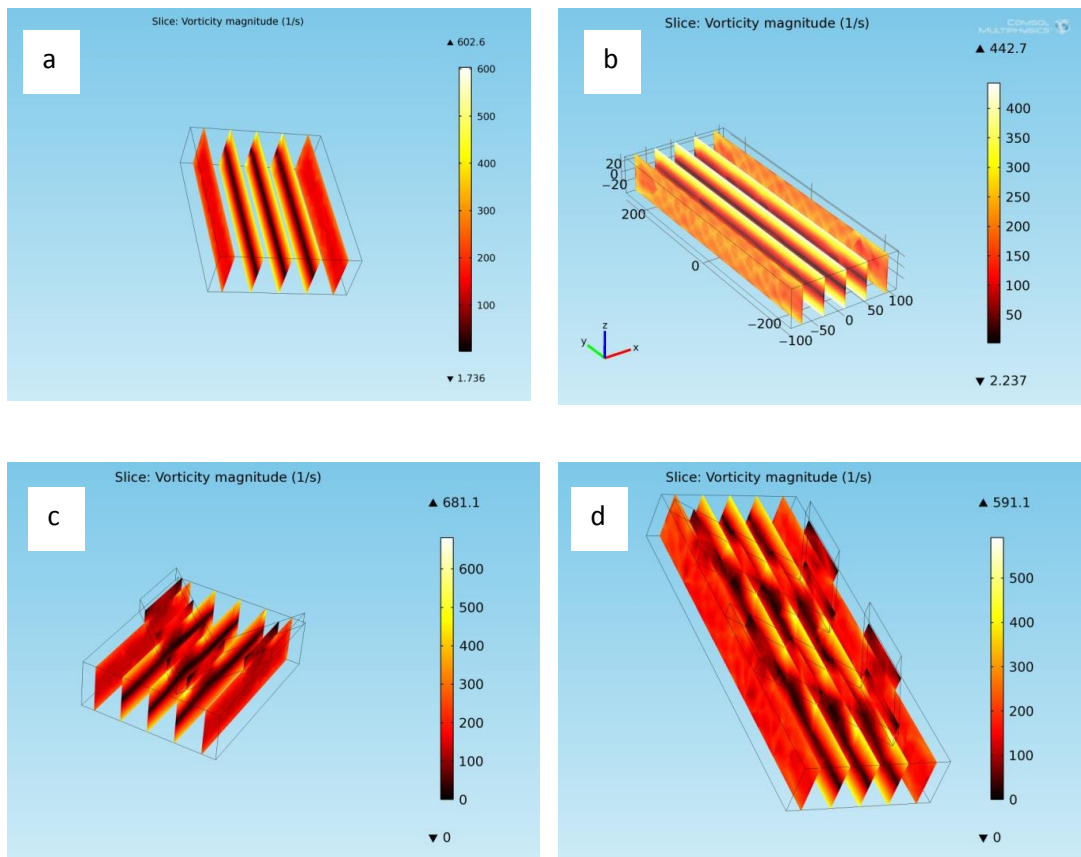


Figure AB.3: Reynolds number from Comsol simulations showing (a) a short channel; (b) a longer channel; (c) a single SHM; (d) a double SHM and (e) an SHM junction. Light colouring shows high Re at the centre of the channels. while dark colours show

low Re at the walls, where the no-slip condition applies. Values on the right of the figures show maximum and minimum values.

Figure AB.3 shows the Reynolds number from the Comsol 4.0 simulation. In this case the absolute values are relatively uninformative given the unconstrained and unequal nature of the meshing between the different types of simulation. It can be seen however that all elements with the simulation are well within the laminar, viscous flow region with peak Reynolds number for any simulation being 0.124. The flow pattern shown is consistent with laminar flow in a duct with peak Reynolds number being in the centre of the channel where velocity is highest. Elements where the SHM joins the main channel do not show any turbulence confirming that the mixing is by advective flow only, not by localised turbulence caused by the mixing design.



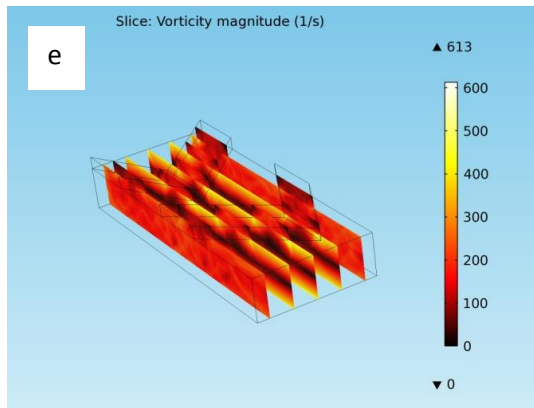


Figure AB.4: Vorticity data from Comsol simulations showing (a) a short channel; (b) a longer channel; (c) a single SHM; (d) a double SHM and (e) an SHM junction. Light colouring shows high vorticity at the walls where the shear between laminae is greatest. Dark colours show low vorticity at the centre of the channels, where shear is lowest. Values on the right of the figures show maximum and minimum values.

Figure b is erroneously processed.

Figure AB.4 shows the vorticity (a continuum field describing the local spinning motion) from the Comsol 4.0 simulation. Excluding model b, the remaining simulations all show similar peak vorticity (this appears to be due to a data processing error in the representation of the data). A higher vorticity shows that a vortex instability is more likely to form. In these simulations the peak vorticity was always observed at the channel wall where the no slip condition was applied. It is unlikely therefore that the vortex formation will be significant given this result. Previous Comsol studies had shown some vortex formation at the corners inside the SHM at Reynolds numbers similar to that seen here but a normalisation technique was employed which was not elaborated on in the work [98]. Vorticity can be checked through experiment if required but it can be assumed that vortex formation will not be significant

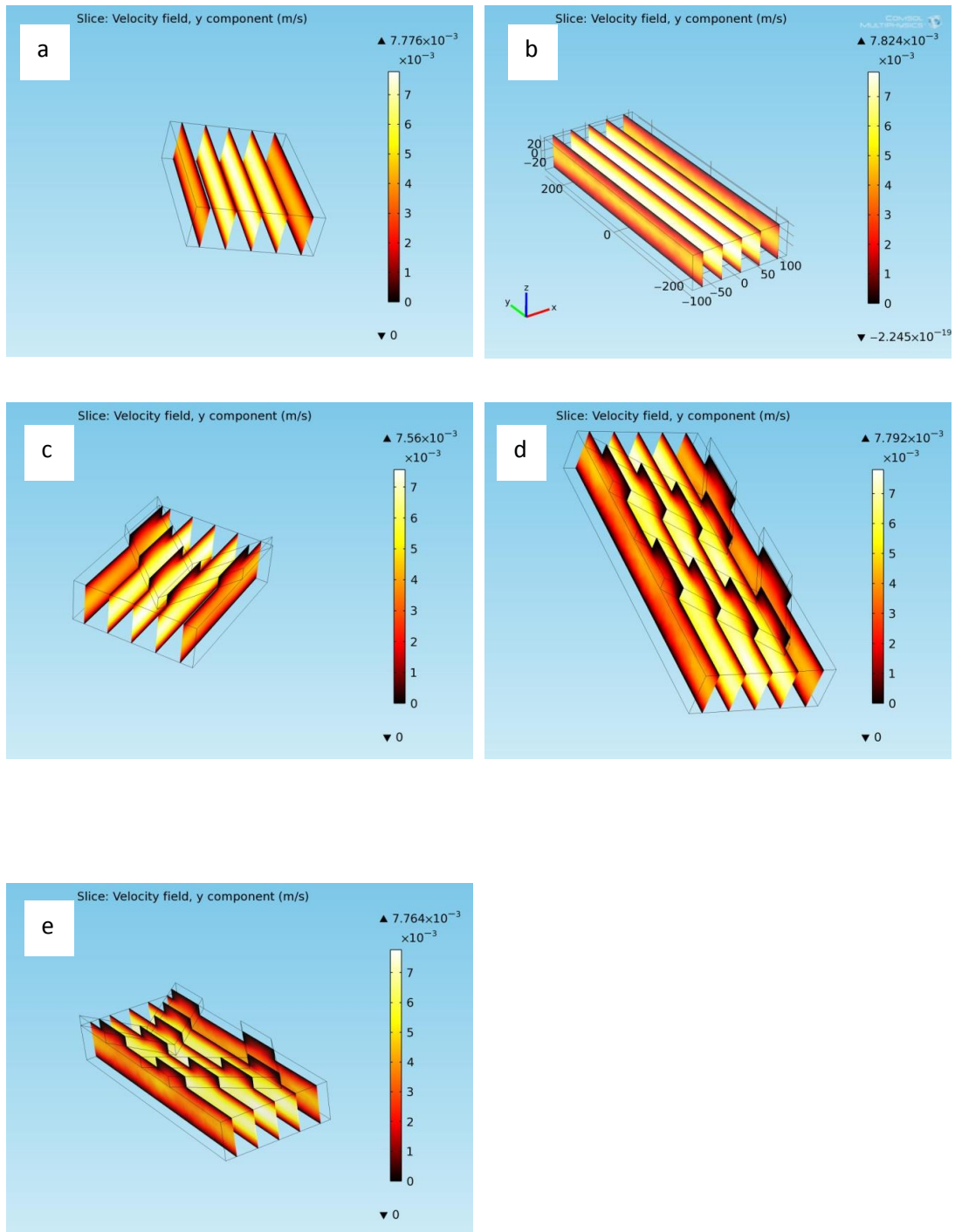
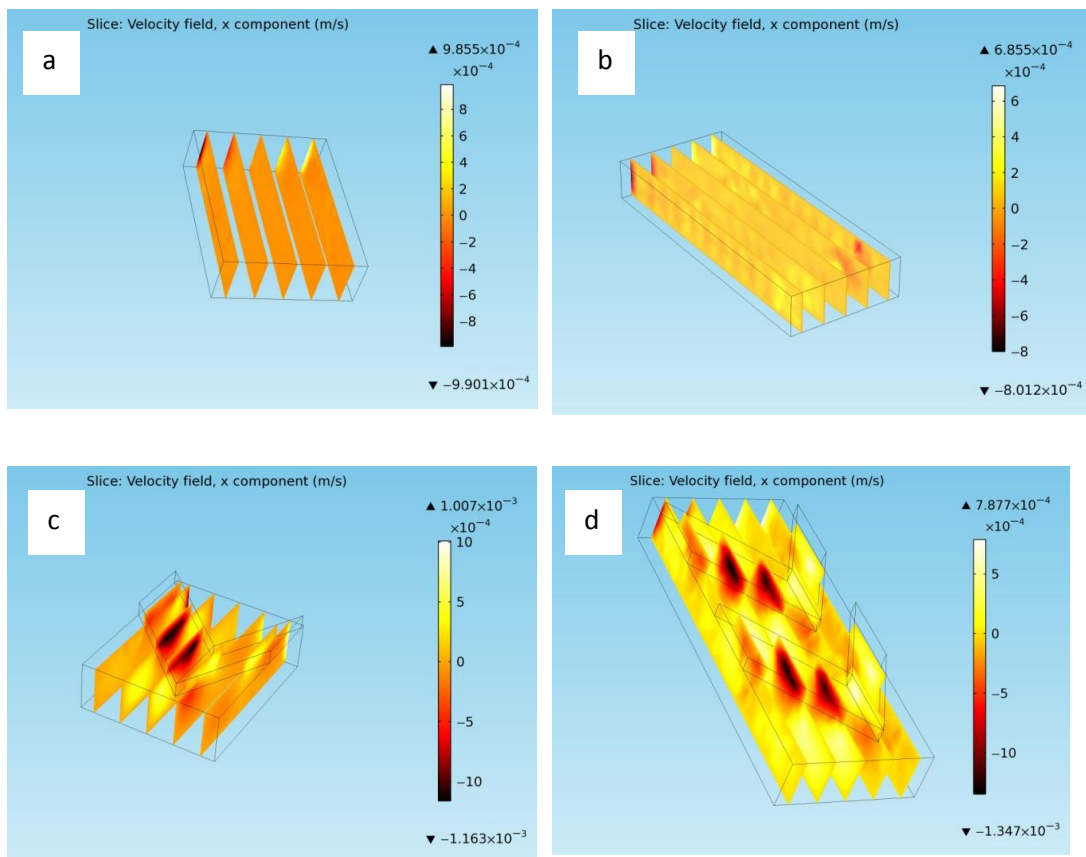


Figure AB.5: y axis velocity magnitude data from Comsol simulations showing (a) a short channel; (b) a longer channel; (c) a single SHM; (d) a double SHM and (e) an SHM junction. Light colouring shows high velocity at the centre of the channels where laminar profile velocity is highest. Dark colours show low velocity at the walls,

where the no-slip condition applies. Values on the right of the figures show maximum and minimum values.

The velocity magnitude in the y-axis is shown in figure A B.5. The y-axis is the axis down which fluid flows and is the major component of the velocity magnitude. All simulations have a similar peak velocity at close to that predicted for laminar flow profiles with an average velocity of 0.004 m/s. For all of the SHM simulations there is significant flow within the mixing pattern, showing that they are involved in the flow. The internal corners of the SHM have very low velocity suggesting they contain points of low or no flow.



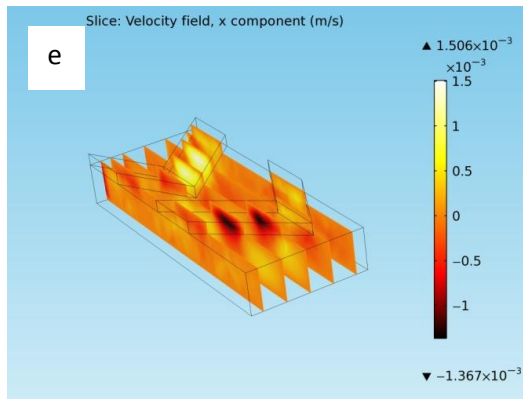


Figure AB.6: x axis velocity magnitude data from Comsol simulations showing (a) a short channel; (b) a longer channel; (c) a single SHM; (d) a double SHM and (e) a SHM junction. Light colouring shows high velocity to the right. Dark colours show high velocity to the left. Values on the right of the figures show maximum and minimum values. Note the larger magnitude of the values within the SHM and the anomaly at the end of the straight channel.

The flow in the x axis (figure AB.6) shows the flow magnitude across the width of the channel. For the two ducts there is little flow across the channel with some artefacts from the simulation at the end of the channels. With the SHM there is significant flow across the channel. In simulation d, the double SHM, the flow velocity in the second herringbone is higher than in the first as the helical flow is established. In the junction between the two SHM the flow velocity maximum readily transfers to the second SHM major side; flow velocity in the shorter side after the junction does not maintain the high velocity maintained by the first SHM.

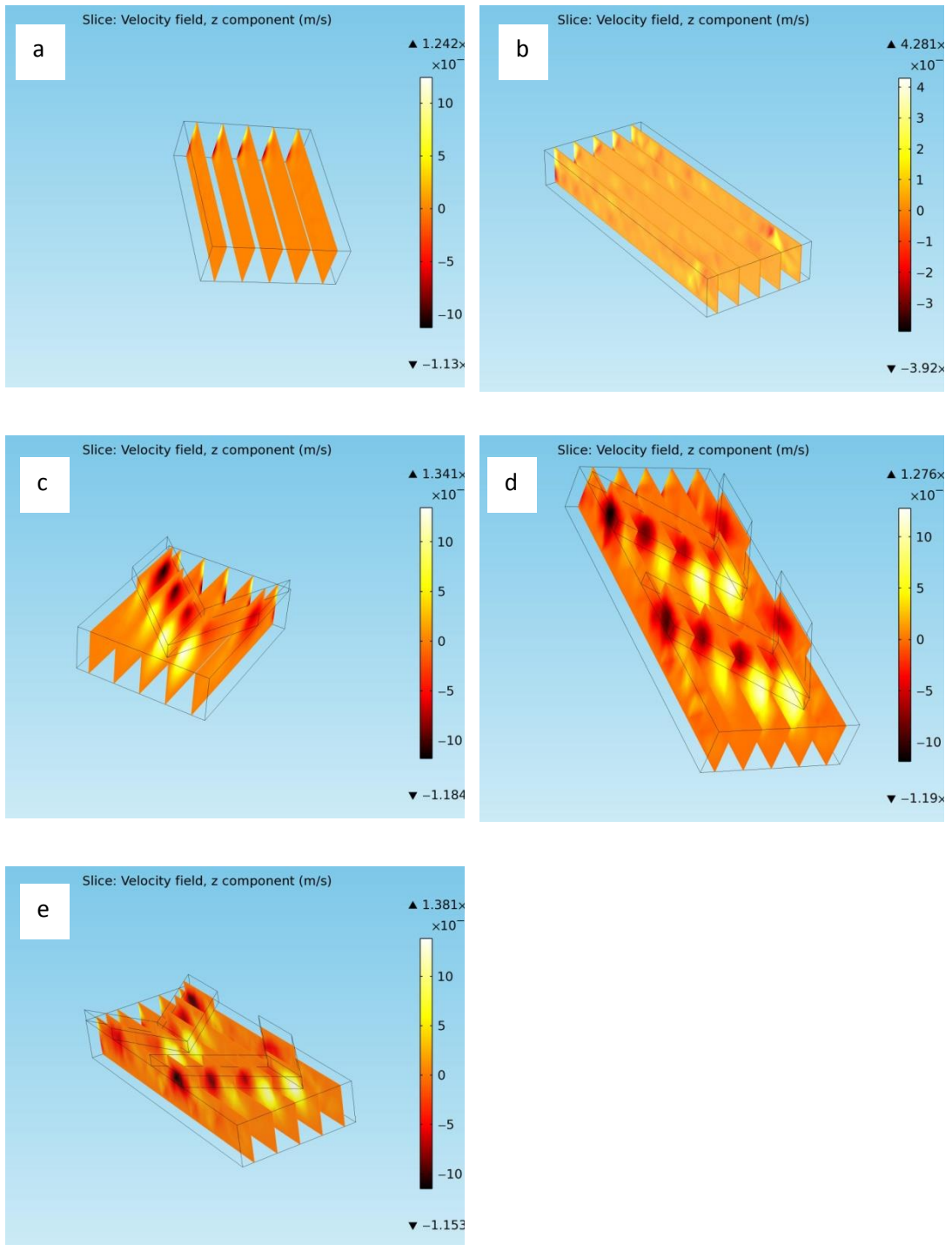


Figure AB.7: z axis velocity magnitude data from Comsol simulations showing (a) a short channel; (b) a longer channel; (c) a single SHM; (d) a double SHM and (e) an SHM junction. Light colouring shows high velocity upwards. Dark colours show high

velocity downwards. Values on the right of the figures show maximum and minimum values. Note the larger magnitude of the values into and out of the SHM.

Figure AB.7 shows the z-axis velocity and has many similarities to x velocity magnitude; in the ducts of both lengths there is very little flow across, up and down the channel except from the artefacts at the end of the simulation space. Flows through all of the SHMs are similar with peak up flow into the mixing pattern at the point of the SHM. Down flow occurs along the width of the SHM, primarily at the back edge of the mixer and where it meets the side wall. Down flow in the minor side is much less significant than in the longer side.

The main results of the Comsol simulations are that the pressure drop decreased in channels with the SHM. This is because the laminar nature of the flow remains consistent and sequences where the channel is expanded to 90 μm high instead of 70 μm explain the decreased pressure drop. A more extensive Comsol simulation could be run to confirm but this is computationally time consuming; the results will be assumed to hold for a more extensive section of SHMs and that the pressure drop is 90% that for a straight channel.

With the SHM there was significant flow across the main channel flow, indicating chaotic mixing should occur. No such flow was observed in a simple rectangular channel of the same length. Reynolds numbers never exceeded 1 for any mesh element indicating highly laminar flow was maintained in all cases. Vorticity remained relatively constant for all simulations; this suggests that the sharp angles where the individual SHM elements end and re-join the main channel are not likely to result in closed vortex formation where fluid elements circle with the recessed SHM, reducing mixing effectiveness.

1.10 Appendix C: Mixing in the SHM

The fluorescence images in the main text indicate that the SHM homogenises liquid on each side of the herring bone separately. This leads to a simple model of this mixing that can be constructed based on a simple mathematical description.

Each side of the SHM was termed major or minor as per figure AC.1. It was assumed that for two mixing streams the concentration had an initial value of either 1 or 0 for the component in the inlet stream. It was assumed that each half cycle of the SHM completely homogenised the liquid across that vortex of the mixer. For the full cycle in figure AC.2 this means that each of the four coloured blocks was considered separate and, by the end of the half cycle, completely mixed.

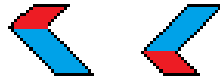


Figure AC.1: Diagram showing the major (blue) and minor (red) sides of the SHM.



Figure AC.2: Diagram showing homogenised blocks for one full cycle of the SHM.

In this model, the mixing is characterised by the ratio of concentrations in the two sides of the SHM. For completely unmixed streams the ratio will be zero and for complete mixing the ratio will be one. For a mixture of equal volumes, the flow entering on the minor side of the SHM is dispersed slightly more quickly at the beginning of the first half cycle as shown in figure AC.3. Both components approach complete mixing after the third full cycle of the SHM. Since both streams are of equivalent volume it is unimportant which stream is assigned to which side of the

mixer; whichever stream enters on the major side is dispersed slightly slower at the beginning of the cycles but this is unavoidable.

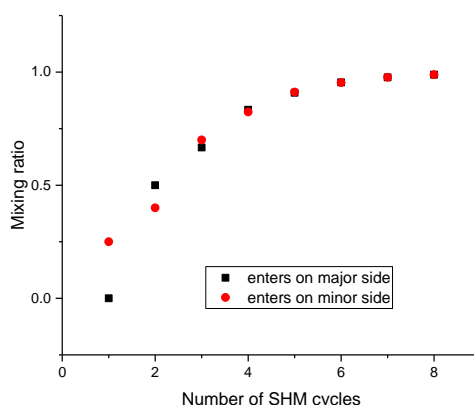


Figure AC.3: Graph of mixing ratio with two equal streams in the SHM.

The description becomes more complex when the two streams are no longer of equivalent volume. A mixing ratio of 6:1 is shown in this example as it is the same as the mixing between the colloid stream and functionalisation stream in the actual device.

For the smaller volume stream it is unimportant which side of the SHM it enters on as both the major and minor side disperse the fluid at the same rate as shown by the pink and blue triangles in figure AC.4. This happens because the fraction of the stream is so small it will not fill either side of the SHM by itself. It will therefore be mixed with the other stream from the very first half cycle, regardless of which side of the SHM it enters on.

For the major stream the mixing is now no longer equivalent as shown by the black and red squares in figure AC.3. This is because the stream takes up a large part of the channel width, so it is important to have the best mixing possible with the smaller stream. This happens when it enters on the minor side as it exceeds the smaller side of the SHM and occupies most of the larger side to achieve a greater extent of mixing with the smaller stream after the first half cycle. This gives the most rapid dispersion

of the larger stream and the major stream entering the SHM on the minor side should therefore be the arrangement used.

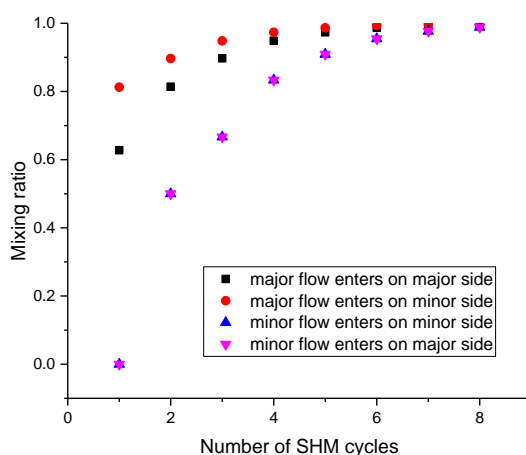


Figure AC.4: Graph of mixing ratios for a 6:1 stream mix in the SHM.

1.11 References

1. Sackmann, E.K., A.L. Fulton, and D.J. Beebe, *The present and future role of microfluidics in biomedical research*. *Nature*, 2014. **507**(7491): p. 181-189.
2. Kurita, R., et al., *On-Chip Enzyme Immunoassay of a Cardiac Marker Using a Microfluidic Device Combined with a Portable Surface Plasmon Resonance System*. *Analytical Chemistry*, 2006. **78**(15): p. 5525-5531.
3. Moorthy, J., et al., *Microfluidic tectonics platform: A colorimetric, disposable botulinum toxin enzyme-linked immunosorbent assay system*. *Electrophoresis*, 2004. **25**(10-11): p. 1705-1713.
4. Martinez, A.W., et al., *Diagnostics for the Developing World: Microfluidic Paper-Based Analytical Devices*. *Analytical Chemistry*, 2010. **82**(1): p. 3-10.
5. Noh, H. and S.T. Phillips, *Fluidic Timers for Time-Dependent, Point-of-Care Assays on Paper*. *Analytical Chemistry*, 2010. **82**(19): p. 8071-8078.
6. Ge, L., et al., *3D Origami-based multifunction-integrated immunodevice: low-cost and multiplexed sandwich chemiluminescence immunoassay on*

- microfluidic paper-based analytical device*. Lab on a Chip, 2012. **12**(17): p. 3150-3158.
7. Whitesides, G.M., *The origins and the future of microfluidics*. Nature, 2006. **442**(7101): p. 368-373.
 8. Cho, S., et al., *Droplet-based microfluidic platform for high-throughput, multi-parameter screening of photosensitizer activity*. Analytical chemistry, 2013. **85**(18): p. 8866-8872.
 9. Shamsi, M.H., et al., *Electrochemiluminescence on digital microfluidics for microRNA analysis*. Biosensors and Bioelectronics, 2016. **77**: p. 845-852.
 10. Elvira, K.S., R. Leatherbarrow, and J. Edel, *Droplet dispensing in digital microfluidic devices: Assessment of long-term reproducibility*. Biomicrofluidics, 2012. **6**(2): p. 022003.
 11. Ng, A.H.C., et al., *Digital Microfluidic Platform for the Detection of Rubella Infection and Immunity: A Proof of Concept*. Clinical Chemistry, 2014.
 12. Coulson, J.M., et al., *Fluid Flow, Heat Transfer and Mass Transfer*. Coulson and Richardson's Chemical Engineering. Vol. one. 1999, Oxford: Butterworth-Heinemann.
 13. Kenis, P.J.A., R.F. Ismagilov, and G.M. Whitesides, *Microfabrication Inside Capillaries Using Multiphase Laminar Flow Patterning*. Science, 1999. **285**(5424): p. 83-85.
 14. Rodriguez-Trujillo, R., et al., *Label-free protein detection using a microfluidic Coulter-counter device*. Sensors and Actuators B: Chemical, 2014. **190**: p. 922-927.
 15. Andreou, C., et al., *Rapid Detection of Drugs of Abuse in Saliva Using Surface Enhanced Raman Spectroscopy and Microfluidics*. ACS Nano, 2013. **7**(8): p. 7157-7164.
 16. Hessel, V., H. Löwe, and F. Schönfeld, *Micromixers—a review on passive and active mixing principles*. Chemical Engineering Science, 2005. **60**(8–9): p. 2479-2501.

17. Dreher, S., et al., *Theoretical and Experimental Investigations of Convective Micromixers and Microreactors for Chemical Reactions*, H. Bockhorn, et al., Editors. 2010, Springer Berlin Heidelberg. p. 325-346.
18. SadAbadi, H., M. Packirisamy, and R. Wuthrich, *High performance cascaded PDMS micromixer based on split-and-recombination flows for lab-on-a-chip applications*. RSC Advances, 2013. **3**(20): p. 7296-7305.
19. Zhou, B., et al., *Design and fabrication of magnetically functionalized flexible micropillar arrays for rapid and controllable microfluidic mixing*. Lab on a Chip, 2015. **15**(9): p. 2125-2132.
20. Keir, R., et al., *SERFS. In Situ Substrate Formation and Improved Detection Using Microfluidics*. Analytical Chemistry, 2002. **74**(7): p. 1503-1508.
21. Mengeaud, V., J. Josserand, and H.H. Girault, *Mixing Processes in a Zigzag Microchannel: Finite Element Simulations and Optical Study*. Analytical Chemistry, 2002. **74**(16): p. 4279-4286.
22. Guo, B., T.A.G. Langrish, and D.F. Fletcher, *CFD simulation of precession in sudden pipe expansion flows with low inlet swirl*. Applied Mathematical Modelling, 2002. **26**(1): p. 1-15.
23. Liu, R.H., et al., *Passive mixing in a three-dimensional serpentine microchannel*. Journal of Microelectromechanical Systems, 2000. **9**(2): p. 190-197.
24. Chen, L., et al., *Evaluation of passive mixing behaviors in a pillar obstruction poly(dimethylsiloxane) microfluidic mixer using fluorescence microscopy*. Microfluidics and Nanofluidics, 2009. **7**(2): p. 267-273.
25. Liu, Y.Z., B.J. Kim, and H.J. Sung, *Two-fluid mixing in a microchannel*. International Journal of Heat and Fluid Flow, 2004. **25**(6): p. 986-995.
26. Mark, A.E., A.J. Michael, and K.G. Bruce, *Determining the optimal PDMS–PDMS bonding technique for microfluidic devices*. Journal of Micromechanics and Microengineering, 2008. **18**(6): p. 067001.
27. Lee, C.-Y., et al., *Microfluidic Mixing: A Review*. International Journal of Molecular Sciences, 2011. **12**(5): p. 3263-3287.

28. Knight, J.B., et al., *Hydrodynamic Focusing on a Silicon Chip: Mixing Nanoliters in Microseconds*. Physical Review Letters, 1998. **80**(17): p. 3863-3866.
29. Hertzog, D.E., et al., *Femtomole Mixer for Microsecond Kinetic Studies of Protein Folding*. Analytical Chemistry, 2004. **76**(24): p. 7169-7178.
30. Majedi, F.S., et al., *Microfluidic synthesis of chitosan-based nanoparticles for fuel cell applications*. Chemical Communications, 2012. **48**(62): p. 7744-7746.
31. Stroock, A.D., et al., *Chaotic Mixer for Microchannels*. Science, 2002. **295**(5555): p. 647-651.
32. Kee, S.P. and A. Gavriilidis, *Design and characterisation of the staggered herringbone mixer*. Chemical Engineering Journal, 2008. **142**(1): p. 109-121.
33. Stroock, A.D. and G.J. McGraw, *Investigation of the staggered herringbone mixer with a simple analytical model*. Philosophical Transactions of the Royal Society of London A: Mathematical, Physical and Engineering Sciences, 2004. **362**(1818): p. 971-986.
34. Lin, X.Z., A.D. Terepka, and H. Yang, *Synthesis of Silver Nanoparticles in a Continuous Flow Tubular Microreactor*. Nano Letters, 2004. **4**(11): p. 2227-2232.
35. Manca, J.V., et al., *Localized monitoring of electromigration with early resistance change measurements*. Microelectronics Reliability, 1998. **38**(4): p. 641-650.
36. Choi, N., et al., *Simultaneous detection of duplex DNA oligonucleotides using a SERS-based micro-network gradient chip*. Lab on a Chip, 2012. **12**(24): p. 5160-5167.
37. Lee, K., et al., *Microfluidic concentration-on-demand combinatorial dilutions*. Microfluidics and Nanofluidics, 2011. **11**(1): p. 75-86.
38. Lee, M., et al., *SERS-based immunoassay using a gold array-embedded gradient microfluidic chip*. Lab on a Chip, 2012. **12**(19): p. 3720-3727.
39. Gao, Y., et al., *A compact microfluidic gradient generator using passive pumping*. Microfluidics and Nanofluidics, 2012. **12**(6): p. 887-895.

40. Nguyen, N.-T., et al., *Design, fabrication and characterization of drug delivery systems based on lab-on-a-chip technology*. *Advanced Drug Delivery Reviews*, 2013. **65**(11–12): p. 1403-1419.
41. Khan, F., et al., *Lectins as markers for blood grouping*. *Medical Science Monitor*, 2002. **8**(12): p. RA293-RA300.
42. Lindhorst, T.K., *Essentials of carbohydrate chemistry and biochemistry*. 2000: Wiley-VCH Weinheim, Germany.
43. Sharon, N. and H. Lis, *History of lectins: from hemagglutinins to biological recognition molecules*. *Glycobiology*, 2004. **14**(11): p. 53R-62R.
44. Holmgren, J., et al., *Interaction of cholera toxin and membrane GM1 ganglioside of small intestine*. *Proceedings of the National Academy of Sciences of the United States of America*, 1975. **72**(7): p. 2520-2524.
45. Karel, L., *The inhibition and potentiation of cellular agglutination by ricin, with a note on the toxicity of special preparations of ricin in mice*. *Journal of Cellular and Comparative Physiology*, 1946. **28**(3): p. 339-347.
46. Leung, H.S.Y., et al., *Entry of Influenza A Virus with a α 2,6-Linked Sialic Acid Binding Preference Requires Host Fibronectin*. *Journal of Virology*, 2012. **86**(19): p. 10704-10713.
47. Cummins, B., et al. *ConA-based glucose sensing using the long-lifetime azadioxatriangulenium fluorophore*. 2014.
48. Waterhouse, D.J., et al. *Design and validation of a near-infrared fluorescence endoscope for detection of early esophageal malignancy using a targeted imaging probe*. 2016.
49. Wang, X., O. Ramström, and M. Yan, *Quantitative Analysis of Multivalent Ligand Presentation on Gold Glyconanoparticles and the Impact on Lectin Binding*. *Analytical Chemistry*, 2010. **82**(21): p. 9082-9089.
50. Watanabe, S., et al., *Thioglucose-stabilized gold nanoparticles as a novel platform for colorimetric bioassay based on nanoparticle aggregation*. *Colloids and Surfaces B: Biointerfaces*, 2010. **81**(2): p. 570-577.

51. Jayawardena, H.S.N., X. Wang, and M. Yan, *Classification of Lectins by Pattern Recognition Using Glyconanoparticles*. Analytical Chemistry, 2013. **85**(21): p. 10277-10281.
52. Edelman, G.M., et al., *The Covalent and Three-Dimensional Structure of Concanavalin A*. Proceedings of the National Academy of Sciences of the United States of America, 1972. **69**(9): p. 2580-2584.
53. Ahmed, H.U., et al., *The determination of protonation states in proteins*. Acta Crystallographica Section D: Biological Crystallography, 2007. **63**(8): p. 906-922.
54. Fotinou, C., et al., *The crystal structure of tetanus toxin Hc fragment complexed with a synthetic GT1b analogue suggests cross-linking between ganglioside receptors and the toxin*. Journal of Biological Chemistry, 2001. **276**(34): p. 32274-32281.
55. Goldstein, I.J. and R.D. Poretz, *Isolation, Physicochemical Characterization and Carbohydrate-Binding Specificity of Lectins*, in *The Lectins: Properties, Functions, and Applications in Biology and Medicine*, I. Liener, N. Sharon, and I.J. Goldstein, Editors. 1986, Academic Press Inc.: London.
56. Goto, S., et al., *Quantitative estimation of interaction between carbohydrates and concanavalin A by surface plasmon resonance biosensor*. Chemical and pharmaceutical bulletin, 2002. **50**(4): p. 445-449.
57. Shang, Y., Y. Zeng, and Y. Zeng, *Integrated Microfluidic Lectin Barcode Platform for High-Performance Focused Glycomic Profiling*. Scientific Reports, 2016. **6**: p. 20297.
58. Jolly, P., et al., *DNA aptamer-based sandwich microfluidic assays for dual quantification and multi-glycan profiling of cancer biomarkers*. Biosensors and Bioelectronics, 2016. **79**: p. 313-319.
59. Heyries, K.A., et al., *Microfluidic biochip for chemiluminescent detection of allergen-specific antibodies*. Biosensors and Bioelectronics, 2008. **23**(12): p. 1812-1818.

60. Craig, D., et al., *Formation of SERS active nanoparticle assemblies via specific carbohydrate-protein interactions*. Chemical Communications, 2013. **49**(1): p. 30-32.
61. Hone, D.C., A.H. Haines, and D.A. Russell, *Rapid, Quantitative Colorimetric Detection of a Lectin Using Mannose-Stabilized Gold Nanoparticles*. Langmuir, 2003. **19**(17): p. 7141-7144.
62. Jain, P.K. and M.A. El-Sayed, *Plasmonic coupling in noble metal nanostructures*. Chemical Physics Letters, 2010. **487**(4-6): p. 153-164.
63. Cobley, C.M., et al., *Gold nanostructures: a class of multifunctional materials for biomedical applications*. Chemical Society Reviews, 2011. **40**(1): p. 44-56.
64. Jain, P.K., et al., *Calculated Absorption and Scattering Properties of Gold Nanoparticles of Different Size, Shape, and Composition: Applications in Biological Imaging and Biomedicine*. The Journal of Physical Chemistry B, 2006. **110**(14): p. 7238-7248.
65. Yang, L., et al., *Calibration of Silver Plasmon Rulers in the 1-25 nm Separation Range: Experimental Indications of Distinct Plasmon Coupling Regimes*. The Journal of Physical Chemistry C, 2010. **114**(11): p. 4901-4908.
66. Reinhard, B.M., et al., *Calibration of Dynamic Molecular Rulers Based on Plasmon Coupling between Gold Nanoparticles*. Nano Letters, 2005. **5**(11): p. 2246-2252.
67. E. L Ru, P.E., *Principles of Surface Enhanced Raman Spectroscopy*. 2009, Elsevier: The Netherlands.
68. Lyandres, O., et al., *Real-Time Glucose Sensing by Surface-Enhanced Raman Spectroscopy in Bovine Plasma Facilitated by a Mixed Decanethiol/Mercaptohexanol Partition Layer*. Analytical Chemistry, 2005. **77**(19): p. 6134-6139.
69. Turkevich, J., P.C. Stevenson, and J. Hillier, *A study of the nucleation and growth processes in the synthesis of colloidal gold*. Discussions of the Faraday Society, 1951. **11**: p. 55-75.

70. Leopold, N. and B. Lendl, *A New Method for Fast Preparation of Highly Surface-Enhanced Raman Scattering (SERS) Active Silver Colloids at Room Temperature by Reduction of Silver Nitrate with Hydroxylamine Hydrochloride*. *The Journal of Physical Chemistry B*, 2003. **107**(24): p. 5723-5727.
71. James, T.H., *The Reduction of Silver Ions by Hydroxylamine*. *Journal of the American Chemical Society*, 1939. **61**(9): p. 2379-2383.
72. Nichols, M.L., *The reduction of silver salts with hydroxylamine*. *Journal of the American Chemical Society*, 1934. **56**.
73. Cañamares, M.V., et al., *Comparative Study of the Morphology, Aggregation, Adherence to Glass, and Surface-Enhanced Raman Scattering Activity of Silver Nanoparticles Prepared by Chemical Reduction of Ag⁺ Using Citrate and Hydroxylamine*. *Langmuir*, 2005. **21**(18): p. 8546-8553.
74. Qin, L., et al., *Designing, fabricating, and imaging Raman hot spots*. *Proceedings of the National Academy of Sciences*, 2006. **103**(36): p. 13300-13303.
75. Donnelly, T., et al., *Silver and magnetic nanoparticles for sensitive DNA detection by SERS*. *Chemical Communications*, 2014. **50**(85): p. 12907-12910.
76. Taylor, G.T., S.K. Sharma, and K. Mohanan, *Optimization of a flow injection sampling system for quantitative analysis of dilute aqueous solutions using combined resonance and surface-enhanced Raman spectroscopy (SERRS)*. *Applied Spectroscopy*, 1990. **44**(4): p. 635-640.
77. Piorek, B.D., et al., *Free-surface microfluidic control of surface-enhanced Raman spectroscopy for the optimized detection of airborne molecules*. *Proceedings of the National Academy of Sciences*, 2007. **104**(48): p. 18898-18901.
78. Knauer, M., et al., *A flow-through microarray cell for the online SERS detection of antibody-captured E. coli bacteria*. *Analytical and Bioanalytical Chemistry*, 2012. **402**(8): p. 2663-2667.

79. Guo, L. and D.-H. Kim, *LSPR biomolecular assay with high sensitivity induced by aptamer–antigen–antibody sandwich complex*. *Biosensors and Bioelectronics*, 2012. **31**(1): p. 567-570.
80. Zhang, W., Q. Li, and M. Qiu, *A plasmon ruler based on nanoscale photothermal effect*. *Optics Express*, 2013. **21**(1): p. 172-181.
81. Larmour, I.A., K. Faulds, and D. Graham, *SERS activity and stability of the most frequently used silver colloids*. *Journal of Raman Spectroscopy*, 2012. **43**(2).
82. Stewart, A., et al., *Controlling assembly of mixed thiol monolayers on silver nanoparticles to tune their surface properties*. *Acs Nano*, 2012. **6**(5): p. 3718-3726.
83. Cerruti, M., et al., *Poly (ethylene glycol) monolayer formation and stability on gold and silicon nitride substrates*. *Langmuir*, 2008. **24**(19): p. 10646-10653.
84. Simpson, J., et al., *Mixed-monolayer glyconanoparticles for the detection of cholera toxin by surface enhanced Raman spectroscopy*. *Nanoscale Horizons*, 2016. **1**(1): p. 60-63.
85. Love, J.C., et al., *Self-Assembled Monolayers of Thiolates on Metals as a Form of Nanotechnology*. *Chemical Reviews*, 2005. **105**(4): p. 1103-1170.
86. Yi, M. and H.H. Bau, *The kinematics of bend-induced mixing in micro-conduits*. *International Journal of Heat and Fluid Flow*, 2003. **24**(5): p. 645-656.
87. Beebe, D.J., G.A. Mensing, and G.M. Walker, *Physics and applications of microfluidics in biology*. *Annual Review of Biomedical Engineering*, 2002. **4**: p. 261-286.
88. Fine, R.A. and F.J. Millero, *Compressibility of water as a function of temperature and pressure*. *The Journal of Chemical Physics*, 1973. **59**(10): p. 5529-5536.
89. Tosun, I., D. Uner, and C. Ozgen, *Critical Reynolds number for Newtonian flow in rectangular ducts*. *Industrial & Engineering Chemistry Research*, 1988. **27**(10): p. 1955-1957.

90. McAnally, G., et al., *SERRS dyes. Part I. Synthesis of benzotriazole monoazo dyes as model analytes for surface enhanced resonance Raman scattering*. Analyst, 2002. **127**(6): p. 838-841.
91. Cai, D., et al., *Raman, mid-infrared, near-infrared and ultraviolet–visible spectroscopy of PDMS silicone rubber for characterization of polymer optical waveguide materials*. Journal of Molecular Structure, 2010. **976**(1–3): p. 274-281.
92. Wagner, J., et al., *Generation of metal nanoparticles in a microchannel reactor*. Chemical Engineering Journal, 2004. **101**(1–3): p. 251-260.
93. Wagner, J., T.R. Tshikhudo, and J.M. Köhler, *Microfluidic generation of metal nanoparticles by borohydride reduction*. Chemical Engineering Journal, 2008. **135, Supplement 1**: p. S104-S109.
94. Schofield, C.L., et al., *Silver and Gold Glyconanoparticles for Colorimetric Bioassays*. Langmuir, 2006. **22**(15): p. 6707-6711.
95. Song, Y., M. Luo, and L.L. Dai, *Understanding Nanoparticle Diffusion and Exploring Interfacial Nanorheology using Molecular Dynamics Simulations*. Langmuir, 2009. **26**(1): p. 5-9.
96. El-Hallag, I.S., et al., *Electrochemical Investigation of Cysteamine at Carbon Fibre Microdisk Electrode*. Journal of the Chilean Chemical Society, 2011. **56**: p. 837-841.
97. Albaladejo, S., M.I. Marqués, and J.J. Sáenz, *Light control of silver nanoparticle's diffusion*. Optics Express, 2011. **19**(12): p. 11471-11478.
98. Williams, M.S., K.J. Longmuir, and P. Yager, *A practical guide to the staggered herringbone mixer*. Lab Chip, 2008. **8**(7): p. 1121-9.

2 Continuous Gold Colloid Production

2.1 Abstract

Production of gold nanoparticles by solution phase reduction of gold salts has been used for many years. The optical properties of these gold nanoparticles make them very useful, particularly within the biomedical sciences where they are used as markers and therapeutic agents. They are still produced using methods very close to the original batch chemistry and remain a very high value product. For their widespread use outside academia in a variety of areas (such as diagnostics and healthcare), a scale-up in production would be required. In this chapter, a novel bench-top scale continuous reactor for the production of gold nanoparticles was developed. It was found that the continuous stirred tank reactor was generally unsuitable for this synthesis. A laminar tubular reactor was more successful but fouling of the reactor material was a significant obstacle to production of good quality colloid. In both cases, nanoparticles produced in a batch synthesis were of higher and more consistent quality. This suggested that further development work was needed to develop a more competitive continuous production method.

2.2 Introduction

Gold nanoparticles are widely used in materials and biomedical applications including cancer diagnosis[1], photothermal therapy [2], therapeutic delivery agents [3], electronics [4] and catalysis [5]. Many of the uses rely on the nanoscale of the materials and the localised surface plasmon inherent in the gold structures at this nanoscale. The chemistry and physical description of these effects are well covered in a number of comprehensive reviews [6, 7].

Gold nanoparticles are also recognized by the World Gold Council as a technological area of interest; highlighting their potential impact and use on an industrial scale. Some commercial applications of gold nanoparticles are being developed [8-10]. However, to truly become an economic route for either diagnostic assays or point of care testing, especially for low resource environments [11], gold nanoparticles should be available in relatively large volumes and at sufficiently low cost.

Production of colloid traditionally uses relatively large batches of hundreds of millilitres on a laboratory scale; commercial production generally only scales this up to batches of litres. The commercial method of making colloid has not developed into a continuous process and relies on the relative ease with which gold colloid can be made in reproducible batches. A continuous production method for gold colloid could provide many advantages, including elimination of batch-to-batch variation and reduction of overall variation (which is already low for commercial gold colloids). With a continuous production, there would be very little down time and therefore the reactor could be more productive. A continuous process would also be less labour intensive, requiring less cleaning and charging of vessels *etc.* and have less reactor volume requirements for a given production. In continuous production, concerted steps are more readily synchronised into a single process; for example, multiple stages for seed synthesis and growth, anisotropic particle generation or colloid functionalisation. This latter step is particularly relevant for gold nanoparticles given the requirement for functionalisation in the majority of cases, and with the versatility afforded by general gold- thiol chemistry for functionalisation [12].

There have been large steps towards redesigning manufacturing pathways in industries such as pharmaceutical production, to include continuous synthesis and processing. In this setting, comparatively modest production scales of single tons per year of finalised products are common. This highlights the identified advantages of continuous production for high quality products, even for products not typically requiring large-scale production.

2.2.1 Gold Nanoparticle Production Methods

Gold nanoparticles are most often generated by solution phase reduction of water soluble gold salts, although other methods of production exist. These include ultrasonication [13], laser ablation [14, 15] and ultraviolet irradiation [16]. In this chapter, work focuses on the most widely used methods, including reduction by trisodium citrate [17, 18], sodium borohydride [19, 20] and ascorbic acid [21], with a later focus on the chemistry used by BBI solutions for the commercial production of colloid. This follows on from the developing project collaboration with BBI Solutions and interest in the potential utility of the reactor types developed here with the proprietary method of colloid production used in the company.

Of the colloid production methods used, the citrate reduction is the most widely employed and studied. Despite this, research into a complete understanding of the mechanistic detail is still ongoing and continues to produce new insights into the process [22-24]. However, the work of Turkevich revealed much of the detail of the process [25]. It was elucidated that the citrate was oxidised to acetone dicarboxylic acid, resulting in an induction time for the reaction to begin. A complex between gold ions and the acetone dicarboxylate ions was formed, resulting in a small oligomer of gold ions, which is then reduced when the resulting gold nucleus is of sufficient size to be stable. These 1-2 nm nuclei then coalesce and grow to give larger particles. This is a result of both multiple small gold nuclei coalescing together and of reduction of gold ions onto the surface of these nuclei. The stability of the colloid is then afforded

by the strong binding of the citrate ion to the gold nanoparticle in a layer of strongly bound ions, known as the Stern layer.

Sodium borohydride is a much stronger reducing agent than trisodium citrate; hence reduction of gold can proceed rapidly at room temperature (compared with the required boiling for citrate reduction). As a stronger reducing agent, borohydride more rapidly reduces the gold to small nuclei and these then coalesce. The nanoparticle synthesis reaction is proposed to include no growth steps [23].

Ascorbic acid is a weak reducing agent, most often used to generate gold nanorods [19]. Under these circumstances it is too weak to reduce Au (III) even when many gold ions are in a complex with the polymer cetyltrimethylammonium bromide [26]. When gold seed particles are added, the new Au (0) surface in solution lowers the energy potential to be overcome for reduction. This allows the growth of existing nanoparticles but precludes the generation of new seeds. For this reason ascorbic acid is often used as a growth medium for nanoparticles [27] and nanorods [26]. Higher concentrations of ascorbic acid can however reduce gold ions, but over a longer time resulting in poorer quality colloid.

As a first approximation, the size and dispersity of the nanoparticles produced is a good indicator of quality. Beyond this there are several factors that may affect the quality of a colloid for a particular use. These relevant factors can include: the homogeneity of particle shapes, the apparent SERS activity of various types of nanoparticles [28] and the surface chemistry of the colloid for bio-excretion and toxicity [29]. The majority of current uses for gold nanoparticles employ their distinct optoelectronic properties as a detection methodology for assays including plasmon extinction colorimetric assay [30], lateral flow assay [31] or surface enhanced Raman spectroscopy [32]. Since the optical properties of gold nanoparticles are intricately linked with their size, this is often the main criterion used in judging nanoparticle quality. Large deviations of nanoparticle size in a colloid is often undesirable as it gives an inconsistent optical response and can be difficult to functionalise consistently.

2.2.2 Measuring Nanoparticle Size

The size of colloidal nanoparticles can be measured in a number of different ways. For most metal nanoparticles, the most straightforward of these is the extinction of light by the plasmon resonance. From the solutions of Mie theory, the size and extinction coefficient of spherical nanoparticles correlates to their size [33]. Employing this, it is possible to easily and non-invasively monitor the extinction and therefore determine the size. Potential problems arise from the fact that a real colloid will have a variety of nanoparticle sizes and since scattering is a large contributor to the extinction of nanoparticles larger than about 10 nm, the largest particles will dominate the extinction profile. Dispersion in the size is difficult to quantify in extinction spectroscopy. Often this is correlated to the full width at half maximum (fwhm) [34] which is easily measured. It is defined as the width of the plasmon peak at half of the peak extinction. The basis for this metric is the assumption that all particles are spherical; therefore, any deviation around the central peak will arise from the presence of different sized spheres. The lower the fwhm, the fewer spheres with radii different from the average. Extinction spectroscopy can often not distinguish between very small gold nanoparticles, as at smaller sizes the scattering contribution is very small. This means that the plasmon resonance absorption gives very similar spectra for particles below about 15 nm in diameter. As the spectra are very similar, it is difficult to draw any conclusions about the size or dispersity for small colloids using the extinction spectra. Representative spectra for BBI Solutions produced colloids from five to fifteen nanometres are shown in figure 2.1. True sizing was determined by transmission electron microscopy.

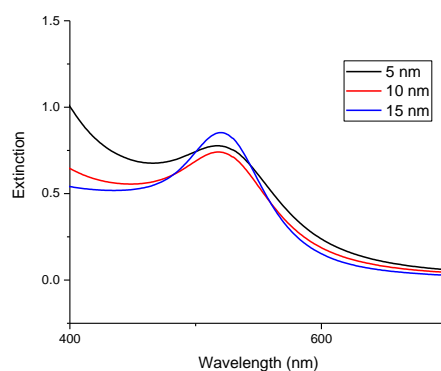


Figure 2.1: Extinction for small gold colloids of 5 nm (black), 10 nm (red) and 15 nm (blue). Observed differences in the extinction profile are very slight between the three samples. Data provided by BBI Solutions.

An alternative to extinction spectroscopy is dynamic light scattering (DLS). This technique uses the Brownian motion of nanoparticles in a colloid and the Stokes-Einstein equation to measure the hydrodynamic radius based on the scattering of laser light by a sample. The hydrodynamic radius includes ions strongly bound to the particle in the Stern layer (figure 2.2) and will therefore differ from the true size of the metallic nanoparticle core. Other issues can arise from heating of the sample by the laser through absorption or plasmonic heating. This heating creates a temperature gradient which causes more particle movement than would be predicted from Brownian motion and causes errors in calculations of the size. Again this technique relies on scattering and will therefore be prone to skewing of the results by the presence of larger nanoparticles (e.g. in a multimodal distribution or in a polydisperse sample). Size dispersion can be estimated from the produced histogram of nanoparticle size or related to the polydispersity index generated from the DLS calculations.

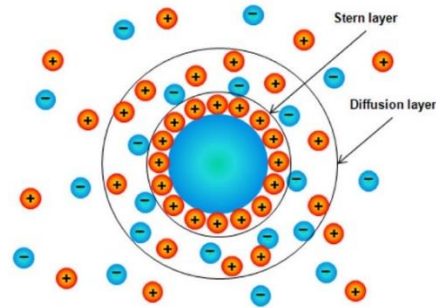


Figure 2.2: Diagram showing the Stern layer around a particle. In this example a negatively charged silica particle is surrounded by strongly bound positive ions in the Stern layer. A less strongly bound layer of ions surrounds this Stern layer. For gold nanoparticles, the Stern layer will be negatively charged. Reproduced from reference [35].

Both extinction spectroscopy and DLS sample a very large number of nanoparticles in producing a result. For unimodal, monodisperse samples these will be reliable and accessible methods for sizing colloidal nanoparticles. Alternative methods use electron microscopy to size a relatively small numbers of nanoparticles by visualizing them and measuring the image produced. These techniques require vacuum conditions and cannot sample the nanoparticles in their native suspended state. Scanning electron microscopy (SEM) is limited to sizing larger colloids and cannot reliably size particles below about 20 nm. Transmission electron microscopy (TEM), has higher resolution and can size smaller colloids. Both of these microscopy techniques are destructive and cannot be made continuous. In both, since a relatively small number of particles are sampled to produce the result, standard deviation is easily obtained from the data, either manually or through the program used to measure particles (such as ImageJ).

TEM is currently used to size colloidal gold nanoparticles produced commercially by BBI Solutions and a sample is sized for every batch produced, to ensure adherence to required standards. For a continuous process, it would be desirable if either extinction spectroscopy or DLS could be used to non-invasively, continuously monitor

the production of colloid, rather than employing expensive, off-line, labour intensive TEM or SEM techniques.

2.2.3 Continuous Gold Colloid Production in Literature

Previously some small reactors have been shown, mostly in the field of microfluidics. One relatively early work by Wagner *et al.* employed a small microreactor for the handling of gold nanoparticles [36]. When handling gold nanoparticles, the reactor was found to show very little fouling, even when incubated overnight. A seeded growth to form larger nanoparticles with ascorbic acid as the reducing agent was also reported in this work. Precipitation of gold in the glass and silicon microchannels was reported to be significant with this reduction at 10 $\mu\text{L}/\text{min}$. It was not reported whether this was also present at higher flowrates (flow rates up to 50 $\mu\text{L}/\text{min}$ were used). A further point of note in this work was the observation that with a low presence of seeds, nucleation rather than growth appeared to be promoted.

In a later expansion of this work, Wagner *et al.* used a similar microreactor to reduce gold salt with ascorbic acid, without any pre-formed seed [37]. Poly(vinylpyrrolidone) was used as a capping agent. In this work, the challenge of reactor fouling was directly addressed in three ways: producing only small colloid volumes (10 mL), not using the microreactor for long continuous synthesis and chemically modifying the internal walls of the reactor. Despite this, fouling remained a major issue with deposition of gold observed as either elemental gold or thin, violet-coloured films. Chemical modification of the channels was either by increasing the pH to 9.5, to deprotonate the surface silanol groups and therefore repel the negative nanoparticles, or by functionalisation with trichloro(1H,1H,2H,2H-perfluoro-octyl)silane to reduce wetting of the channel wall.

This microreactor was run at a much higher maximum flowrate of 8 mL/min, where the adsorption of gold to the reactor walls was at a minimum. At higher flow rates, a trend towards smaller particles was observed and attributed to a higher nucleation rate at higher flowrates. The coefficient of variance in almost all cases was around

30%; this standard deviation in the size is lower than that of some colloid made in traditional lab equipment.

A later work on continuous gold nanoparticle production was published by Shalom *et al.* on the use of a microfluidic mixer employing the Brust method to produce gold colloid [38]. The Brust method [20] uses a two phase liquid- liquid system where tetrachloroauric acid is moved from an aqueous phase to an organic phase by a phase transfer agent (tetrabutylammonium bromide). The organic soluble gold complex is then reduced by aqueous sodium borohydride in the presence of alkanethiols to give organic soluble gold nanoparticles. In the work of Shalom *et al.* the thiol/ gold salt complex in organic solvent with the phase transfer agent was prepared as a reagent and was reduced by aqueous sodium borohydride within the microfluidic mixer. The microfluidic mixer was made by wet etching glass with hydrofluoric acid. The mixer operated most effectively at less than 1 mL/ min and was shown to give both smaller particles and less standard deviation in the size than a corresponding bulk synthesis, up to a production of 800 μ L/ min. In keeping with the finding of Wagner, a trend towards smaller particles was observed at higher flowrates. The possibility of an integrated system where functionalised nanoparticles can be made and used all within a microfluidic chip was raised, indicating the planned trajectory of this small micromixer type reactor.

Work by Yang *et al.* moved gold nanoparticle synthesis away from the microreactor scale and instead used a small quartz coil as the reactor with peristaltic pumps to manipulate fluid flow [39]. The above examples by Wagner and Shalom used syringe pumps which are suitable for small scale but not truly continuous operation. Yang used ultraviolet light initiated reduction of tetrachloroauric acid by trisodium citrate, with poly(vinylpyrrolidone) as a capping agent and achieved a maximum flowrate of 6 mL/ min. Although lower than that used by Wagner, this reactor format is much more amenable to potential scale up and continuous operation. This work also noted the severe fouling of the quartz tubing used at lower flowrates and observed a decrease in this effect at higher flowrates, although elimination of the issue was not

achieved. Fouling was found to be most severe after an induction time for the reaction where the citrate had travelled a distance down the coil. Once again, higher flowrates led to increased nucleation and smaller gold nanoparticles. Particles were generally very small (2nm or less) and the coefficient of variance was 20-38%, the upper end of the scale being broadly in keeping with that from batch production.

The most successful of the previously shown reactors was a small bench-top continuous reactor developed by Lohse *et al*, which could produce either spherical gold nanoparticles or nanorods continuously [40]. A straightforward experimental set up was established with a binary mix of reagents flown through parallel streams in a peristaltic pump and mixed in a y-mixer, before flowing through a cell for spectrophotometry measurement, and then transferred to a storage flask. Nanoparticles could be made using a borohydride reduction with no seeding and nanorods made by a seeded growth method. Cetrimonium bromide (CTAB) was used as a capping agent in both cases. Sodium citrate and mercaptohexanoic acid were also shown as capping agents for spherical nanoparticles but production was most efficient using CTAB. Sodium borohydride is not well suited to continuous production as it decomposes in water (through the reaction of borohydride with water to give borates) but this synthesis was run for a number of hours, giving grams of nanorods produced, at a flow rate of 35- 60 mL/ min. No mention was made of problems with fouling over this long run time but the standard deviation is reported to be the same as batch synthesis, indicating that fouling does not present a significant obstacle to consistent particle production. This may be due to the high flow rate used in the device. The work of Lohse *et al*. represents the most significant advancement towards a continuous production of gold nanoparticles. Gram scale synthesis of nanorods was demonstrated, with the potential for in-line monitoring using a portable spectrophotometer also shown. This represents the most likely literature route for continuous scale-up and has been patented by the publishers [41].

Several papers exist covering other aspects of the continuous production of gold nanoparticles but the above cover the key developments from small microfluidics

with increasingly effective mixers and higher flow rates, to larger millifluidic reactors that are more likely to be amenable to scale up. Though the possibility exists for scale-out from small microfluidic devices, these are unlikely to be competitive with more usual reactor formats for production of large volumes, or even moderate volumes of colloid *e.g.* to provide nanoparticles in an academic research group.

Key points to summarise from the papers above are the impact of the flow on the gold nanoparticle synthesis; almost all the reports detail the reduction of particle size with increasing flow rate because of increased nucleation at high flow rates. Most works detailed above reference fouling of the reactor by the reduction of gold salts. It was observed most keenly at lower flow rates and was not eliminated in any of the works above. Thirdly in most cases where a coefficient of variance is given for the produced nanoparticles, this is close to that for the batch production and is lower in very few cases.

2.2.4 Reactor Configurations

A variety of reactor types exist and continue to be developed to address new design challenges and facilitate new chemistries. As a starting point three basic models can be expanded to generally describe most reactor formats: batch reactors, continuous stirred tank reactors and plug flow reactors. The key features of these reactors and their use on a bench-top scale are outlined below, along with a modification to the plug flow reactor – the laminar tubular reactor.

2.2.4.1 Batch Reactors

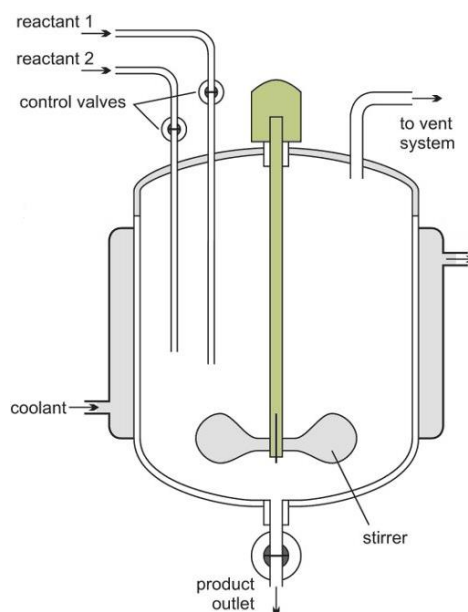


Figure 2.3: Diagram of a batch reactor showing temperature control jacket and stirrer. Note the lack of baffles to assist mixing and inlet temperature control in this diagram. Reproduced from reference [42].

The batch reactor is conceptually the simplest to understand and is the type currently used for gold nanoparticle production. A diagram showing the key features of a batch vessel is shown in figure 2.3. In this, a vessel of appropriate size acts as the reactor, all reagents are charged into the vessel and the reaction takes place. No material enters or leaves the vessel during the reaction except for gases produced which can be vented to prevent pressurising the vessel. Mixing is readily achieved by magnetic stirring or a suitable stirrer design (e.g. disk turbines, propeller mixers or anchor agitators) and baffles to prevent vortexing can be included [43]. Temperature control can be given by a heating mantle, heated oil bath or temperature controlled jacket.

Batch reactors have the advantage that they can be used for multiple reactions, with potentially no hardware modifications. This allows flexibility if small amounts of a variety of products are required (e.g. different sizes of colloid or nanoparticle shapes). Batch reactors can also be more easily scaled up, as long as efficient mixing and heat

transfer are maintained. However due to the required downtime and cleaning of batch vessels, they are less productive over a given time and require more operator input. Since product is prepared in distinct batches, slight changes in conditions at the reaction initiation can cause batch-to-batch variation. For these reasons a continuous reactor configuration is often preferred; it requires very little down time, less reactor volume for a given production rate, less operator input and has very little product variation at steady state.

2.2.4.2 Continuous Stirred Tank Reactor

The most obvious development from the batch reactor is a continuous stirred tank reactor (CSTR), in which a batch style tank is continuously charged with new reagents and product is drawn off, as shown in figure 2.4. The use of the same vessel as batch reactors simplifies required maintenance and cleaning. Agitators and heat transfer equipment can be similar to a batch reactor design.

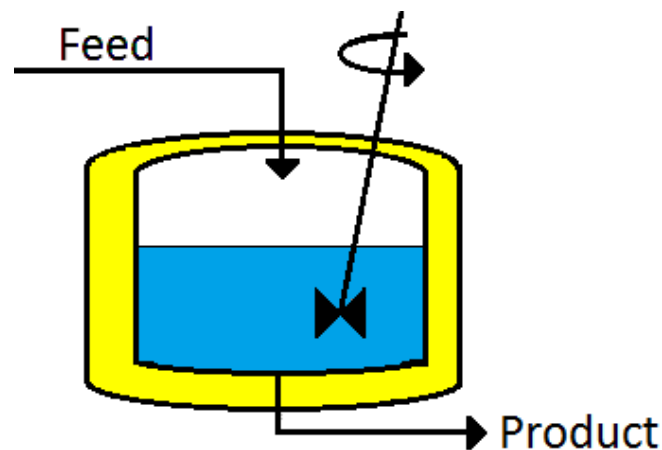


Figure 2.4: Diagram showing a block diagram of a CSTR with jacket (yellow) and stirrer. Other elements from batch reactors can be included, such as baffles and vents as required.

For a continuous reactor the concept of a residence time is introduced; for a batch reactor this is obvious- the time between initiating the reaction (by charging the vessel or heating above a reaction initiation temperature *etc.*) and stopping the

reaction in the vessel, is the residence time. For a continuous reaction this is not so intuitive, and an estimate can be made using the equation $\tau = V/Q$ where τ is the mean residence time, V is the reactor volume and Q is the volumetric flow rate [44]. This gives us a single number, which is not a good representation of the residence time within a CSTR. If ideal mixing is assumed (where there is no variation of composition throughout the vessel), the outlet will have a composition equal to that in the vessel. That is to say, with all components in the vessel intimately mixed, there is no reason for residence time to follow a single mean value; all fluid elements have equal probability of leaving the vessel at a given time. Instead, it follows a distribution function that can be defined as the residence time distribution (RTD). For a CSTR the RTD is given by [45]:

$$RTD(t) = \frac{1}{\tau} e^{-\frac{t}{\tau}}$$

The standard deviation for an exponential distribution of this type is given by τ (the inverse of the pre-exponential factor and the value of the mean residence time). This means for long residence times, the standard deviation will be correspondingly greater, a severe limitation for this type of reactor with long reaction times. As graphed below in figure 2.5, the increase in residence time has a detrimental impact on the observed deviation in the residence time. In effect, the longer residence time flattens the exponential decay in the residence time, meaning for short residence times, the CSTR will give a relatively narrow exponential distribution of residence time. For longer residence times the CSTR will give closer to a flat distribution as the exponential function is stretched.

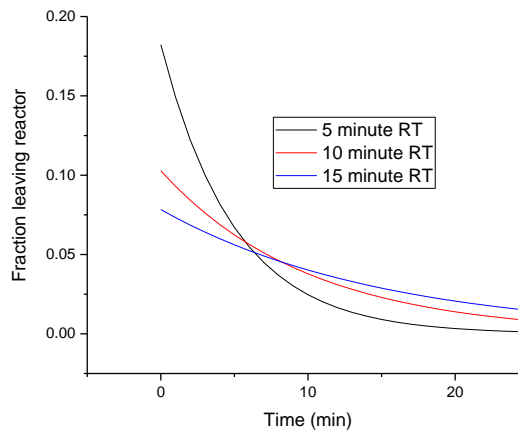


Figure 2.5: Graph showing how changing residence time stretches the distribution of residence times in a CSTR for 5 minute (black), 10 minute (red) and 15 minute (blue) residence time. None of the profiles show a sharp distribution in time, as predicted by an average residence time.

To overcome this long residence time distribution, a cascade of CSTRs can be used. This is where the outlet from one CSTR becomes the feed to the next as shown in figure 2.6. The separation of the vessels reduces the variance as the exponential residence time distribution is stretched less in each tank. By separating the reaction stages, it is also possible to control parameters as the reaction proceeds (e.g. a heating ramp as a reaction continues, with increasing heating in successive vessels), this is not possible in a single CSTR. The number of vessels and their associated equipment can however incur significant cost. As the number of reactors becomes very large, the residence time distribution begins to represent increasingly smaller volumes that flow sequentially through the reactor system. The ultimate extension of this case (i.e. an infinite number of CSTRs in series) is the reactor configuration shown below, the plug flow reactor.

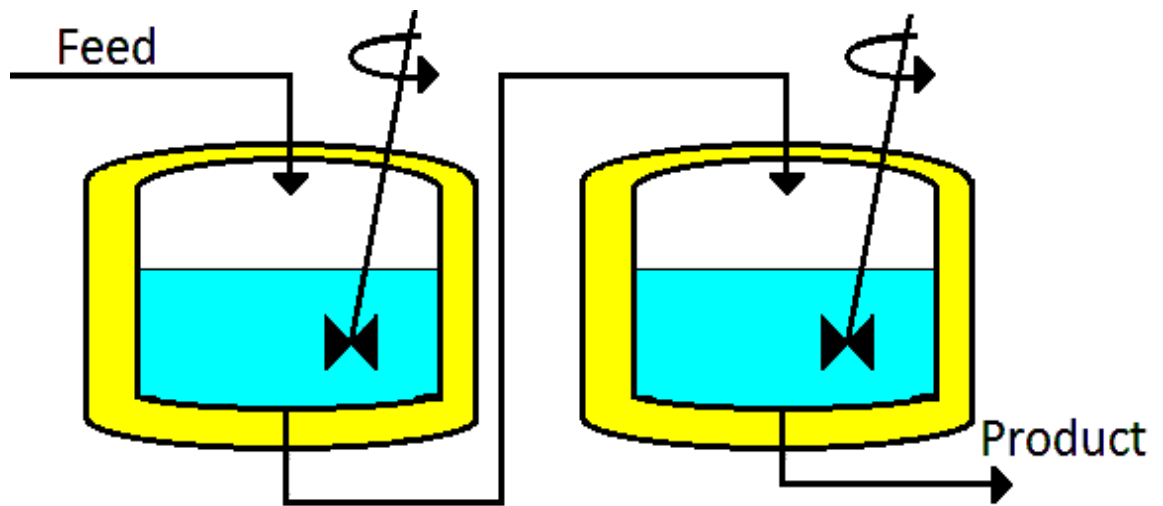


Figure 2.6: Diagram of a CSTR cascade with the outlet from one tank becoming the inlet to the next. Similar to a single CSTR, additional features such as vents and mixing aids can be included.

2.2.4.3 Plug Flow Reactor

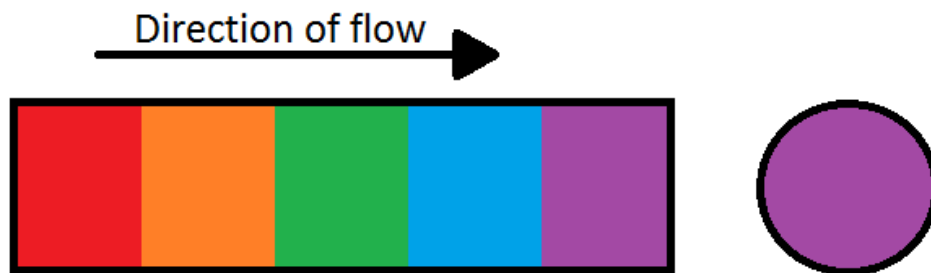


Figure 2.7: Simple diagram of a PFR. The colours across the width of the pipe are completely homogeneous (radial mixing) but there is no mixing between the different coloured slugs of liquid (axial mixing).

The plug flow reactor (PFR) is a model reactor used to describe a tubular reactor where there is perfect radial mixing (i.e. composition through a cross section of the tube is identical at all points) but no axial mixing (i.e. along the length of the tube the fluid does not mix). This can be thought of as separate ‘plugs’ of very small volumes moving through the tubular reactor, where these are completely mixed within an individual plug but do not interact with other plugs moving through the tube as

shown by the coloured blocks in figure 2.7.

For this type of reactor, the residence time should be a single value where the residence time is easily calculated from the volumetric flow rate, the cross sectional area of the reactor used and the length of the path through the reactor. The graph of the residence time distribution is given below in figure 2.8 for three PFRs operating with residence times equal to the CSTR graphs shown in figure 2.5. The distribution shows a Dirac delta function, where at all values of t except τ the function has a zero value. This means that residence time is controlled to a much greater degree than in a CSTR, even in real reactors where the distribution will not exactly follow these idealised models.

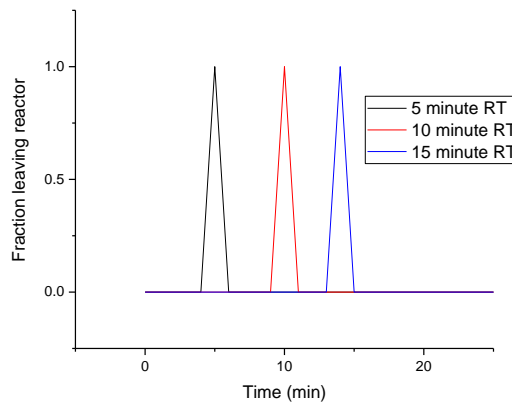


Figure 2.8: Residence time distribution for PFR for 5 minutes (black), 10 minutes (red) and 15 minutes (blue). The distribution is a sharp peak at the average residence time with minimal distribution.

Practically the assumptions of a PFR can be realised to a great degree in reactors using a simple pipeline configuration with turbulent flow. Turbulent flow ensures good heat transfer and mixing within the reactor and is not associated with extra equipment, as it is typically the flow regime encountered in larger scale fluid flow at reasonable flow rates.

The velocity profile of turbulent flow across the channel also lends itself to use in a

PFR, given that it is relatively flat (as shown in figure 2.9 below). The structure in the flow means that velocity at the wall is zero (assuming the no slip condition), but even at small distances from the wall, velocity is close to the maximum [46]. Due to the irregular nature of turbulent flow, there is some mixing of the fluid plugs in this type of reactor, so operation will not be ideal and there will be some variation around the Dirac distribution. Turbulent flow is very complex and can only be described statistically; vorticity is high and it cannot be said in which direction a very small fluid element will travel. For these reasons, some back flow will occur. Maintenance of the reactor can be more complex due to the lack of an open vessel, making physical cleaning difficult. On a small scale, the flow rates required for turbulent flow are generally too high to be readily applied but the reactor configuration can be achieved using small scale tubing and connectors. In this case, the PFR model can be modified to adapt to laminar flow, as described in the laminar tubular reactor detailed below.

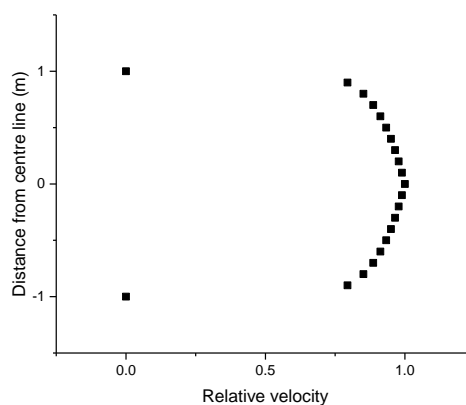


Figure 2.9: Typical velocity profile across a pipe for fluid flowing under a turbulent regime. Profile was calculated using the 1/7th power law. Typically, turbulent velocity profile is relatively flat with zero velocity at the wall.

2.2.4.4 Laminar Tubular Reactor

On a small scale (*i.e.* in narrow tubes with relatively small flow rates) laminar flow will dominate, which changes the basis of the PFR model. This is primarily due to a lack

of advective mixing, which limits heat and mass transfer radially in the tubing, and the velocity profile, which is not conducive to considering a plug flow. The flow is more structured in the laminar system and can be described analytically; it will not cause any back flow due to vorticity but will, however, cause greater dispersion due to the parabolic velocity profile (shown below in figure 2.10). Maximum velocity is twice the average velocity and there is a more gradual increase in velocity with distance from the wall of the vessel.

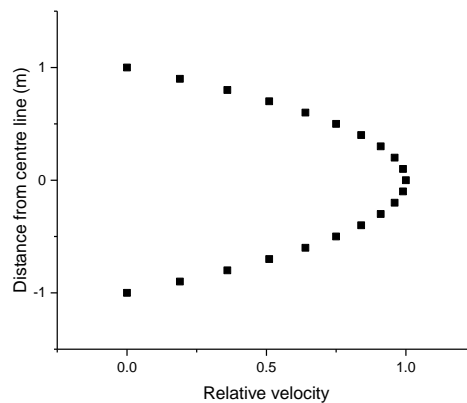


Figure 2.10: Velocity profile across a pipe for fluid flowing under a laminar regime. Profile was calculated by solving the Hagen-Poiseuille equation. The profile is parabolic with average speed of half the maximum.

This velocity profile causes a skewing of the residence time distribution towards longer times as shown in the example in figure 2.11 below. The idealised response of an ideal PFR is lost in this reactor configuration but control over the residence time is greater than with a CSTR. Compared to a PFR, a laminar tubular reactor would often not be preferred due to the poorer radial mixing, which can impede heat transfer and reagent mixing and the deviation from the almost ideal impulse response of the residence time in a PFR. On a small scale though where diffusion mixing, or in-line mixing (e.g. in a t-mixer) is sufficient and heat transfer will be sufficiently rapid, laminar flow reactors can be useful. These reactors offer some of the advantages of the PFR over the CSTR (including better residence time control and lack of equipment

such as active mixing devices) but introduce some disadvantages (primarily the poor mixing outlined above).

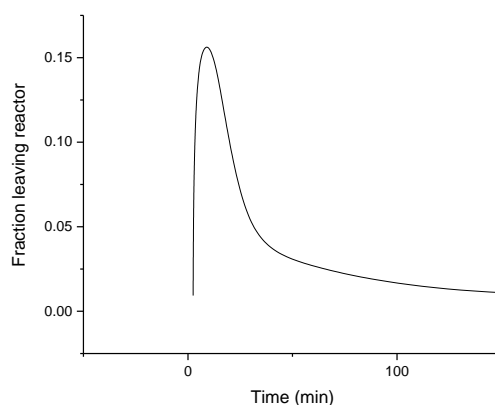


Figure 2.11: Typical residence time distribution for a laminar tubular reactor. Profile was calculated by considering the laminar velocity profile and subdividing the flow area into a series of annulus cross sections.

2.3 Aims

The main aim of this chapter is to investigate the possibility of using a bench-top continuous reactor for the production of gold colloid. The target production of 3-5 mL/ min should give production of nanoparticles on the scale of grams/ hour. This allows for a continuous production on a similar scale to current batch production methods. The motivation was development towards a method of continuous production which would maintain the same quality of colloid as in batch production but with a view to reducing manpower requirements and ensuring a continuous supply for further processes e.g. conjugation.

As an initial investigation, the fundamental model reactors show above were to be used, namely the CSTR and laminar tubular reactor. These were to be used to generate gold colloid and the product compared with batch synthesis, primarily by sizing as this is a good indicator of the quality of the colloid for use. Some

investigation was carried out into the batch preparation of gold nanoparticles to further inform the development of a continuous process.

2.4 Results and Discussion

2.4.1 Batch Production of Gold Colloid

A two-step synthesis was identified as the most likely to give monodisperse colloid and be versatile enough to encompass a range of particle sizes. Batch tests were run on the most common synthesis methods along with the BBI method of producing 10 nm colloid.

As the citrate reduction was the most widely used synthesis for gold colloid, this was tested first. Seeds were formed from citrate reduction to give 14 nm gold seeds [47]. This method gave a ruby red sol which had a narrow plasmon peak in the extinction spectrum, as previously reported.

Reducing the time at reflux did not have any noticeable effect, as long as the solution was vigorously refluxing for at least 5 minutes after addition of the trisodium citrate, indicating that in a reactor a residence time of five minutes or greater would suffice for colloid production. This was in keeping with observations by Frens on the speed of reduction by trisodium citrate at boiling [18].

Sodium borohydride reduction to give gold nanoparticles with citrate capping was also carried out. This required a longer reaction time for the observed colloid colour to develop, compared with citrate reduction. The borohydride solution appeared to decompose over time at room temperature, so was prepared immediately before use in each case.

Both borohydride reduced and citrate reduced colloid were characterised by extinction spectroscopy and the raw spectra are shown in figure 2.12. The peak extinction was at a higher wavelength for citrate reduced colloid (as shown in figure

2.13), indicating a larger nanoparticle size. Size was measured by DLS at 20 nm for citrate and 12 nm for borohydride reduced colloids. Borohydride reduced colloids had a much higher fwhm (figure 2.14), indicating a more polydisperse colloid. The constancy of the borohydride synthesis was poorer, with higher standard deviation for both of the measures shown in figures 2.13 and 2.14.

Stability for borohydride reduction was also poorer than for the citrate reduced colloid with large flocs formed after around one month of storage at room temperature, whereas the citrate reduced colloid appeared stable for at least two months.

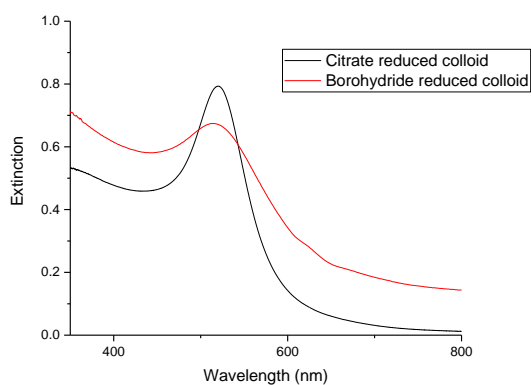


Figure 2.12: Extinction of batches of citrate reduced gold colloid (black) and borohydride reduced gold colloid (red). The citrate colloid has a much sharper extinction peak. Results are single representative spectra.

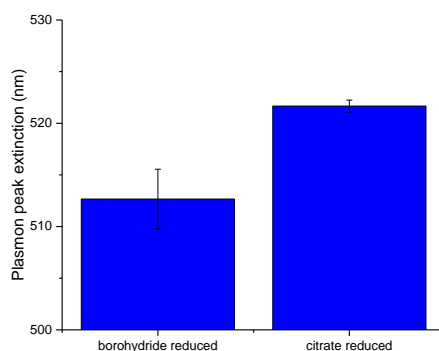


Figure 2.13: Plasmon peak extinction of batch prepared borohydride reduced and citrate reduced gold colloids. Results shown are the average of three experiments and error bars show one standard deviation.

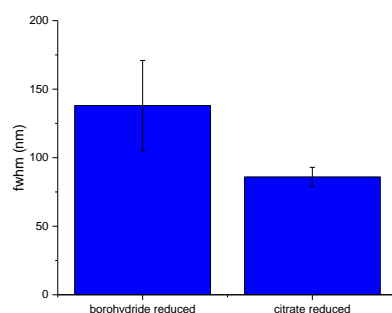


Figure 2.14: Fwhm of batch prepared borohydride reduced and citrate reduced gold colloids. Results shown are the average of three experiments and error bars show one standard deviation.

For the second stage of the colloid production, a growth step was employed. Using ascorbic acid as a reducing agent and citrate as the capping agent, citrate nanoparticles from the Turkevich- Frens method were used as seeds. The ascorbic acid reduction gave a colloid in less than five minutes, which showed a plasmon peak at a higher wavelength and of greater extinction than the seeds but remained narrow as shown in figure 2.15. Unseeded growth gave very broad extinction spectra with a

poorly defined peak extinction. The peak extinction increased slightly from seeds to the grown particles and a much higher peak extinction was observed for the unseeded growth as shown in figure 2.16. The fwhm (figure 2.17) showed the same trend as the peak extinction. Overall, the quality of the colloid formed by unseeded ascorbic acid reduction was poor but ascorbic acid growth with seeds gave larger, good quality colloid as shown by the plasmon peak extinction and fwhm (figures 2.16 and 2.17). This is because the ascorbic acid is not a powerful enough reducing agent to rapidly reduce the gold ions in solution but will reduce onto a gold surface as this is autocatalytic [48]. Ascorbic acid is also not reported to promote a specific structure in the initial reduction of the gold ions. The resulting colloid therefore has a variety of sized and shaped particles forming over a relatively long time scale, which are stabilised by the added citrate ions. The lack of heating means that, despite citrate being present, dicarboxylic acid does not form to structure the particles before nucleation. One previous report used ascorbic acid as a reducing agent [49] and obtained a purple colloid. The colloid had a broad extinction peak at 600 nm and was sized at 7 nm. The results of this paper appear to be contradictory since it is common that small gold nanoparticles have a red colour and extinction at closer to 500 nm (see figure 2.1).

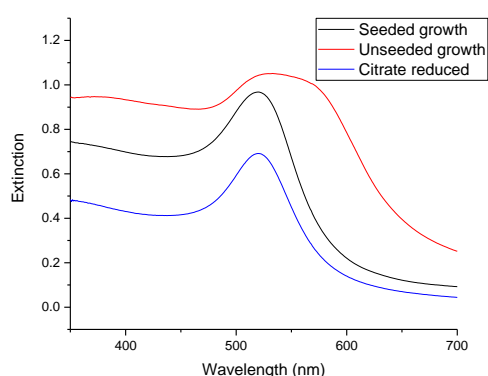


Figure 2.15: Extinction of citrate reduced gold colloid seeds (blue) and ascorbic acid grown gold nanoparticles with seeds (black) and without seeds (red). Results are

single representative spectra. Note the change in extinction profile for the unseeded growth.

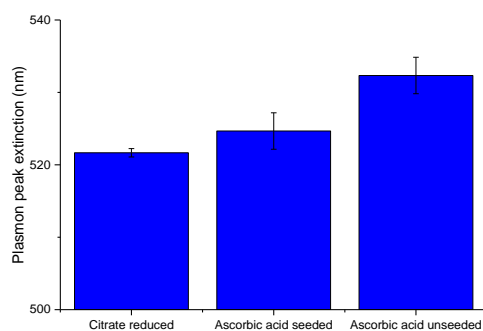


Figure 2.16: Plasmon peak extinction of citrate reduced gold seeds and ascorbic acid grown gold nanoparticles. Results shown are the average of three experiments and error bars show one standard deviation.

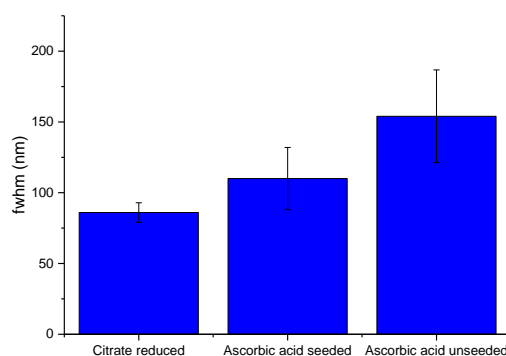


Figure 2.17: Fwhm of citrate reduced gold seeds and batch ascorbic acid grown gold nanoparticles. Results shown are the average of three experiments and error bars show one standard deviation.

The BBI Solutions method of making 10 nm colloid was taken as a typical model of the commercial method of producing colloid. As a current commercial method,

limited discussion is given of the experimental detail. In general terms, the method employed solution phase reagents which were filtered and then boiled, before solution phase reduction at a controlled temperature. Colour development was rapid, demonstrating the efficient reduction reaction in this method. Colloid size is more consistent than with academic methods of gold colloid production and dispersity is very low, with a standard deviation of 1 nm required for every batch. Batches are individually sized by TEM to determine the mean size and standard deviation of the nanoparticles.

2.4.1.1 Reducing Dissolved Oxygen Concentration and Colloid Quality

To eliminate unnecessary steps and for the simplification of a continuous production, the standard BBI Solutions procedure was pared back to the fewest viable steps. Initially with only heating and mixing of the reagents, the colloid formed was demonstrably not as monodisperse as the BBI Solutions commercial sample received, as measured by DLS. Boiling the gold solution before reduction for five minutes was sufficient to produce colloid comparable with that produced using the BBI method. Initially boiling the solution may alter the levels of dissolved oxygen (DO) in the gold (III) solution to be reduced and this is investigated in more detail below. Some differences were observed but mostly in total size, not in dispersity- this may be due to difficulty in accurate temperature control using the available lab equipment.

The step of filtering may act to remove any contaminant dust. However, all components in these prepared solutions should be stable for a reasonable time, with correct storage. Removal of any particles will give a more homogeneous nucleation environment upon reaction with the reducing solution but this was not evident in experiments carried out here so the filtration step was excluded.

As the pre-reaction boiling seemed to be a significant step in generating good quality colloid, an attempt was made to identify the reason for this. As the boiling will reduce the levels of oxygen in the gold solution, various de-oxygenation methods were used,

to try and correlate this to the size and dispersity of the colloid formed. The results from a Winkler titration to determine dissolved oxygen concentration were broadly in keeping with those in literature [50]. Table 2.1 gives the methods used to de-aerate the solutions, results from the Winkler titration and the DO concentration from a literature source [50] or from Henry's law for equilibrium conditions. Parameters for Henry's law and a comprehensive explanation of the theory is given by Sander [51]. The parameters used in Henry's law were those for oxygen given by Sander in the appropriate tables.

Table 2.1: Methods of de-aerating water and measured DO levels with predicted values.

Method	O ₂ concentration (mg/ L ± standard deviation)	Predicted (mg/ L)
Doubly distilled water- 20 °C	8.9 ± 0.2	8.8 (Henry's law)
Doubly distilled water- reduction conditions	5.1 ± 0.1	4.9 (Henry's law)
Boiling doubly distilled water	3.1 ± 0.2	1 (boiling 30 min, 1 atm)
Vigorous N ₂ bubbling through doubly distilled water at reduction conditions	1.4 ± 0.1	0.5 (5 min N ₂ purging with <5% O ₂)
Boiling doubly distilled water under vacuum at reduction conditions	1.3 ± 0.2	0.30 (Boiling under reduced pressure 30 min)

The results show that, compared to the literature, experimentally obtained DO levels are higher but follow the same trend. This could be due to less time under degassing conditions (for boiling) and exposure to open air rather than using a sealed vessel (for N₂ purging).

Changing the de-aeration method causes substantial changes to the size of produced particles, as shown by the DLS sizing in figure 2.18. The z-average size (figure 2.19) showed a decrease with decreasing O₂ concentration, with the sample with no de-aeration having by far the largest size. The boiled sample was very similar to the BBI Solutions colloid, as these are made using essentially the same method. N₂ degassing and vacuum boiling both gave smaller sizes and lower O₂ concentrations. The coefficient of variance followed the same trend as z-average size with the most effective de-aeration giving the lowest variability.

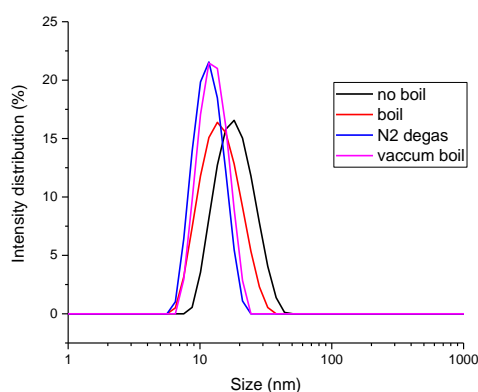


Figure 2.18: DLS sizing data for gold colloid produced by the BBI method with no boiling step (black), initial boiling step (red), nitrogen bubbling (blue) and vacuum

boiling at 60 °C (pink). Results are a single intensity weighted size profile for each sample.

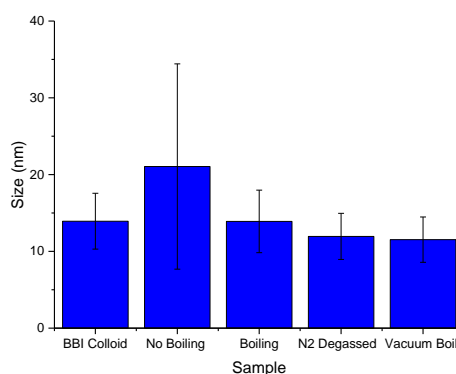


Figure 2.19: Z-average DLS size of gold colloid produced by the BBI method with no boiling step, initial boiling step, nitrogen bubbling and vacuum boiling at 60 °C. Results shown are the average of three experiments and error bars show one standard deviation.

Plotting the measured O₂ concentration with the size gave a weak correlation, particularly given the low number of points. A larger number of points, covering a wider range of dissolved oxygen concentrations, would be necessary to completely investigate this effect.

By separating the two required functions of de-aerating and heating it was possible to more effectively synthesise reliable quality colloid. This was demonstrated by the low coefficient of variance, calculated over a number of samples, for both N₂ bubbling and vacuum boiling. This may be because whilst boiling, the de-aeration is not an equilibrium process and as soon as boiling stops, DO levels will return to the levels predicted by Henry's law for the water. In between the termination of boiling (to lower the solution to the reduction temperature) and addition of the reducing mixture, air will continue to re-dissolve in the water until it reaches saturation. If reduction is carried out before this point, the level of O₂ in solution will be variable depending on the time given for cooling. If reduction is carried out after saturation is reached, then the boiling step has no effect on DO levels. The elimination of boiling

as a required step should also allow more ready transfer of this colloid production method to a continuous reactor.

2.4.1.2 Extinction Spectroscopy for Small Colloids

As outlined in the introduction, extinction spectroscopy is not suitable for differentiating very small nanoparticle colloids, with diameter less than around 10 nm. This was found to apply to the similar colloids formed under various levels of DO reduction. The DLS sizing (figure 2.20) and normalised extinction spectra (figure 2.21) for two separate colloids prepared by the BBI method with different de-aeration methods used alongside a sample of commercial BBI colloid are shown below.

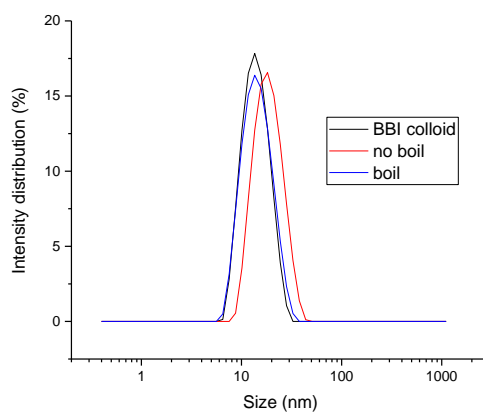


Figure 2.20: DLS sizing data for BBI commercial gold colloid (black) and gold colloid produced by the BBI method with no boiling step (red) and with a boiling step (blue).

Results are a single intensity weighted size profile for each sample.

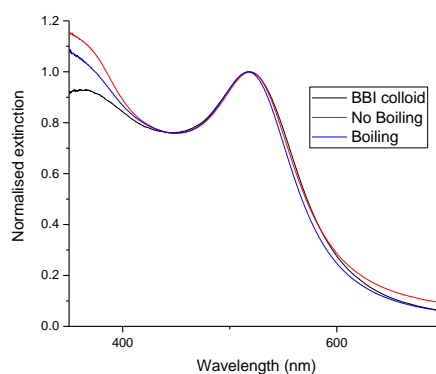


Figure 2.21: Normalised extinction of a sample of commercial BBI gold colloid (black) and gold colloid produced by the BBI method with no boiling step (red) and with a boiling step (blue). Results are a single extinction profile for each sample.

As can be seen in the DLS sizing, there appeared to be a clear distinction between the aerated colloid and the commercial BBI colloid/ boiling de-aerated colloid. This distinction was not evident in the extinction spectra. The logarithmic scale for size in the DLS sizing graph tends to mask the disparity so this is not visually apparent. From the extinction spectroscopy, the fwhm appears very similar and it may erroneously be concluded from this that the size and dispersity of the colloids were approximately

equal.

From Mie theory and in literature it is often reported that the plasmon peak extinction correlates to the size of the colloid [52] and the fwhm correlates to the dispersity of the colloid [53-55]. This does not seem to be a useful measure for these very small nanoparticles and DLS is the more useful measurement for small nanoparticles.

2.4.2 Continuous Production

2.4.2.1 CSTR

Initially two stages of seed generation and growth were chosen, split and performed in a small scale continuous reactor.

The first step of colloidal seed generation was carried out in a simple CSTR type arrangement with a three necked flask used as the vessel. Initially a syringe pump was used to flow in reagents, which placed limits on the period of operation and the residence time in the vessel. The vessel was pre-charged with the appropriate volume of reagent solutions to speed the transition to steady state. The 25 mL charge volume, for a residence time of five minutes at the flow rate of 5 mL/min, was made up of 24.3 mL of $\text{HAuCl}_4 \cdot 3\text{H}_2\text{O}$ solution in the vessel and 0.7 mL of doubly distilled water containing trisodium citrate which was added after the chloroauric acid solution had reached reflux. This was allowed to reflux for five minutes before the flow on both inlet and outlet was started. Collections of 1 mL were taken every five minutes from the beginning of flow until the reactor had been running for 25 minutes. The extinction and DLS sizing of the aliquots was analysed off-line and results are shown in figure 2.22. Initially the peak extinction and fwhm are a good match with the batch results, with a peak of 522 nm and fwhm of 79 nm. These values increased quite rapidly, however, and there was a clear trend of increasing size over time when averaged over the reactor runs.

DLS sizing confirmed an increase in size over the reactor run time (figure 2.23). Initially the nanoparticle size was slightly larger than the batch experiments (24 nm vs 20 nm). This size was quite consistent between reactor runs but over time it became less so and the standard deviation between the runs became very large.

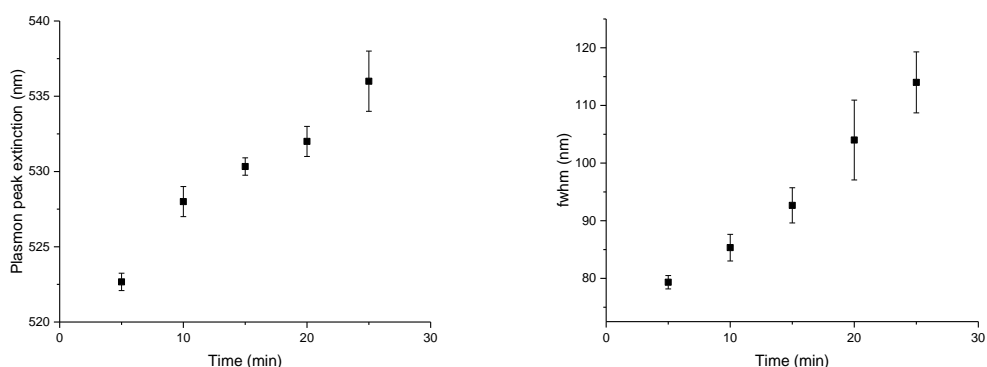


Figure 2.22: Plasmon peak extinction (left) and fwhm (right) for citrate reduced gold colloid produced in the CSTR. Results are the average of three experiments and error bars are one standard deviation.

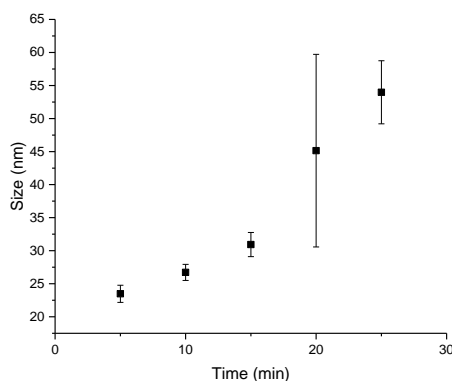


Figure 2.23: Z-average DLS sizing of gold particles synthesised by citrate reduction in a CSTR. Results are the average of three experiments and error bars are one standard deviation.

With the use of peristaltic pumps, the system could be operated for a much longer

time, due to the elimination of reagent volume as a limitation. To check that the short residence time did not contribute to the increasing size and dispersity, residence time was increased. The same CSTR set up as previously was used with a 150 mL charge volume, to give a 30 minute residence time at the outlet flow of 5 mL/min. The charge was boiled for 30 minutes before flow was begun. Aliquots were drawn for off-line extinction analysis every 30 minutes after the flow was begun. The experiment was run for 160 minutes to check whether the product from the reactor stabilised in this time. In-line extinction measurement was also used to check how information from this compared to off-line measurements.

The produced colloid still showed an increase in size as shown by the plasmon peak extinction in figure 2.24. The rate of increase was slower for the larger reactor but continued throughout the run time. As with the previous reactor dispersity, as shown by fwhm, increased during the reactor run time. The rate was slower with the larger tank volume and residence time but the increase continued for the full run time.

The in-line extinction compared well with the off-line analysis. The plasmon maximum extinction was a very good match between in-line and off-line, varying by a maximum of around 3 nm (figure 2.24). This indicated that in-line measurement was an effective way to continuously monitor gold production of this type for large deviations from the expected values. The fwhm measured was larger in each case but this was likely a result of the substantially lower resolution of the in-line spectrometer (figure 2.25). The increase over time in the fwhm appeared larger in the in-line measurements, initially differing by around 10 nm but differing by 20 nm by the end of the experiment. Again, this was likely due to the greater noise in the spectra obtained and the lower resolution of the spectrometer.

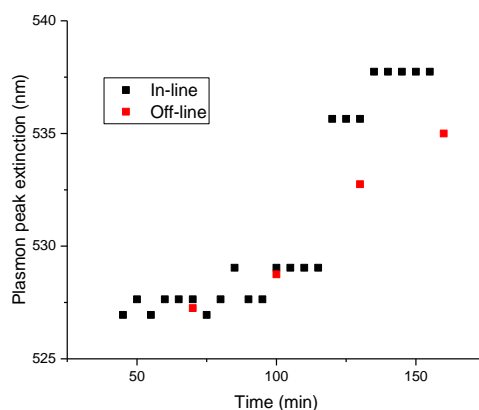


Figure 2.24: Plasmon peak extinction for citrate reduced gold colloid produced in the CSTR measured both in-line (black) and off-line (red). Boxcar averaging was applied at the point of in-line sampling, causing the observed step change in the in-line results.

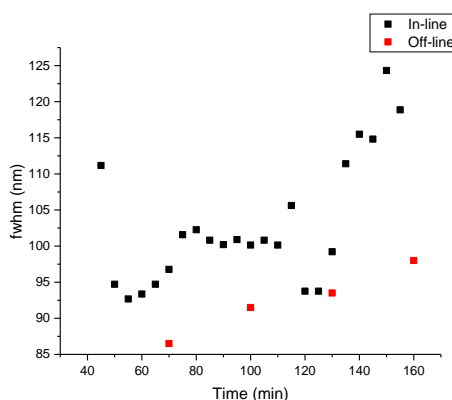


Figure 2.25: Fwhm for citrate reduced gold colloid produced in the CSTR measured both in-line (black) and off-line (red). Lower spectral resolution and boxcar averaging cause the in-line results to appear higher than the off-line.

For the second stage, where seeds were grown to larger particles, a CSTR was again employed. Initially using the limited volume from a syringe pump, volumes of reagents were chosen to match as closely as possible those used in the batch experiment. With the limited equipment, mixed solutions had to be transferred into the vessel. 50 mL of a mixed solution containing trisodium citrate and

tetrachloroauric acid was infused from one syringe. Another 50 mL syringe infused the mixed solution of l-ascorbic acid and gold seeds. A 25 mL charge volume of 12.5 mL of each of these mixed solutions was added to the reactor. This initiated the reaction and flow was started five minutes later (the residence time in the reactor being five minutes). After five minutes, the colloid obtained was a good match to that obtained in batch conditions; both had a plasmon maximum extinction at the same value (525 nm) but fwhm was higher for the CSTR (106 nm v 80 nm). The colloid produced in the CSTR rapidly deteriorated however and the collected colloid after 25 minutes had peak extinction at 560 nm and fwhm of 116 nm. This reaction displayed the same general trends in fwhm and peak extinction as for the nucleated generation of new gold colloid in a CSTR but with far more inconsistency between reactor runs. Both fwhm and plasmon peak extinction increased over time as shown in figure 2.26.

Size, as indicated by DLS shown in figure 2.27, also increased over the reactor run time. Initially the size was substantially larger in the CSTR than the batch synthesis (35 nm v 24 nm) and this continued to increase over time. This result supports previous observations with the CSTR. The initial larger size in the CSTR could be due to the use of mixed reagents, as this may alter the initial steps in the reduction process.

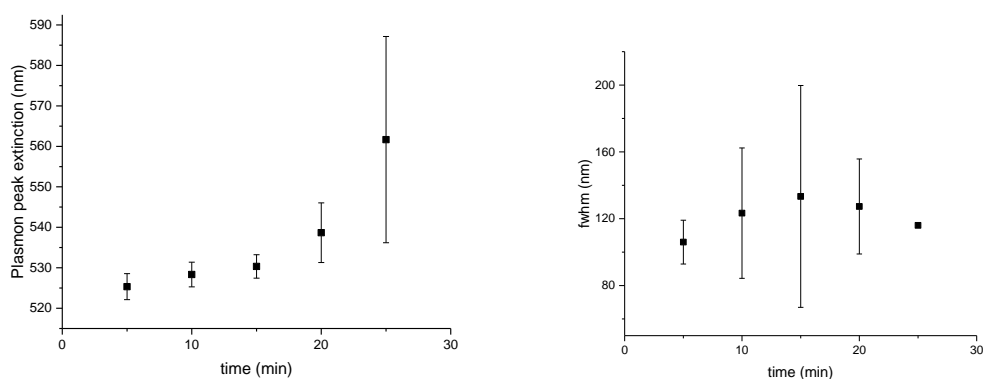


Figure 2.26: Plasmon peak extinction (left) and fwhm (right) for ascorbic acid grown gold colloid produced in the CSTR. Results displayed are the average of three experiments with error bars of one standard deviation. Note the apparent

downward trend after 15 minutes on the fwhm graph and lack of error bars on the final point. This is caused by a first then a second sample having fwhm so large it could not be measured in the recorded spectral range.

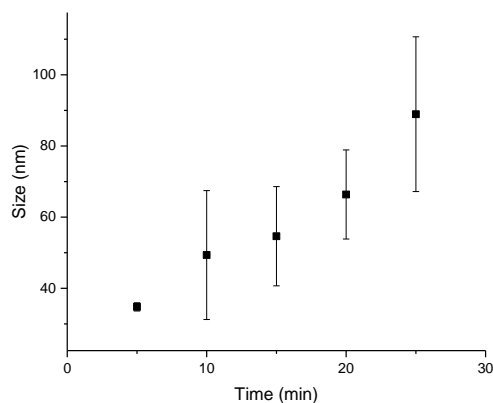


Figure 2.27: Z-average DLS sizing of gold particles grown by ascorbic acid in the CSTR. Results displayed are the average of three experiments with error bars of one standard deviation.

In all cases using a CSTR, a trend of increasing dispersity and plasmon peak extinction with time was observed. This can be explained by considering jointly the processes of nucleation and growth in forming the colloid and the characteristics of the CSTR configuration. As in figure 2.28, the reduction of chloroauric acid to gold nanoparticles to can be simplified to essentially a single step where the citrate added is oxidised to give the acetone dicarboxylic acid, which then polymerises with and reduces the gold (III) ions to give particles and the observed ruby red colloid. If the chloroauric acid is homogeneously heated to approximately 100 °C and the trisodium citrate is added quickly and mixed rapidly into the vessel, the reduction of the gold (III) will occur effectively simultaneously throughout the vessel. The nucleation of new gold (0) will then occur everywhere at the same time (figure 2.28).

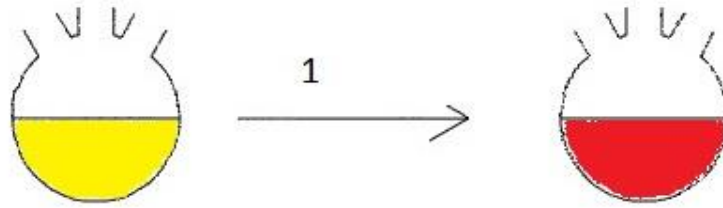


Figure 2.28: The reduction of chloroauric acid (yellow) in batch synthesis to gold nanoparticles (red) by citrate.

If this same simplification is applied to a CSTR with a pre-loaded charge volume (figure 2.29), the first step remains as in batch synthesis; at all points in the tank the reduction of the gold (III) ions causes the nucleation of gold particles in step 1. However, in a CSTR, flow is started at this point and the outlet from the tank will have the same composition as the vessel, assuming good mixing. The inflow of new chloroauric acid and citrate rapidly heats up to the tank temperature of 100 °C and undergoes reaction in step 2. This reaction meets the existing colloidal particles in the vessel and can use these as seeds rather than nucleating new particles. Existing particles are grown in the tank, rather than new particles of consistent size being formed in step 3. This will continue, with increasing size until the particles become unstable or it becomes energetically more favourable to nucleate new particles than grow existing large particles. This explains the general increase in size over time.

The slower increase in the larger volume CSTR is also accounted for, as the larger number of particles in the CSTR will mean the added gold causes less of a size increase in each particle. This will slow the observed rate of size increase, as observed. This suggests that rate of increase should scale with the residence time but be independent of the total flow rate into the reactor.

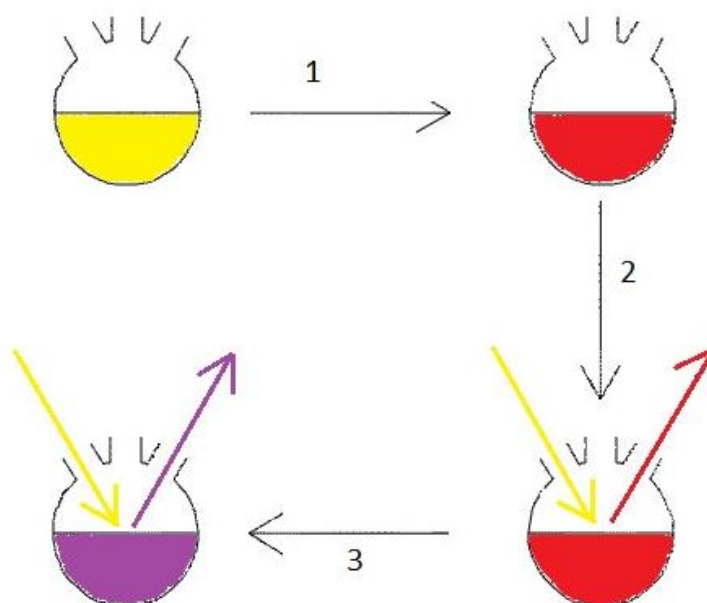


Figure 2.29: The reduction of chloroauric acid (yellow) to smaller gold nanoparticles (red) and growth of these to large particles (purple) in a CSTR.

The increase in dispersity can also be explained by the properties of the CSTR, primarily the residence time distribution. As shown in the introduction, the residence time in an ideal CSTR is represented by an exponential decay. Figure 2.30 shows the comparison between the ideal CSTR and that observed in the small three necked flask used for CSTR experiments shown above. The distribution in residence time, however, contributes to the increasing dispersity in the CSTR as particles now have unequal times in the reactor, during which they will have a correspondingly unequal time to meet incoming Au (III) and hence potentially differing amounts of subsequent growth after nucleation. This differing amount of growth means some particles, on leaving soon after formation, remain a similar size to that expected from batch synthesis. Other particles remaining for longer in the vessel are larger and will continue to grow further in size from that expected and dispersity will increase over time. This explains why, despite lack of competition between nucleation and growth, the ascorbic acid growth of the gold seeds also displays an increase in size and dispersity of the nanoparticles formed over time.

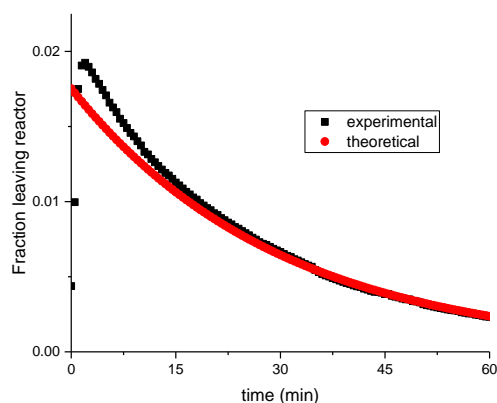


Figure 2.30: Residence time distribution comparison for a theoretical model CSTR (red) and for the CSTR used in the above experiments (black).

A single CSTR therefore seems unsuitable for the nucleation and growth of gold nanoparticles due to instability in the size of nanoparticles produced as measured by both extinction and DLS. Increasing the residence time by increasing the volume in the tank slowed the rate of size and dispersity increase but both measures still increased. Adding further CSTRs in a cascade arrangement would be more effective at reducing the dispersity as the residence time profile begins to approach that of a tubular reactor but the use of multiple CSTRs is problematic from an equipment point of view.

2.4.2.2 Tubular Reactor

As outlined in the introduction, a PFR is challenging to realise for a reaction on a small bench-top scale due to the difficulty in achieving turbulent flow. A laminar tubular reactor can be employed. Problems in this reactor for the production of gold are likely to be fouling of the reactor material, as identified by numerous literature works, and difficulty in accommodating multiphase flow in the small tubes

Initial experiments with the citrate reduction of chloroauric acid, showed that boiling was not necessary for the reduction but even at 90 °C the reaction rate was much

slower. For production of gold seeds in a tubular reactor, the citrate reduction was unsuccessful. It proved difficult to give a 5 minute residence time since boiling gave multiphase flow, with the volume of the vapour bubbles forcing any remaining liquid through the tubes very rapidly. Performing the reaction at 90 °C was not successful as the reaction was too slow to be completed within the limited tubing length. Work close to the boiling point of the liquid presented some difficulties to the operation of a small tubular reactor, such as above, where multiphase flow cannot readily be accommodated.

Since the ascorbic acid growth of seed particles could be carried out rapidly at room temperature, it was more readily transferred into a tubular reactor and was carried out first. A simple tubular reactor was constructed from silicone connecting tubing, Teflon tubing for the reactor and Kynar γ -connectors. The Reynolds number in the main reactor tube was 13, indicating highly laminar flow, so mixing was only by molecular diffusion. Over 25 minutes of operation the plasmon maximum extinction shifted from 525 nm to 545 nm (figure 2.31). Over the same time, fwhm increased from 106 nm to 152 nm. Neither of these measures compared well to batch operating mode but initially the colloid matched the early stages of CSTR operation. The observed shift over the reactor run time in the plasmon maximum was slightly less than was observed in the CSTR. Fwhm increased by the same amount over the 25 minutes but variation in this value was much larger for the tubular reactor, indicating much greater instability between the reactor runs.

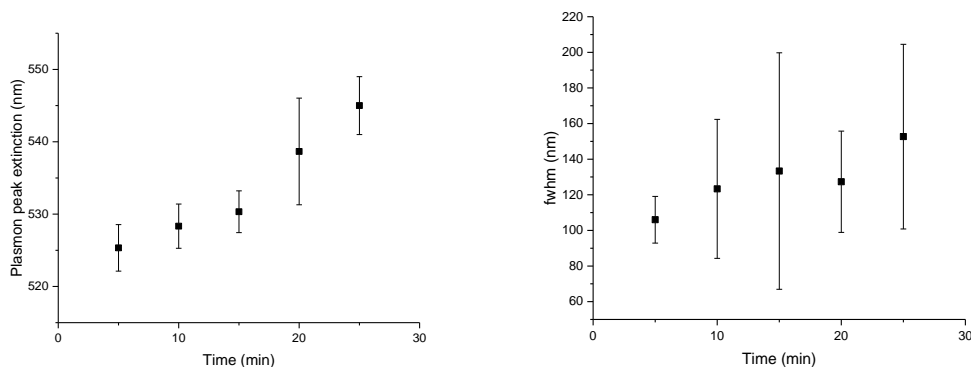


Figure 2.31: Plasmon peak extinction (left) and fwhm (right) for ascorbic acid grown gold colloid produced in the tubular reactor. Results displayed are the average of three experiments with error bars of one standard deviation

Since rapid reactions at ambient temperature were more amenable to use in a tubular reactor, to investigate a nucleating reaction, sodium borohydride reduction of gold (III) was performed.

Setting up a reactor for the reduction of gold (III) by NaBH_4 was very straight forward and has previously been published [40]. Using a five minute residence time, the reactor could be run for 70 minutes, giving colloid continuously. However, there was severe deterioration in quality over time as shown by the z-average size (figure 2.32) and multimodal DLS distributions (figure 2.33). Being limited to borohydride reduced colloid was also not ideal as it is not as widely used due to the size distribution, which is broader than for other methods. Fouling of the PTFE tubing used was severe and this could be a contributing factor in the changing particle size with time.

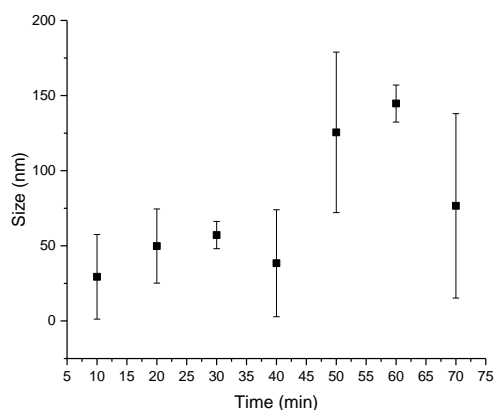


Figure 2.32: Z-average DLS sizing of borohydride reduced gold colloid from a tubular reactor. Results displayed are the average of three experiments with error bars of one standard deviation. Inconsistency in results was contributed to by samples precipitating out of solution.

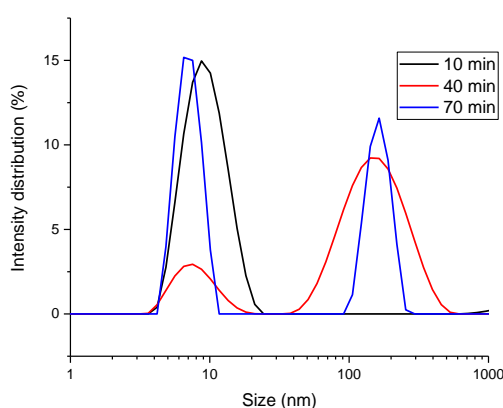


Figure 2.33: DLS sizing data for borohydride reduced gold colloid produced in the tubular reactor after 10 Minutes (black), 40 Minutes (red) and 70 Minutes (blue). Results are a single intensity weighted size profile for each sample.

The tubular reactor appeared to give less consistent colloid quality over reasonably modest run times than might have been supposed from the concept of the tubular reactor. There was an overall increase in the size of the nanoparticles but this was not consistent and the standard deviation between runs was very large. The most

likely cause of this was the fouling of the reactor materials during both the growth and nucleation of the nanoparticles as shown in figure 2.34. Purple coloured films were initially evident on the Kynar connectors and Teflon tubing and these eventually turned to shiny gold colouration. The silicon tubing was fouled with a dark material which appeared inconsistent across the inner surface of the tubing.

To attempt the tubular reactor format with a different synthesis method, BBI colloid was produced using a PTFE reactor coil in an oven as a reactor. Gold salt solution was fed in through one length of tubing by a peristaltic pump. In a separate tubing arm, a syringe pump infused the components of the reducing solution and these were mixed together before being combined with the gold solution inside the oven at the reduction temperature. The reactor was run for 4 hours, with aliquots drawn every 5 minutes for the first 30 minutes and every 30 minutes thereafter. After the 4 hour run time, fouling of the tubing was severe with large clusters observed and a purple colouration throughout. PTFE tubing was cleaned with *aqua regia* but any contaminated silicon tubing for the feeds and outlet from the coil was disposed of.



Figure 2.34: Images of the fouled reactor materials after gold reduction showing a connector and silicone tubing after disconnecting (left) and a selection of connectors (right). Note the increased fouling on one arm of the connectors, likely the side carrying the gold salt, which adheres to the wall and is reduced.

Fouling of the PTFE may present an issue for the consistent quality of the colloid

produced. Quality of the colloid was initially satisfactory, being somewhat larger than BBI colloid but showing good monodispersity. This deteriorated to give a multimodal distribution as shown in figure 2.35. The colloid produced sometimes gave single peaks after this point (e.g. 150 min plot in figure 2.35) but the production of nanoparticles was very unreliable as shown by the z-average size in figure 2.36. There was also some disagreement between the z-average calculation and the indicated intensity distribution from the DLS calculations. This indicated unstable results from a multimodal distribution which was difficult to analyse.

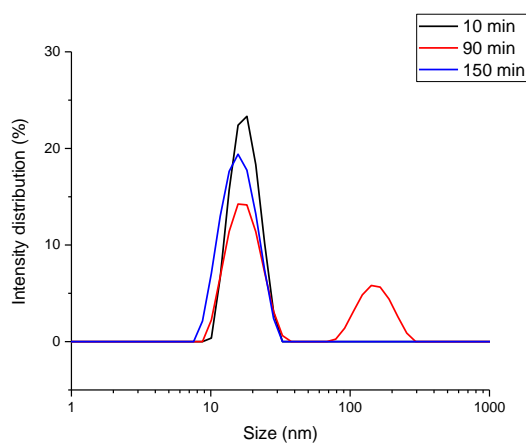


Figure 2.35: DLS sizing data for BBI method gold colloid produced in the tubular reactor after 10 minutes (black), 90 minutes (red) and 150 minutes (blue). Results are a single intensity weighted size profile for each sample.

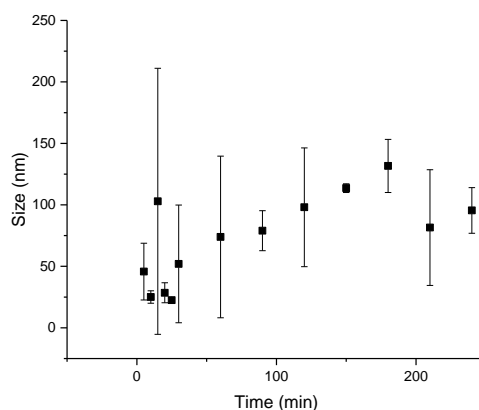


Figure 2.36: Z-average DLS sizing of gold nanoparticles produced by the BBI method in the tubular reactor. Results are the average of three experiments with error bars of one standard deviation. Inconsistency in results was contributed to by samples precipitating out of solution.

This instability of results and fouling had not been observed in the reduction of Au (III) using the BBI Solutions method in glassware. This may be caused by the increased wall effects and low shear in the narrow tubing, promoting adhesion of the forming metallic gold.

2.5 Conclusions

This work details an attempt to use a continuous stirred tank reactor to generate gold colloid using chemical reduction and expands on the examples in literature of a continuous production method. Gold colloid could reliably and reproducibly be made in batch synthesis, even for the relatively unrefined academic methods of colloid synthesis. This was not readily transferred to a continuous production and several challenges existed even on a modest mL/ min scale.

From these simple experiments with two of the most common reactor designs, it can be concluded that CSTRs are not suitable for the production of gold nanoparticles due to the imprecise nature of control over the reaction time and the unavoidable mixing

of reaction stages. In both reduction and growth steps, the residence time distribution and mixing of reaction stages in a CSTR gave an increase of particle size and size distribution with time.

From the first experiments with bench-top scale, laminar tubular reactors it appeared that these may also be unsuitable, since DLS sizing indicated that the dispersity of the nanoparticles produced was inconsistent over time. This appeared to be due to fouling of the materials used in the reactor as the Teflon tubing became severely coated with gold over time, which could adversely affect the colloid production in the tubing. The generation of colloid using borohydride reduction and an adapted BBI method did however demonstrate the possibility for continuous colloid production, but the dispersity from this method was relatively poor. The restrictions placed on the tubular reactor by the incompatibility with multiphase flow were also demonstrated; limited reduction reactions will be useable in the system and this greatly limits which synthesis pathways can be employed. Those which use a reducing agent powerful enough to reduce the Au (III) at sub-boiling temperatures (and realistically in a time scale of a few minutes) are the only ones which will be applicable.

Growth of seed crystals (such as shown above using ascorbic acid) in a tubular reactor may be suitable, due to the prevalence of reduction chemistry at room temperature for this type of reaction. If the size and dispersity could be made stable with time (again, probably with elimination of tubing fouling) this would be a likely target to be made continuous in a bench-top reactor. As part of a multi-step procedure the applicability of this would be severely limited without a continuous production of seed nanoparticles.

This work demonstrates that, commercially, it will require further investment in relatively complex reactors to facilitate the development of continuous production of gold colloid. It is relatively unlikely that a new process could be developed based on basic reactor technology but these more advanced reactors already exist in literature. Batch generation, despite the disadvantages, is likely to remain the most

effective way to operate in this market, unless there is a substantial increase in demand such that batch production cannot keep pace.

2.6 Future Work

The single CSTR configuration showed limited scope for further development, given the inherent incompatibility with the nanoparticle production. A cascade of CSTRs would be a productive next step, were this reactor type to be further exploited. As mentioned, this would be costly in terms of equipment.

For the laminar tubular reactor, improvements would be gained from eliminating or reducing the reactor fouling. This is a key challenge identified in literature when generating gold colloids and has again proven a challenge in this work. Modifications including pH adjustment and surface modification had previously been demonstrated to have limited success in literature. Changing materials of construction of the reactor may prove productive, whilst eliminating the use of silicone may reduce the rate of deterioration, as it appeared to be the most heavily fouled surface. The adhering of the fouling gold to Kynar and PTFE however suggested that eliminating the fouling will prove challenging by altering materials of construction. An investigation into the properties of the CSTR which protected it from fouling during reasonable run times would be informative. Perhaps the increased shear rate in the CSTR would reduce this effect whereas in the small tubes, where wall effects dominate, the reducing gold would readily adhere. Investigating larger tubing, which would have reduced wall effects, could be useful but under laminar flow it is likely that larger tubing would need some in-line mixing included, further complicating the reactor design.

As a further development, there are more specialised reactor types that may be suitable for reactions of this type. These include an oscillatory baffled reactor (OBR) which is currently used for crystallisation and a co-axial tubular reactor (CAT). The OBR is a tubular reactor with baffles along its length; in this reactor a forward and back oscillating motion is superimposed on the fluid, over the slower flow of material

from the reactor [56]. This oscillating flow acts to keep the fluid well mixed through the baffles, even at modest production rates. This would also act to keep shear rates at the wall higher than in a linear flow reactor, reducing the potential for fouling.

The CAT is a reactor recently published in literature with a central tube containing a silver salt solution and an outer annulus with a reducing agent [57]. Downstream, the separating pipe wall is removed and the laminar flow means the reaction is constrained to the boundary between the two fluids. The laminar flow means that mixing will be poor across the boundary but the issue of fouling would be solved by removing the reaction occurring at the walls.

2.7 Experimental

2.7.1 Chemicals and Characterisation

2.7.1.1 Solvents and Reagents

Chemicals were obtained from Sigma Aldrich and were of the highest quality available. Water used in the preparation of colloid and all solutions was obtained from a doubly distilled deionised water system. *Aqua regia* for cleaning was prepared by mixing 3 parts hydrochloric acid and 1 part nitric acid and stirring. The solution was left for 24 hours before use.

2.7.1.2 Extinction Spectroscopy

Off-line UV-Visible spectrophotometry was carried out using a dual-beam Cary-Win UV 300 spectrometer recording extinction between 800 – 300 nm with a resolution of 0.5 nm. Baseline correction was done with a distilled water blank.

On-line spectrophotometry was performed with an Ocean Optics 2000+ USB spectrometer using a portable light source, coupled to a cuvette holder with optical fibres. Five spectra with an integration time of 11 ms were averaged. A moving

average was applied to five pixels either side of each spectral point to reduce noise.

2.7.1.3 Dynamic Light Scattering Measurement

Dynamic light scattering results were recorded in a Malvern ZS zetasizer with a 633 nm laser. The number of runs per sample was determined by the in-built software. Results presented are the intensity size distribution directly from the instrument. Where single sizes are quoted these are the z-average size and are calculated by a standard method reported to conform to ISO 13321.

Disposable poly(methyl methacrylate) cuvettes were used for DLS and extinction measurements.

2.7.2 Batch Nanoparticle Synthesis

All glassware and stirrer bars used were cleaned with *aqua regia* before use and rinsed thoroughly with distilled water.

2.7.2.1 Citrate Reduced Nanoparticles

15 mg of HAuCl_4 trihydrate was dissolved in 150 mL of water and heated to boiling. Subsequently, 4.5 mL of a 1% w/w aqueous trisodium citrate solution was added and the mixture was refluxed for 30 minutes. This was modified for specific experiments detailed in the text (e.g. temperature reduced to 90 °C).

2.7.2.2 Borohydride Reduced Nanoparticles

15 mg of HAuCl_4 trihydrate was dissolved in 150 mL of water. To this, 9 mg trisodium citrate was added. Subsequently, 16 mg of sodium borohydride dissolved in 0.6 mL of ice cold water was added with vigorous stirring.

2.7.2.3 Ascorbic Acid Grown Nanoparticles

19.30 mg of HAuCl_4 trihydrate was dissolved in 50 mL of water and mixed with 50 mL of water containing 13.50 mg trisodium citrate. To this, 10.40 mg of L-ascorbic acid in 700 μL of water and 120 μL of seed colloid were added simultaneously. The reaction was stirred vigorously throughout and for at least five minutes after completion.

2.7.2.4 BBI Colloid

Dissolved gold salt was reduced using the commercial BBI method, which involved boiling the solutions in and an oil bath and then reducing heat to a set point for reduction.

Boiling before the introduction of the reducing solution was omitted for experiments detailed in the text.

For replacement of boiling by N_2 bubbling, a glass pipette was used to bubble N_2 directly into the solution. Stirring was maintained throughout. After five minutes of N_2 bubbling, the gas flow was stopped and the reducing solution added.

For vacuum boiling the solution was heated to the reduction conditions in an oil bath as above. In this set-up however a water jet vacuum tap was connected to the round bottom flask via a ground glass adaptor with two taps. After five minutes boiling, the vacuum tap could be closed and the second tap on the adaptor could be used to introduce the reducing solution from a syringe.

2.7.3 Continuous Reactors

2.7.3.1 Citrate Reduction in a CSTR

A 50 mL three necked flask with a water cooled condenser was used as the vessel. Heating and stirring was provided by a hotplate stirrer and oil bath. A Cole- Parmer 74900 series syringe pump was set up with two syringes, one containing 12 mg of HAuCl_4 in 60 mL of water and the other with 360 mg citrate in 60 mL of water. Solutions were infused at a total rate of 5 mL/ min from the syringe pump and removed by a peristaltic pump, manually calibrated to the same flow rate. The vessel was pre-charged with the appropriate volume of reagent solutions to speed the transition to steady state. The 25 mL charge volume was made up of 24.3 mL containing 2.5 mg $\text{HAuCl}_4 \cdot 3\text{H}_2\text{O}$ solution in the vessel and 0.7 mL of doubly distilled water containing 75 mg trisodium citrate which was added after the chloroauric acid solution had reached reflux. The reaction was allowed to reflux for five minutes before the flow on both inlet and outlet was started. Collections of around 1 mL were taken every five minutes, in glass vials, from the beginning of flow until the reactor had been running for 25 minutes.

2.7.3.2 Citrate Reduction in a CSTR- Longer Residence Time

Experimental set up was similar to above. The 50 mL three necked flask was replaced with a 250 mL three necked flask. The charge volume was increased to 150 mL made up of 121.5 mL water containing 12.5 mg HAuCl_4 . 3.5 mL of water containing 375 mg of trisodium citrate was added after the charge had started to reflux. Inlet and outlet flows were started after 30 minutes at reflux. Reagent reservoirs were increased to 58 mg of HAuCl_4 in 350 mL of water and 1.75 g of trisodium citrate in 350 mL of water. These were fed into the reactor via a peristaltic pump manually calibrated to give 5 mL /min total flow rate. Product was removed by a peristaltic pump similarly calibrated. Samples of around 1 mL were taken every 30 minutes from the beginning of flow for off-line analysis.

An in-line extinction measurement was also performed. This was done with a poly(methyl methacrylate) cuvette which was set up in the outlet line as a flow cell, with a silicone rubber seal and two glass capillaries as inlet and outlet. The working volume of 0.8 mL in the cell gave a reasonable turnover of liquid.

2.7.3.3 Ascorbic Acid Growth in the CSTR

A similar set up to the citrate reduction reaction was used for the ascorbic acid growth. The apparatus for heating and condensing were removed, as they were unnecessary. 12.5 mL of doubly distilled water containing 3.4 mg trisodium citrate and 5 mg $\text{HAuCl}_4 \cdot 3\text{H}_2\text{O}$ was added to 12.5 mL of water containing 2.6 mg of l-ascorbic acid and 30 μL of gold nanoparticle seeds in the CSTR. Flow into and out of the reactor was started 5 minutes after addition of the ascorbic acid and seeds.

A mixed solution containing 13.6 mg trisodium citrate and 20 mg tetrachloroauric acid in 50 mL water was infused, along with the mixed solution of 10.4 mg l-ascorbic acid and 120 μL gold seeds in 50 mL. Total flow rate into and out of the reactor was 5 mL/min.

2.7.3.4 Ascorbic Acid Growth in a Tubular Reactor

7.2 m of PTFE tubing with i.d. 1.6 mm was used as a reactor with a total flow rate of 3 mL/min for 5 min residence time in the coil. Silicone tubing was used where flexible tubing was required and tubing was joined using Kynar barbed connectors in either a straight or y-shaped arrangement. A peristaltic pump was used to dispense 1.5 mL/min of both a mixed solution containing 13.6 mg trisodium citrate and 20 mg tetrachloroauric acid in 50 mL water, along with a mixed solution of 10.4 mg l-ascorbic acid and 120 μL gold seeds in 50 mL. A single pump was used with parallel lengths of tubing used for dispensing each of the solutions into the reactor tubing. Samples were taken every 5 minutes.

2.7.3.5 Borohydride Reduction in a Tubular Reactor

A similar set up to the ascorbic acid growth was used. The reagents were replaced with 13.2 mg trisodium citrate and 22 mg tetrachloroauric acid in 110 mL water and 23.5 mg of sodium borohydride in 110 mL water. The borohydride solution was cooled in an ice bath. Each was dispensed into the reactor tubing at 1.5 mL /min. Samples were taken every 10 minutes.

2.7.3.6 BBI Colloid Reduction in a Tubular Reactor

A large glass flask contained gold salt solution. This had been degassed by N₂ bubbling and was kept under nitrogen for the length of the experiment. A peristaltic pump was used to dispense 2.85 mL/ min of the gold salt solution to the Teflon reactor tubing. Three syringes contained the reducing solution components in solution. A syringe pump infused 0.05 mL/ min of each. These solutions were mixed by Kynar γ -junctions prior to being combined with the gold solution in another γ -connector. The junction combining the reducing solution with the gold solution was kept inside the oven. Samples were collected every five minutes for the first 30 minutes then every 30 min thereafter.

2.7.4 Winkler Titration

To determine the concentration of dissolved oxygen, the Winkler titration was used. 50 mL samples of deionised water were de-aerated as they were for colloid production. To these water samples, 286 μ L of 1 M MnSO₄ solution was added, followed by 286 μ L of 1 M potassium iodide/ 10 M potassium hydroxide. This was then acidified with 142 μ L of 50% sulfuric acid. 15 mL was then removed for titration against 0.1 M Na₂S₂O₃·5H₂O with starch as an indicator. Titrations were repeated in triplicate.

2.8 References

1. Llevot, A. and D. Astruc, *Applications of vectorized gold nanoparticles to the diagnosis and therapy of cancer*. Chemical Society Reviews, 2012. **41**(1): p. 242-257.
2. Huang, X. and M.A. El-Sayed, *Gold nanoparticles: Optical properties and implementations in cancer diagnosis and photothermal therapy*. Journal of Advanced Research, 2010. **1**(1): p. 13-28.
3. Das, M., et al., *Review on gold nanoparticles and their applications*. Toxicology and Environmental Health Sciences, 2011. **3**(4): p. 193-205.
4. Fuller, S.B., E.J. Wilhelm, and J.M. Jacobson, *Ink-jet printed nanoparticle microelectromechanical systems*. Microelectromechanical Systems, Journal of, 2002. **11**(1): p. 54-60.
5. Stratakis, M. and H. Garcia, *Catalysis by Supported Gold Nanoparticles: Beyond Aerobic Oxidative Processes*. Chemical Reviews, 2012. **112**(8): p. 4469-4506.
6. Daniel, M.-C. and D. Astruc, *Gold Nanoparticles: Assembly, Supramolecular Chemistry, Quantum-Size-Related Properties, and Applications toward Biology, Catalysis, and Nanotechnology*. Chemical Reviews, 2003. **104**(1): p. 293-346.
7. Saha, K., et al., *Gold Nanoparticles in Chemical and Biological Sensing*. Chemical Reviews, 2012. **112**(5): p. 2739-2779.
8. Huang, J., et al., *Continuous-flow biosynthesis of silver nanoparticles by lixivium of sundried Cinnamomum camphora leaf in tubular microreactors*. Industrial & Engineering Chemistry Research, 2008. **47**(16): p. 6081-6090.
9. Williamson, I. and G.J. Allen, *Capillary fluid flow measurment and capillary flow device therefore*. 2014, Google Patents.
10. *Gold Nanaoparticle Kits: Innovacoat*. [cited 2014 23/07/2014]; Available from: <http://www.innovabiosciences.com/gold-conjugation-kits.html>.

11. Qu, W., et al., *Copper-Mediated Amplification Allows Readout of Immunoassays by the Naked Eye*. *Angewandte Chemie International Edition*, 2011. **50**(15): p. 3442-3445.
12. Polavarapu, I., et al., *Optical Sensing of Biological, Chemical and Ionic Species Through Aggregation of Plasmonic Nanoparticles*. *Journal of Materials Chemistry C*, 2014.
13. Baigent, C.L. and G. Müller, *A colloidal gold prepared with ultrasonics*. *Experientia*, 1980. **36**(4): p. 472-473.
14. Mafuné, F., et al., *Formation of Gold Nanoparticles by Laser Ablation in Aqueous Solution of Surfactant*. *The Journal of Physical Chemistry B*, 2001. **105**(22): p. 5114-5120.
15. Wender, H., et al., *Synthesis of gold nanoparticles by laser ablation of an Au foil inside and outside ionic liquids*. *Nanoscale*, 2011. **3**(3): p. 1240-1245.
16. Shang, Y., et al., *Synthesis of gold nanoparticles by reduction of HAuCl₄ under UV irradiation*. *Solid State Sciences*, 2013. **15**(0): p. 17-23.
17. Turkevich, J., P.C. Stevenson, and J. Hillier, *A study of the nucleation and growth processes in the synthesis of colloidal gold*. *Discussions of the Faraday Society*, 1951. **11**: p. 55-75.
18. Frens, G., *Controlled Nucleation for the Regulation of the Particle Size in Monodisperse Gold Suspensions*. *Nature Physical Science*, 1973. **241**: p. 20-22.
19. Gole, A. and C.J. Murphy, *Seed-Mediated Synthesis of Gold Nanorods: Role of the Size and Nature of the Seed*. *Chemistry of Materials*, 2004. **16**(19): p. 3633-3640.
20. Brust, M., et al., *Synthesis of thiol-derivatised gold nanoparticles in a two-phase Liquid-Liquid system*. *Journal of the Chemical Society, Chemical Communications*, 1994(7): p. 801-802.
21. Jana, N.R., L. Gearheart, and C.J. Murphy, *Evidence for Seed-Mediated Nucleation in the Chemical Reduction of Gold Salts to Gold Nanoparticles*. *Chemistry of Materials*, 2001. **13**(7): p. 2313-2322.

22. Ojea-Jiménez, I., et al., *Small Gold Nanoparticles Synthesized with Sodium Citrate and Heavy Water: Insights into the Reaction Mechanism*. The Journal of Physical Chemistry C, 2010. **114**(4): p. 1800-1804.
23. Polte, J., et al., *Mechanism of Gold Nanoparticle Formation in the Classical Citrate Synthesis Method Derived from Coupled In Situ XANES and SAXS Evaluation*. Journal of the American Chemical Society, 2010. **132**(4): p. 1296-1301.
24. Ji, X., et al., *Size Control of Gold Nanocrystals in Citrate Reduction: The Third Role of Citrate*. Journal of the American Chemical Society, 2007. **129**(45): p. 13939-13948.
25. Turkevich, J., *Colloidal gold. Part I*. Gold Bulletin, 1985. **18**(3): p. 86-91.
26. Jana, N.R., L. Gearheart, and C.J. Murphy, *Wet Chemical Synthesis of High Aspect Ratio Cylindrical Gold Nanorods*. The Journal of Physical Chemistry B, 2001. **105**(19): p. 4065-4067.
27. Ziegler, C. and A. Eychmüller, *Seeded Growth Synthesis of Uniform Gold Nanoparticles with Diameters of 15–300 nm*. The Journal of Physical Chemistry C, 2011. **115**(11): p. 4502-4506.
28. Tian, F., et al., *Surface enhanced Raman scattering with gold nanoparticles: effect of particle shape*. Analytical Methods, 2014. **6**(22): p. 9116-9123.
29. Oh, N. and J.-H. Park, *Surface Chemistry of Gold Nanoparticles Mediates Their Exocytosis in Macrophages*. ACS Nano, 2014. **8**(6): p. 6232-6241.
30. Schofield, C.L., et al., *Silver and Gold Glyconanoparticles for Colorimetric Bioassays*. Langmuir, 2006. **22**(15): p. 6707-6711.
31. Kolosova, A., et al., *Development of a colloidal gold-based lateral-flow immunoassay for the rapid simultaneous detection of zearalenone and deoxynivalenol*. Analytical and Bioanalytical Chemistry, 2007. **389**(7-8): p. 2103-2107.
32. Dasary, S.S.R., et al., *Gold Nanoparticle Based Label-Free SERS Probe for Ultrasensitive and Selective Detection of Trinitrotoluene*. Journal of the American Chemical Society, 2009. **131**(38): p. 13806-13812.

33. Kelly, K.L., et al., *The Optical Properties of Metal Nanoparticles: The Influence of Size, Shape, and Dielectric Environment*. The Journal of Physical Chemistry B, 2003. **107**(3): p. 668-677.
34. Agnihotri, S., S. Mukherji, and S. Mukherji, *Size-controlled silver nanoparticles synthesized over the range 5-100 nm using the same protocol and their antibacterial efficacy*. RSC Advances, 2014. **4**(8): p. 3974-3983.
35. K, L., et al., *Sub-20nm node photomask cleaning enhanced by controlling zeta potential*. SPIE Proceedings, 2012. **8522**.
36. Wagner, J., et al., *Generation of metal nanoparticles in a microchannel reactor*. Chemical Engineering Journal, 2004. **101**(1-3): p. 251-260.
37. Wagner, J. and J.M. Köhler, *Continuous Synthesis of Gold Nanoparticles in a Microreactor*. Nano Letters, 2005. **5**(4): p. 685-691.
38. Shalom, D., et al., *Synthesis of thiol functionalized gold nanoparticles using a continuous flow microfluidic reactor*. Materials Letters, 2007. **61**(4-5): p. 1146-1150.
39. Yang, S., et al., *Continuous synthesis of gold nanoparticles and nanoplates with controlled size and shape under UV irradiation*. Colloids and Surfaces A: Physicochemical and Engineering Aspects, 2007. **296**(1-3): p. 37-44.
40. Lohse, S.E., et al., *A Simple Millifluidic Benchtop Reactor System for the High-Throughput Synthesis and Functionalization of Gold Nanoparticles with Different Sizes and Shapes*. ACS Nano, 2013. **7**(5): p. 4135-4150.
41. Murphy, C.J., S.E. Lohse, and J.R. Eller, *Continuous flow reactor and method for nanoparticle synthesis*. 2014, Google Patents.
42. Lazonby, J. and D. Waddington, *The Essential Chemical Industry*. 2013.
43. Coulson, J.M., et al., *Fluid Flow, Heat Transfer and Mass Transfer*. Coulson and Richardson's Chemical Engineering. Vol. one. 1999, Oxford: Butterworth-Heinemann.
44. Coulson, J.M., et al., *Chemical and Biochemical Reactors and Process Control*. 3rd ed. Coulson and Richardson's Chemical Engineering, ed. J.F. Richardson and D.G. Peacock. Vol. 3. 1994, Oxford: Pergamon.

45. Grady Jr., C.P.L., G.T. Daigger, and H.C. Lim, *Biological Wastewater Treatment, Second Edition, Revised and Expanded*. 1999, New York: Marcell Dekker, Inc.
46. G, I.E., *DOE Fundamentals Handbook: Thermodynamics, Heat Transfer and Fluid Flow*.
47. Krpetić, Ž., et al., *Importance of Nanoparticle Size in Colorimetric and SERS-Based Multimodal Trace Detection of Ni(II) Ions with Functional Gold Nanoparticles*. *Small*, 2012. **8**(5): p. 707-714.
48. Jana, N.R., L. Gearheart, and C.J. Murphy, *Seed-mediated growth approach for shape-controlled synthesis of spheroidal and rod-like gold nanoparticles using a surfactant template*. *Advanced Materials*, 2001. **13**(18): p. 1389.
49. Sun, K., et al., *Preparation and characterization of gold nanoparticles using ascorbic acid as reducing agent in reverse micelles*. *Journal of materials science*, 2009. **44**(3): p. 754-758.
50. Butler, I.B., M.A.A. Schoonen, and D.T. Rickard, *Removal of dissolved oxygen from water: A comparison of four common techniques*. *Talanta*, 1994. **41**(2): p. 211-215.
51. Sander, R., *Compilation of Henry's law constants (version 4.0) for water as solvent*. *Atmospheric Chemistry & Physics*, 2015. **15**(8).
52. Yguerabide, J. and E.E. Yguerabide, *Light-Scattering Submicroscopic Particles as Highly Fluorescent Analogs and Their Use as Tracer Labels in Clinical and Biological Applications: I. Theory*. *Analytical Biochemistry*, 1998. **262**(2): p. 137-156.
53. Larmour, I.A., K. Faulds, and D. Graham, *SERS activity and stability of the most frequently used silver colloids*. *Journal of Raman Spectroscopy*, 2012. **43**(2).
54. Scaffardi, L.B., et al., *Sizing gold nanoparticles by optical extinction spectroscopy*. *Nanotechnology*, 2005. **16**(1): p. 158.
55. Jain, P.K., et al., *Calculated Absorption and Scattering Properties of Gold Nanoparticles of Different Size, Shape, and Composition: Applications in Biological Imaging and Biomedicine*. *The Journal of Physical Chemistry B*, 2006. **110**(14): p. 7238-7248.

56. Lawton, S., et al., *Continuous Crystallization of Pharmaceuticals Using a Continuous Oscillatory Baffled Crystallizer*. *Organic Process Research & Development*, 2009. **13**(6): p. 1357-1363.
57. Baber, R., et al., *Synthesis of silver nanoparticles in a microfluidic coaxial flow reactor*. *RSC Advances*, 2015. **5**(116): p. 95585-95591.

3 Computer

Simulation of a DNA

Assembly Assay

3.1 Abstract

Whilst developing a novel nanoparticle assembly assay, based on DNA assembly, it was found that current tools for the understanding of dynamic DNA structure were either very specialist and computationally expensive or basic but lacking structural elucidation. This led to the use of an existing coarse grain model to determine thermodynamic properties of DNA assembly and testing of this model against experimental datasets. The initial testing of the model and calculation of thermodynamic properties are shown here, along with steps for deployment of the model for understanding novel assays. This is the first time that thermodynamic properties of DNA have been determined from this coarse grain model. Analysis showed that the results were comparable with simulation models shown in the literature, while being generated at much less computational expense.

3.2 Introduction

The initial goal of the work in this chapter was the development of a binding induced DNA assembly (BINDA) assay. This assay has received significant attention in the literature, due to initial reports which highlighted the extreme sensitivities [1] and consistent response available with this assay type. The BINDA relies upon the increased stability of an intramolecular DNA assembly over an intermolecular DNA assembly. This concept is used to design an assay where the presence of a target joins two DNA probes, making the assembly intramolecular. The DNA probe is bound to the protein target via a conjugated recognition molecule, such as an antibody or aptamer. Without the target, the two DNA probes remain separate and have lower stability, as shown in figure 3.1. The top part of figure 3.1 shows the increase in local concentration of DNA after binding. The bottom part of the figure shows the effect on stability of the DNA hybridisation and the corresponding inter- and intramolecular hybridisations. A useful measure of DNA hybridisation stability is the melting temperature, where 50% of strands are hybridised and 50% are separate. If the BINDA is designed properly, the melting temperature of the intramolecular assembly (with target) will be well above room temperature and the intermolecular assembly (without target) will be well below room temperature. Therefore, during a room temperature experiment there will be clear discrimination between the presence of target or not.

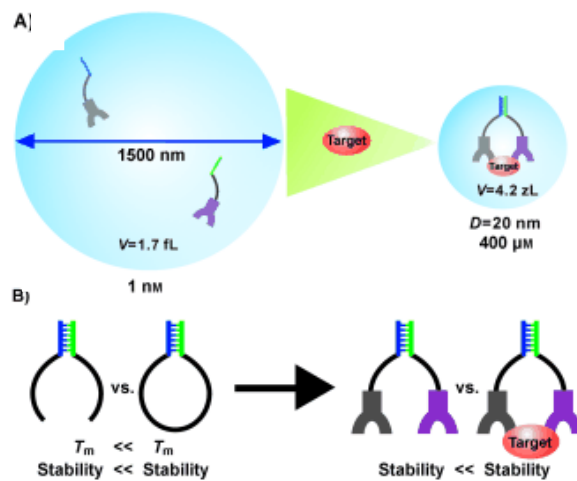


Figure 3.1: Diagram of principles behind the BINDA. The increased local concentration of the DNA strands is shown (top) as is the effect on stability and an analogous intramolecular process (bottom). In this example the target is bound by antibodies but the assay can be based on any binding interaction. Reproduced from reference [2].

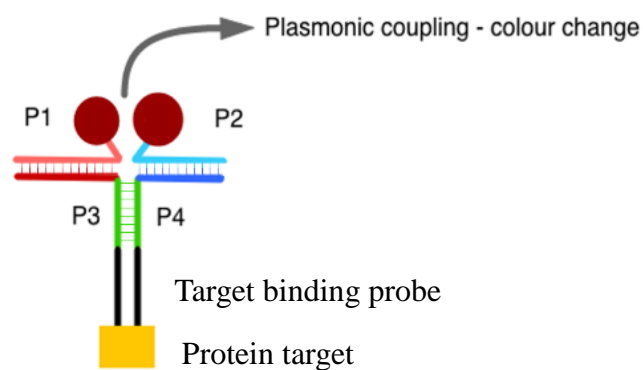


Figure 3.2: Schematic of the initial concept for a BINDA based on plasmonic nanoparticle coupling. The sequences in black are the target binding probe, e.g. an antibody or aptamer. P1 and P2 are the nanoparticle bound DNA sequences for attachment to the BINDA probes. P3 and P4 are the BINDA assembly sequences which should only hybridise in the presence of the protein target (yellow square). The dark red and green sequence marked as P3 are a single continuous strand of DNA, as are the dark blue and green marked as P4. Thin lines between the strands show bonding but do not represent individual base pair interactions in this diagram.

An initial conceptual design for adapting the BINDA to use with nanoparticle coupling is shown in figure 3.2. This assay has been exploited using fluorescence [3, 4], electrochemical methods [5] and DNA amplification [2] but not plasmonic nanoparticle coupling. It is furthermore interesting because it can transform a protein assay into a DNA assembly, allowing the use of a more predictable DNA assembly. The initial motivation for adapting this assay for use with nanoparticle detection was to allow the detection of the proteins using various detection molecules, whilst maintaining a constant assembly process. Detection methods relying on nanoparticles are very susceptible to changes in inter-particle distance [6], meaning that comparison between two different binding molecules for the same target is not possible. Using the BINDA, the constant DNA assembly should allow direct comparison between different binding molecules for the same target. The initial aim of this work was the comparison of aptamers and antibodies against the same target. Brain natriuretic peptide detection was the ultimate goal, with a streptavidin/ biotin system used as a model for developing the assay. The strong binding of biotin and streptavidin make it a good starting point for developing this type of assay. The streptavidin is also multivalent allowing for four biotinylated probes to bind to it. As a development model, biotin and streptavidin are also readily available.

Developing the assay with streptavidin and biotin as the binding pair gave some challenging results. DNA conjugated streptavidin probes, which were designed based on published sequences used for fluorescence detection, appeared not to give any assembly as the full assay did not give any plasmonic changes. Without further understanding of the point of failure it was difficult to redesign the probes. Chemical assays to test for double stranded DNA were not successful at confirming which parts of the BINDA assembled correctly. A computational method was sought that would give better dynamic, structural information on the DNA assembly probes. Computational tools should allow a design-led, rationally planned approach to various BINDA assays, rather than the more typical heuristic, experience driven design.

3.2.1 Simulation of DNA

Multiple simulation types exist, including single point calculations, energy minimisation calculations and molecular dynamics (MD). In static calculations the potential energy of a system is calculated at a single fixed geometry. Energy minimisation expands on this to determine conformations which lower the potential energy for a system and allows a potential energy surface to be created, identifying structures with local energy minima. MD dynamically simulates how a structure changes with time at a given temperature based on inter- or intramolecular forces on the molecule. Since the BINDA assay assembly is a dynamic process and to determine physical values of the process we require dynamic structure, MD is the best candidate for this model.

In all types of simulation, some method is required for determining the potential energy or force. This can be done with *ab-initio* calculations [7, 8], semi-empirical quantum mechanics based models [9] and classical mechanics based molecular mechanics (MM) [10, 11]. Potentially all of these models could provide a useful basis for understanding the BINDA. The key limitations of simulations based on *ab-initio* methods, are the large computational requirements to model these systems. Since the *ab-initio* methods are based only on quantum mechanics; a very large number of calculations must be solved for all electrons in the system. This requires a large amount of calculation time for even relatively limited systems and will be unsuitable for the simulation of DNA sequences with the order of hundreds or thousands of individual atoms. Semi-empirical models reduce this computational requirement by parameterising some features, based on experimental data. This reduces the required calculations but is still relatively expensive for the large DNA structures involved in the BINDA. Molecular mechanics is often the most suitable simulation type for medium to large sized biomolecules. These simulations are based on classical mechanics models, which allow the potential energy of a system to be calculated as a function of its atomic coordinates from classical equations containing some empirical parameters. Enough accuracy is retained in these MM models to be very

applicable for a variety of simulation models including investigation into a variety of DNA properties [12], thermodynamics of protein-ligand interactions [13] and how material properties change with temperature [14]. For studies of thermodynamic properties and simulation structure over long timescales, MD based on a MM forcefield is likely to be the best fit. This model type is the most suitable for modelling of the BINDA. However, over the experimentally relevant timescale, even MM driven MD simulations are likely to become computationally expensive. Further steps to reduce this requirement are outlined later in the chapter.

3.2.2 Molecular Dynamics

Molecular dynamics is a computational method which relies upon the capability of modern computers to perform large numbers of calculations in order to model physical interactions. The strategy of this simulation type is to set initial positions and assign random velocities, based on thermal motion. A simplified theory for the MD process is given below. The forces on every particle in the simulation are calculated based on interactions with all other particles. These new forces are then used to determine the acceleration, from Newton's second law.

$$a = \frac{F}{m}$$

Where a is acceleration, F is force and m is mass. The first and second integrals of this acceleration are taken to calculate the velocity and position. These new positions and velocities are used to determine the motion over some small time step and the new forces used to repeat this process. The whole process is completed many times to build up a series of positions for each atom as outlined in the flow diagram in figure 3.3.

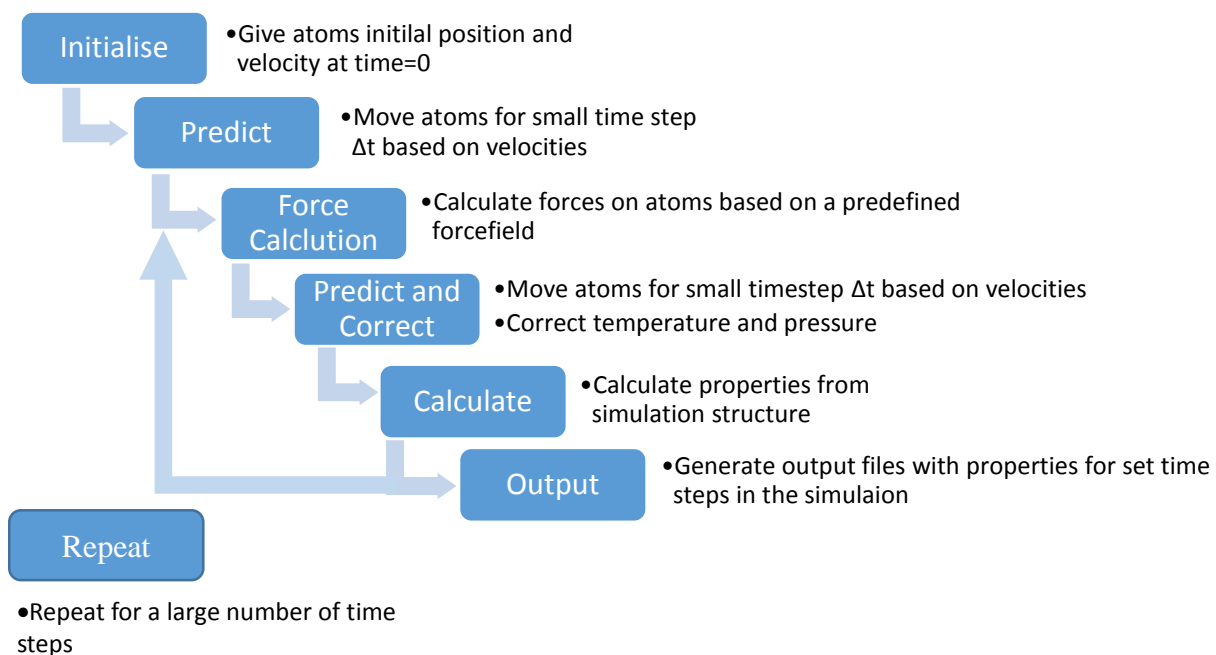


Figure 3.3: Flow diagram showing the steps involved in a basic MD routine which are repeated many times to generate an output which shows atom positions with time.

The force is a key parameter in MD as it defines completely how the positions change. The force is given by a forcefield in the simulation through the second derivative of the potential energy with respect to position. These forcefields can be simple models such as the isotropic Lennard-Jones hard sphere potential [15] or complex models such as reactive forcefields which can model chemical bond breaking and formation [16]. The choice of forcefield is key and must be defined and parameterised such that it well represents the interactions to be studied. Often this practically entails the correct choice of a suitable forcefield from the literature as many fully parameterised forcefields have been developed.

3.2.3 Reducing Computational Requirements of Simulations

To reduce the computational demands of a MD simulation, groups of atoms in the simulation can be replaced with a pseudo-atom (also called a bead) that is parameterised to represent important features of the chemical group it replaces. This

technique is called coarse graining (CG) and eliminates atom-atom interactions along with conformational and configurational degrees of freedom that are unnecessary in determining the parameters or structures of interest [17, 18]. The MD simulation of DNA can be done atomistically, i.e. including every atom in the structure in the simulation. This has been done multiple times in the literature [12, 19, 20] and is very successful in many cases at giving useful prediction. However, the interactions of DNA are dominated by the hydrogen bonding between only four types of nucleobase; adenine, cytosine, guanine and thymine. Rather than define the individual atoms as the smallest unit, for DNA with a finite number of available chemical functional groups, it is sometimes preferable to define the nucleobases as the smallest unit. The phosphate and deoxyribose sugar must also be included to maintain a useful simulation by adding steric information to the model. With an atomistic simulation, all possible interactions between the atoms must be calculated, causing the number of calculations to increase greatly compared to a CG model. The gross number of 2 body interactions in the simulation scales with N^2 , where N is the number of atoms in the simulation. Coarse graining can reduce the number of interactions between two DNA base pairs by up to a factor of 100. This is likely to be an over estimate of the true figure, due to cut-off distances in calculating interactions, but highlights the potential of the technique to reduce computational requirements.

A relatively new model for CG simulation of DNA is the three sites per nucleotide model (3SPN2). In this model, separate beads are used to model each of the nucleobases, the sugar and the phosphate backbone [21]. The extent of coarse graining has some influence on the data generated by the model. Simpler one or two site models can represent energy changes etc but often not complete structural information. More beads increase the structural information but at increased computational cost. 3SPN2 is one of the simplest models which is able to properly represent the major and minor grooves of DNA and the structure of the double helix [22]. 3SPN2 is therefore a suitable model, as the coarse graining does not compromise the structural information from simulation. Each CG bead is modelled by the forcefield in 3SPN2 and the interactions are set by the anisotropic forcefield around

each bead, accounting for the directionality of the interactions. The initial structure is setup by the simulation tools as a straight chain of the double stranded DNA and, from this initial structure, MD simulations can be started.

The basic components of the 3SPN2 interactions can be broken down into bonding and non-bonding terms [21]. The Bonding energy (U_b) contains terms representing the length of bonds between two CG beads (U_{bond}), the bond angle between three bonded CG beads (U_{bend}) and the torsion angle created by four bonded beads (U_{tors}). These are commonly used terms in MD forcefields for chemically bonded species and are parameterised for all possible cases (in 3SPN2, for all combinations of bonded CG beads), so that they give values that represent those from experiment or *ab-initio* calculations.

The non-bonded energy contributions (U_{nb}) are more specific to the DNA modelled in 3SPN2. It comprises a volume exclusion to account for space occupied by the bases (U_{exe}), intra-strand base stacking (U_{bstk}), inter-strand base stacking (U_{cstk}), base pairing interactions (U_{bp}) and electrostatic potential (U_{elec}). Importantly, only beads which are not joined by the bonding terms are paired for the non-bonded interaction.

$$U_b = U_{bond} + U_{bend} + U_{tors}$$

$$U_{nb} = U_{exe} + U_{bstk} + U_{cstk} + U_{bp} + U_{elec}$$

The 3SPN2 model had not been tested widely in the literature for its ability to give thermodynamic properties from simulation. The key information required from the model was the stability of the BINDA probes, either in terms of the melting temperature or the free energy change on binding. Free energy change on binding is the more robust figure and is more widely reported from experimental and computational datasets. Melting temperature is useful as it gives an intuitive feel for the stability and how this will apply to experimental conditions.

To reduce the computational requirements of the MD simulation even further, the solvent can be replaced by a continuum model. Including every solvent model in the

simulation (explicit solvation) is computationally expensive, as it greatly increases the number of interactions to be calculated. This is because in a typical simulation there will be many more solvent atoms than DNA molecules and the solvent will add many potential interactions. Ordinarily, these solvent molecules do not add useful information to the system but there are exceptions, including studies into dissolution of molecules [23]. Replacing explicit solvent molecules with some other representation (implicit solvation) allows the number of atoms in the simulation to be reduced, with minimal reduction in the quality of data obtained. The solvent molecules are most often replaced by a field which replicates some of the effect of the solvent on the molecule. This can be a Langevin model in which the solvent effect is represented by a series of equations giving a field of random drag/ jostling interactions on the solute [24]. Alternative implicit solvation models include the generalised Born surface area (GBSA) [25] or the Poisson-Boltzmann surface area (PBSA) [26]. The PBSA model simulates the molecular electrostatics in a solvent by replacing the molecules with a dielectric continuum. GBSA simplifies this further by replacing the solute with spheres that have different dielectric properties from the solvent. In both methods the surface area (SA) contribution simulates the non-polar contribution to solvation by calculating an effective area for van der Waals interaction between the solvent and molecule.

The reduction of computational requirements, both in terms of computing time and total size of the simulation, by combining this implicit solvent with coarse graining can be substantial. To take advantage of this, Langevin dynamics was used in the simulations in this work. Comparison is made to GBSA and PBSA models in the literature.

3.2.4 Determining Free Energy Change from Non-Equilibrium Simulations

To determine the free energy taken to dehybridise the double stranded DNA, the Jarzynski equality can be employed [27]. This equality relates the work done in a finite number of experiments or simulations and the free energy for the process. The

equality has been applied over a large number of both simulated [28, 29] and experimental systems [30, 31].

To determine the work done and therefore apply the Jarzynski equality, a steered molecular dynamics simulation (SMD) can be used. In this simulation model a dummy atom is used to apply force to some part of the simulation as shown in figure 3.4. For the double stranded DNA, this force can be applied to dehybridise the DNA in the simulation. The dummy atom in the DNA model moves at a constant velocity and is attached to a stiff spring.

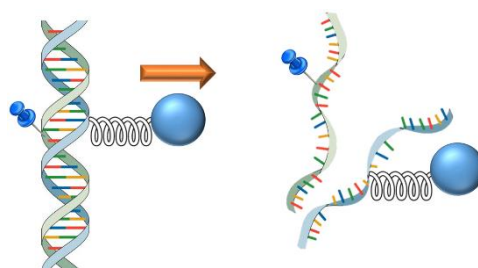


Figure 3.4: Diagram of the SMD process used. One strand is pinned to a fixed point. The other strand is attached to a moving dummy atom (blue sphere) via a spring (left). As the dummy atom moves it imparts a force on the DNA. Eventually this will result in dehybridisation (right).

Since the harmonic potential of the spring is a defined parameter, the distance between the DNA strand and the dummy atom will allow the applied force to be calculated. The work done is then calculated by the simple equation

$$W = Fd$$

Where W is the work done, F is the force and d is the displacement of the dummy atom.

The Jarzynski equality in three possible forms is given below [28]. Firstly, the original form of the equality.

$$e^{-\Delta F/kT} = \langle e^{-W/kT} \rangle$$

Rearranging to explicitly give the free energy change:

$$\Delta F = -kT \times \log \langle e^{-W/kT} \rangle$$

And after a cumulants expansion up to the second term

$$\Delta F = \langle W \rangle - \frac{1}{2T} (\langle W^2 \rangle - \langle W \rangle^2)$$

Where in all cases ΔF is the free energy change, k is the Boltzmann constant, T is the temperature, W is the work done and the angled brackets indicate an average of multiple independent experiments.

The simplest form is the first term cumulants expansion, which is an average of the work done over a number of simulations. The second order cumulants expansion corrects this by adding a difference of squares and is recognised as the most accurate [28]. The second order cumulants expansion was used in this work. These simple calculations allow the prediction of equilibrium properties of the DNA dehybridisation, from a non-equilibrium simulation.

3.2.5 Statistical Analysis

Several parameters can be used to check the validity and predictive power of the model obtained from the 3SPN2 model. These are used in literature for comparing simulated and experimental datasets [32]. In this chapter these statistical measures are used to check how well predictions from a simulation model compared with experimental results, over a number of oligonucleotide sequences.

The coefficient of determination (R^2) is routinely used in describing how well recorded values are predicted by a model. An R^2 value of one means that a model completely describes observed values, whilst a value of 0 means that none of the variation in the observed variable is described by a model. R^2 is not the only parameter in determining

how well a model fits observed data and care should be taken not to assume a high coefficient of determination indicates that a model is the correct one.

$$R^2 = \left(\frac{\sum_1^i (x_i - \bar{x})(y_i - \bar{y})}{\sqrt{\sum_1^i (x_i - \bar{x})^2 \sum_1^i (y_i - \bar{y})^2}} \right)^2$$

Where y_i is the known experimental result, \bar{y} is the mean of all y values, x_i is the result from the model and \bar{x} is the mean of all x values. The Σ represents a summation which is performed over all pairs of x and y values.

Root mean square error (RMSE) is complementary to R^2 and gives an absolute measure of how far the data points lie from their predicted values. RMSE is a key value for the model if the regression is to be used to predict values. A low RMSE indicates that the predicted values are very close to the true values and the model will give useful predictions. Conversely, a high RMSE suggests that the model poorly describes the data and the predictive power of the model will be weak. It is composed of the bias and standard deviation, meaning for an unbiased model the RMSE will equal the standard deviation.

$$RMSE = \sqrt{\frac{1}{N} \sum_1^i (x_i - y_i)^2} = \sqrt{bias^2 + \sigma^2}$$

Where x_i is the predicted value from the model, y_i is the experimental y value and N is the total number of correlated points. The Σ represents a summation which is performed over all data points.

The bias describes any systematic error in how the regression model predicts the data. A positive value indicates that the model tends to over-predict (return a more positive value), while for a negative value the model generally under-predicts (return a more negative value). A value of 0 indicates that the model is unbiased but not that it well represents the data. Bias is an absolute measure and is relatively simply

corrected by adding a correction constant to the regression model.

$$bias = \frac{1}{N} \sum_1^i (x_i - y_i)$$

Where x_i is the predicted value from the model, y_i is the experimental y value and N is the total number of points. The Σ represents a summation which is performed over all data points.

Standard deviation (σ) describes how much of the total variation in the model cannot be accounted for by a systematic bias in the model. In the total error it accounts for random error that cannot be corrected in the model. High standard deviation indicates that the regression does not correctly predict the data due to some reason other than systematic over- or underprediction.

$$\sigma = \sqrt{\frac{1}{N} \sum_i^i [x_i - y_i - bias]^2}$$

Where x_i is the predicted value from the model, y_i is the experimental y value and N is the total number of points. The Σ represents a summation which is performed over all data points.

Taken together these basic statistical measures report how well a model made from simulated data represents the true values from experiment. They also indicate the total error in the model, how much of the error is from a bias in the estimation and how much error is contributed from uncontrolled variation in the model.

3.3 Aims

To further understand the BINDA, the 3SPN2 model was to be developed as a tool for understanding the assay on a molecular level and why the initially designed probes had failed. To do this the CG MD model was to be checked for its predictive power and how well it matched results from experiments in literature. The simulation tool was also to be set up for the modelling of the BINDA.

3.4 Results and Discussion

Initially the parameters of the simulation including values for the simulation time, SMD spring constant and velocity were tested to determine suitable input values for the DNA hybridisation to be carried out. This was performed iteratively (starting from reasonable conditions from literature [28]) using a 20 base pair model until a reasonable set of values was obtained. The parametrisation of the SMD setup was not investigated further. The combination of simulation time, spring constant for the SMD and the dummy atom constant velocity arrived at was 10 μ s, 7.8 kcal/ mol \AA^2 and 0.000001 $\text{\AA}/$ fs, for a 20 base pair dehybridisation. The velocity and spring constant could be kept constant and the simulation time altered, if required, for simulations. Initial SMD experiments were held at the centre of mass (COM) of one strand and pulled at the COM of the complementary strand.

The model was tested by checking how many simulations were required so that the final free energy values generated converged and were stable. To do this, the same simulation was run 999 times and set numbers of simulations sampled. The average free energy from the sampled simulations was calculated and plotted against the number sampled. This was done without replacement so individual simulations could not be processed in a calculation more than once. Results from a robust calculation should not vary with the number of simulations sampled.

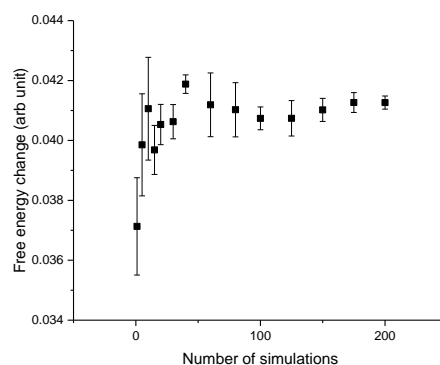


Figure 3.5: Convergence of free energy change from sampling an increasing number of simulations. All simulations are run using the same inputs and DNA sequence. The number of replicates contributing to each point is shown on the x-axis. Sampling was repeated three times to give error bars of one standard deviation.

The variation between sequential sample sizes was initially very large and decreased as the number of simulations increased as shown by the graphed results in figure 3.5. The standard deviation also decreased as the number of simulations increased, as expected through the result becoming more robust and closer representing the true mean of the whole population.

The number of simulations required to reach a stable result was relatively large at around 200. This relatively large sample number indicated a good level of variation between simulation runs, caused by the varying initial conditions. Reasonable variation is useful as it means a larger number of physical structures and dehybridisation pathways are being sampled by the model, likely giving a better representation of reality at the cost of increased computing time.

The second check run was to determine whether the results from simulations reliably scaled with increasing number of base pairs. To test this, a 10 base pair sequence was randomly selected from a longer sequence. This 10 base pair sequence was repeated a number of times to give sequences of various lengths. As can be seen in figure 3.6, the linearity of the increasing number of base pairs was good. In these simulations only 200 repeats were run in each simulation so bootstrapping error analysis was

used. In bootstrapping analysis, 200 samples were picked with replacement and the free energy change calculated. This was repeated 300 times with random sampling each time. Since replacement is allowed, each simulation can be selected more than once and each result is slightly different based on the samples selected. The results from the 300 repeats of the processing were averaged and the standard deviation estimated. Compared to sampling without replacement from a larger pool of simulations, bootstrap analysis appeared to underestimate the standard deviation.

The standard deviation values in figure 3.6 appear very small, compared to those for 200 simulations in figure 3.5. The coefficient of variance calculated by sampling with replacement varied between 25-50% of that calculated when a pool of 999 simulations was randomly sampled.

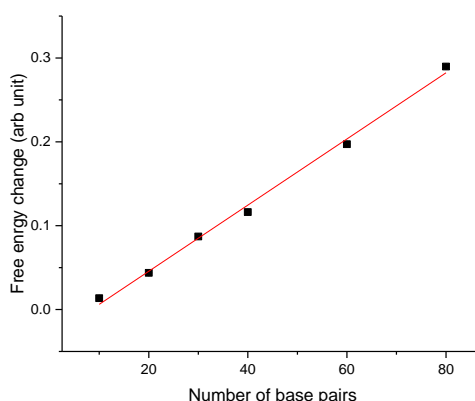


Figure 3.6: Free energy change with increasing number of DNA base pairs dehybridising. Results are an average of 200 replicates. Error bars are not visible, due to the y-axis scale.

One additional feature of these simulations was an observed increase in the free energy, even after the DNA was dehybridised. This followed a constant gradient after a clear change in line shape. All simulations were run for 50 μ s, to accommodate the increased time to dehybridise the relatively large 80 base pair DNA. The constant

gradient change in the free energy represented a large fraction of the overall free energy change. This was particularly noticeable for the shorter sequences which dehybridised more quickly, leaving more time for this second contribution to the free energy change to accumulate. The example shown below in figure 3.7 is for 20 base pairs and clearly shows the initial dehybridisation event as a steep gradient, for approximately the first 3 μ s of the simulation, followed by a constant rate of increase for the rest of the simulation time. Figure 3.8 shows the corresponding force profile with movement of the dummy atom. Initially there is a peak in the force value, as the DNA dehybridises. The force then returns to near zero and fluctuates around zero for the remaining simulation time. No second force peak is observed to account for the second stage free energy increase.

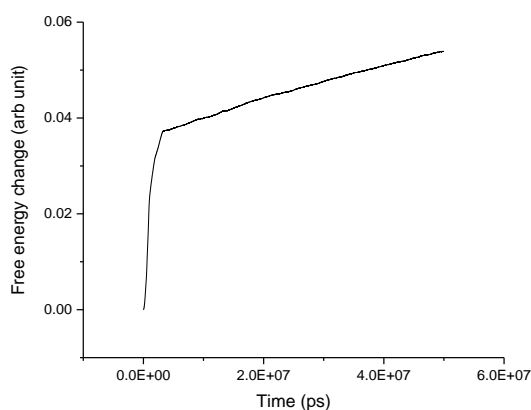


Figure 3.7: Example of free energy change with time showing the two distinct profiles. The sharp initial increase of free energy with time to approximately 5×10^6 ps represents the dehybridisation event. The result is from a single representative simulation.

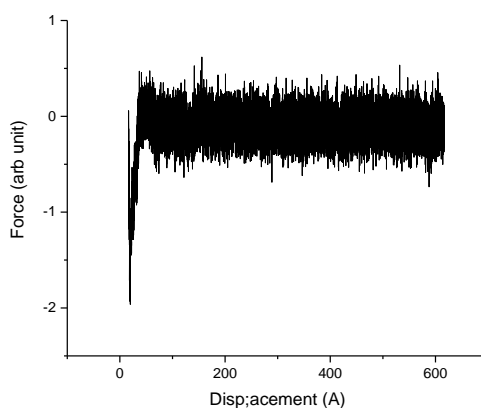


Figure 3.8: Example of force with displacement of the SMD dummy atom, showing the dehybridisation as a sharp negative peak in the force at slightly greater than 0 Å. The result is from a single representative simulation.

This gradient was observed in all simulations and in some cases was preceded by a short section where no increase was observed. To remove this extra contribution to the free energy change, the data in figure 3.6 was taken from points in the simulation at the end of the dehybridisation event. This point in the simulation was then randomly sampled 300 times with replacement, to give the average values and standard deviation presented in figure 3.6. Since the end of the dehybridisation was sometimes indicated by a point of zero gradient, a script was used to automatically select this point but this worked in only a limited number of simulations and more often the point to be sampled had to be selected manually. This was due to inconsistency in the change in gradient after dehybridisation. In some cases, there was no plateau and running the script to determine the point of minimum gradient did not work.

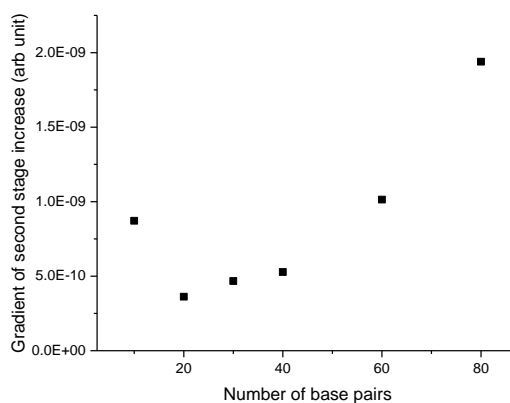


Figure 3.9: Gradient of the energy increase after dehybridisation with increasing base pairs. Results are the average of 200 simulations. Error bars are not visible, due to the y-axis scale.

Figure 3.9 shows the gradient of the increase in free energy after dehybridisation. This increased with increasing number of base pairs, with the 10 base pair simulation as an outlier, and appeared to approximately follow an exponential trend. Further investigation into this is detailed below.

3.4.1 Changing the Pulled Group in SMD

To check the influence of the point pulled by the dummy atom in the SMD simulations, the same simulations as in the above section were repeated with the SMD groups redefined. In the experiments above, the DNA was pulled from the COM of the single strand of pulled DNA. This COM was recalculated as the simulation proceeded. As a further investigation, force was applied to either the terminal phosphate bead or the centre phosphate bead in the pulled strand. The stationary strand was still held at its COM. The sampling methodology was the same as for the investigation into changing the number of hybridising base pairs.

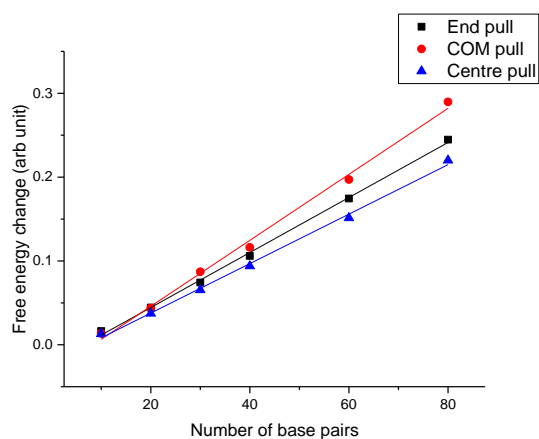


Figure 3.10: Free energy change of dehybridisation with increasing numbers of base pairs for the end phosphate pulled by the SMD (black), the COM pulled by the SMD (red) and the centre phosphate pulled by the SMD (blue). Lines of best fit to the data are shown in the same colours. Results are the average of 200 simulations. Error bars are not visible, due to the y-axis scale.

Table 3.1: Parameters from the lines of best fit shown in figure 3.10.

Pulling point	Gradient	Intercept	R ²
COM	0.0039	-0.033	0.996
End phosphate	0.0033	-0.021	0.998
Centre phosphate	0.0030	-0.021	0.997

The linear correlation between the number of DNA base pairs being dehybridised and the free energy change was strong in all cases but showed different gradients and intercepts for each of the cases as shown in figure 3.10 with the regression values detailed in table 3.1. Visual analysis showed a different dehybridisation pattern with the centre phosphate pull compared to a COM pull and the end pull. The end phosphate pull and COM pull dehybridised the DNA from one end to the other while the centre phosphate group dehybridised the strands from the centre. Applying the

SMD force to the centre of mass created a complex progression of dehybridisation. This was due to the COM shifting as the structure changed shape, therefore changing the direction of force. Images from the simulations show how each of these pulling modes contributes to a different dehybridisation mode.

Figure 3.11 shows the COM pull causing an unzipping of the two strands, accompanied by significant bending of the DNA into a horseshoe shape around one COM. Figure 3.12 shows the end pull and associated unzipping dehybridisation, again with significant bending of the strands around the pinned COM. Figure 3.13 shows the different structure adopted when pulled from the centre phosphate. The entire double strand flexed into a hairpin bend before the centre bases began to dehybridise, forming a large open loop.

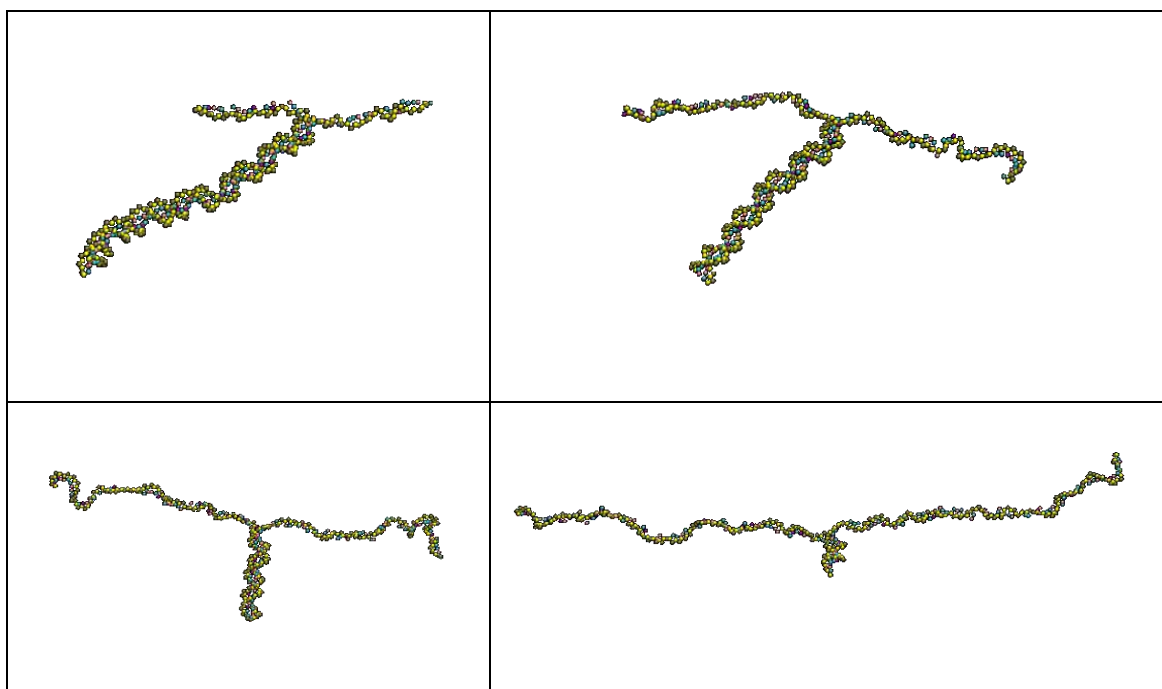


Figure 3.11: Images showing how the dehybridisation of 80 base pair sequence proceeds (from top left to bottom right) when pulled from the centre of mass, with 2 μ s between each image.

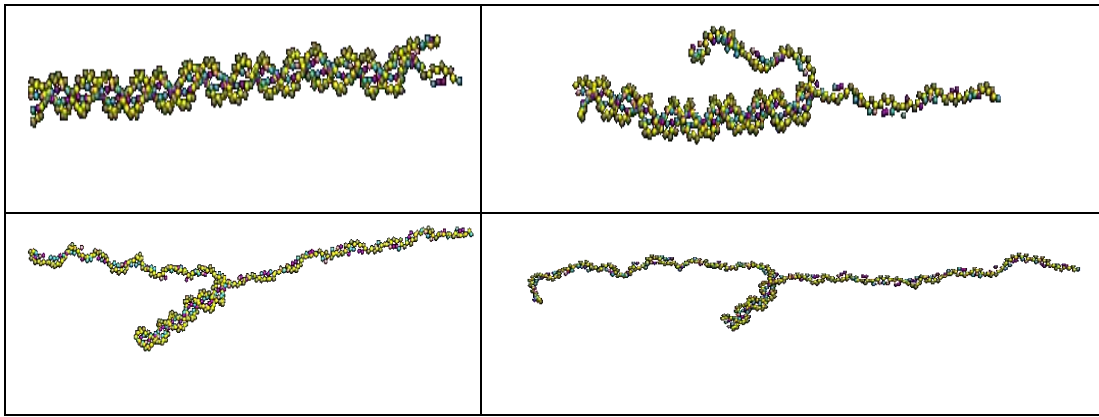


Figure 3.12: Images showing how the dehybridisation of 80 base pair sequence proceeds (from top left to bottom right) when pulled from the end phosphate, with 2 μ s between each image.

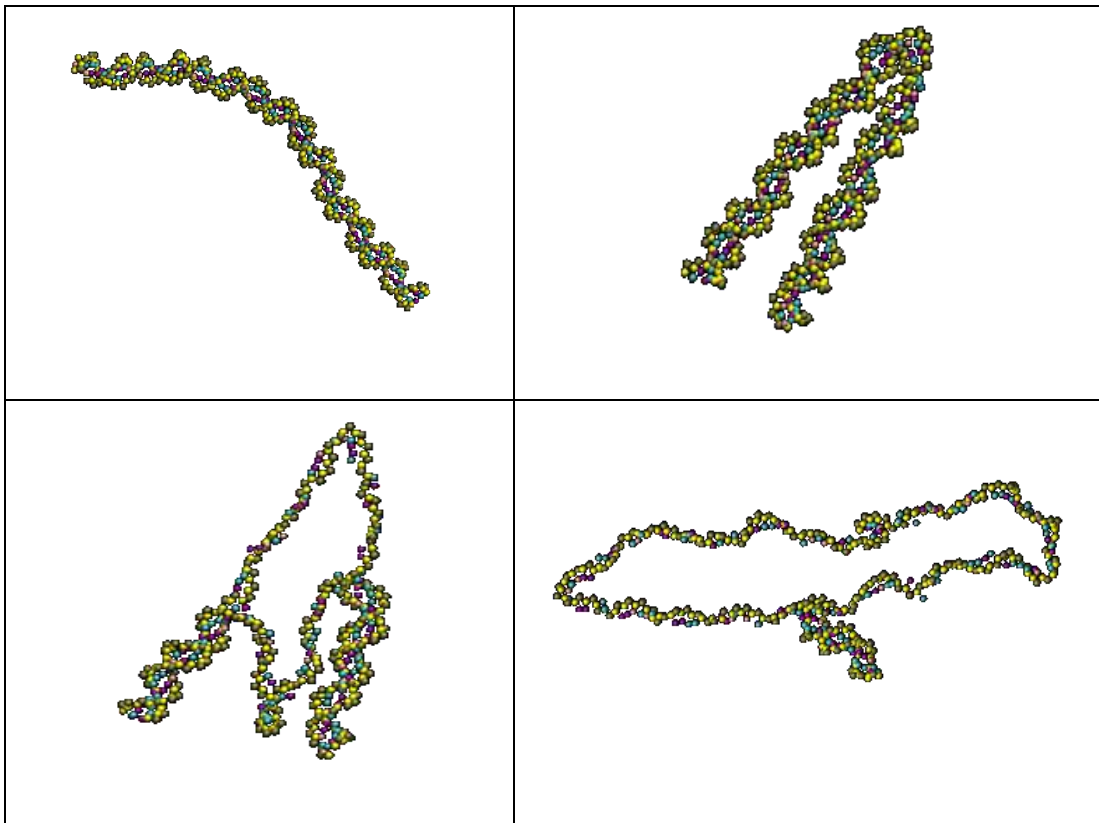


Figure 3.13: Images showing how the dehybridisation of 80 base pair sequence proceeds (from top left to bottom right) when pulled from the centre phosphate, with 2 μ s between each image.

It has been shown previously from simulation that the different dehybridisation modes result in different free energy changes [33]. It is likely to be this effect that

causes the differences in linear trend for different pulling modes. The centre phosphate pull is likely to give the closest to pure unzipping with COM and end phosphate pulling giving mixed unzipping and shearing modes [33].

The second stage gradient after the dehybridisation event had occurred was still evident, and appeared to be influenced by the number of base pairs being dehybridised as shown in figure 3.14.

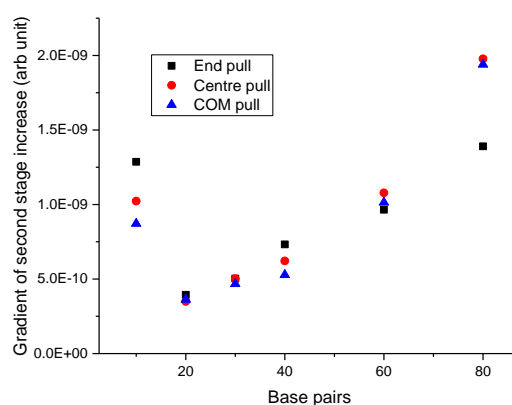


Figure 3.14: Gradient of second stage free energy increase with increasing base pairs in the simulation for end phosphate pulled by the SMD (black), COM pulled by the SMD (blue) and centre phosphate pulled by the SMD (red). Results are the average of 200 simulations. Error bars are not visible, due to the y-axis scale.

For all pulling modes the gradient observed for the 10 base pair simulation was anomalously high. Excluding 10 base pair simulations, the remaining values showed a continuous increase with a difference between the end phosphate pull and the other two modes. This suggested that the physical orientation of the DNA has some influence on the rate of energy increase with time. The most likely interaction causing this is with the Langevin field representing the solvent, as this is the only remaining interaction with the DNA after dehybridisation. Performing a limited number of simulations at different pulling velocities indicated a linear trend (figure 3.15) but this would require further investigation to confirm. A further investigation could use a different implicit solvent or explicit solvent to determine whether this effect was

consistently represented across the different solvation models

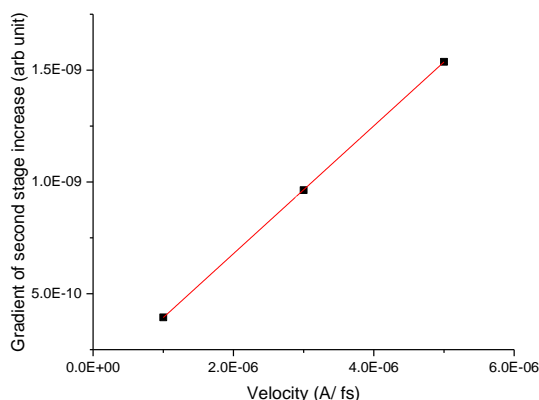


Figure 3.15: Gradient of the second stage free energy increase with increasing SMD dummy atom velocity. Results are the average of 200 simulations. Error bars are not visible, due to the y-axis scale.

The dependence on length of DNA and pulling speed indicated a contribution to total work done on the system by solvent drag. One previous paper reported frictional forces in similar SMD simulations, where after an unbinding event a molecule was moved through simulated solvent [34]. The literature source detailed two proteins being uncomplexed with different pulling points for the SMD, with the different forces observed attributed to changing surface area for the interaction with the solvent. In the case of DNA, the surface area will be related to the length of the DNA strand and the geometry of the strand as it moves through the solvent. Friction with the solvent in the system appears to explain the free energy contribution in this case. It is not clear why 10 base pairs gave higher than expected values for all simulations.

3.4.2 Comparison with Experimental Data

After the inherent scalability, reproducibility and linearity of the model with increasing numbers of base pairs had been established, the predictive power of the 3SPN2 model was checked. Numerical results from the simulations would not be expected to directly match true values from experiment or from atomistic

simulations, due to the reduced nature of the interactions in the coarse-grained model. However, the 3SPN2 model would be expected to predict general trends correctly, which is often sufficient to guide experimental work. Moreover, with a correction factor, determined through comparison of simulated and true values, the final output of the simulation model can be calibrated to match experimental values. Literature details numerous reports of the free energy change on DNA hybridisation and a comparison of these with various simulation models. The 3SPN2 model was compared with the most comprehensive of these literature reports [32]. The published work details 305 DNA sequences with exact complementary sequences. None of the simulations involved more complex structures, such as overlaps or mismatches. Multiple solvation models were used and the free energy change, entropy and enthalpy change was calculated for each sequence and then compared to experimental data. Due to a cut-off term in the 3SPN2 setup, only sequences longer than 8 base pairs could be modelled without modifying the setup. 79 remaining sequences of 9 base pairs or more were simulated to determine the dehybridisation energy. The simulation of all of these sequences was completely automated by the use of purpose-written R and Bash scripts. The end point of the dehybridisation was determined by taking the point of minimum gradient using a computer script, which was successful in these simulations.

The literature source also details several MD simulations results for the free energy change of dehybridising DNA and one mathematical model for predicting this value (nearest neighbour model). The nearest neighbour (NN) model is based on the energetic contribution of a base pairing interaction weighted by the base pairs next to it. This mathematical model is calibrated over many DNA sequences, so is a good representation of the average free energy change for a hybridising base pair. It is entirely empirical. It is useful because it is very rapid and gives a good representation of experimental data, for simple double stranded DNA. It does not, however, give any structural information nor any useful data for mismatched sequences or overlap in one sequence. The simulation models reported are all atomistic DNA models with various solvation systems including the PBSA and GBSA models with explicit solvation

shells added (PBSA + shell and GBSA +shell) and the GBSA implicit solvent model only.

Literature values for free energy change were calculated by taking the total potential energy in the simulation after hybridisation and before. The difference was attributed to hybridisation, as constant pressure was maintained and the volume change was negligible. From this enthalpy change, free energy and entropy changes were also calculated.

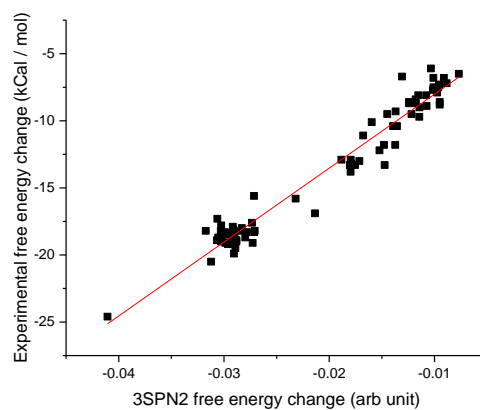


Figure 3.16: Free energy change for all sequences in the experimental dataset compared to the result from 3SPN2 simulation. Red line shows line of best fit for all data points. 3SPN2 energy changes are the average of 200 simulations. Error bars not shown.

Table 3.2: R² values for linear regression between experimental free energy values and values from each of the models tested, for the full dataset.

Model	R ² value
3SPN2	0.96
Nearest Neighbour	0.99
PBSA +shell	0.94
GBSA + shell	0.93
GBSA	0.96

The unprocessed results (figure 3.16) showed a relatively good linear trend but the distribution of the dehybridisation energies is biased towards a group at between -18 and -20 kcal/ mol and by a lack of data between -15 and -18 kcal/ mol, potentially influencing the model. This is observed with all other models and is due to the relatively similar families of sequences that make up the dataset. The R² value of the 3SPN2 model is comparable to the other models, with all showing a good linear correlation as indicated in table 3.2. The nearest neighbour (NN) model gives the best linear correlation of all the models, with implicit solvent and 3SPN2 being slightly lower than this. The two models with explicit solvent added showed less good linearity. The relatively high R² indicates that the 3SPN2 model can correctly predict trends in the underlying data of the oligonucleotide dehybridisation. This is important as a relative measure of thermodynamic properties is often very useful for comparison.

The direct results from the 3SPN2 simulation showed good linear correlation with the experimental data, however, the data was not useful for quantitative predictions at this stage. This was because the raw 3SPN2 results were in arbitrary units due to the

coarse grain model. For this reason, 53 oligonucleotide sequences were randomly selected to form a training set. Linear regression was then carried out on these simulation results to give the regression equation shown below. This equation was then used to make predictions about the free energy of the remaining 26 sequences (test set) in kcal/ mol and these predictions were checked against the experimental values.

$$y = (545 \pm 17)x - (2.65 \pm 0.39)$$

This equation was used to predict the correct value for the free energy change from the simulation results for the training set (figure 3.17). The training set maintains a good linear correlation between the experimental and simulated data, with no significant outliers.

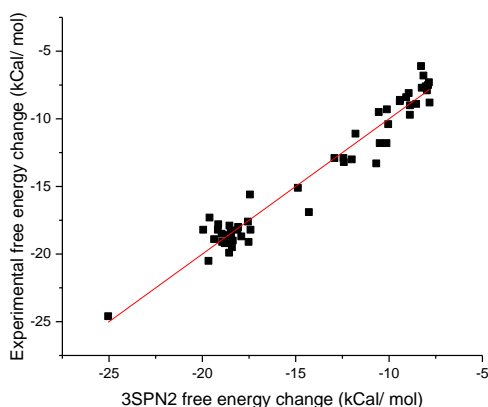


Figure 3.17: Experimental free energy with the 3SPN2 values, corrected using the regression equation given in table 3.3, for the training set. Red line shows line of best fit for all data points. 3SPN2 energy changes are the average of 200 simulations. Error bars not shown.

The effectiveness of the model is given by several statistical analyses as described in the introduction to this chapter. These statistics describe how well the model (based on simulated data) represents the experimental data. As a first test the regression model and statistical analysis can be used on the training set to ensure the selected

data is well represented by the regression model.

Table 3.3: Statistical measures for the comparison between experimental data and each of the models for the training set. 3SPN2 model corrected by a regression model.

Simulation model	R ²	Standard deviation	Bias	RMSE
3SPN2	0.95	1.05	0	1.05
NN	0.99	0.58	0.09	0.59
PBSA + shell	0.93	1.53	0.30	1.56
GBSA + shell	0.91	1.64	-4.45	4.74
GBSA	0.95	1.11	-3.35	3.53

For all models the R² value was above 0.9, indicating that the linear correlation of the models was maintained when the training set was separated. The NN gave the strongest linear correlation, followed by 3SPN2 and the GBSA solvent model. The weakest linear correlation was given by the models with the added solvation shells. However, all R² values were above 0.9, meaning that the simulation models all described a large proportion of the variance in the experimental results.

Standard deviation values were split into three groups. The highest standard deviation was generated by the models with the explicit solvent shell published in the dataset. The GBSA and 3SPN2 models had lower standard deviation. The lowest standard deviation was observed with the NN model. This matches with the R² values calculated, as the higher standard deviation indicates that there is variation within the experimental results that is not accounted for in the linear regression model.

The second component of the overall error in the regression model is the bias. The

3SPN2 model showed no bias, as expected for results from using the regression model on the training set. As a regression model was not used on the values published in literature, these all have non-zero bias. The NN model maintained a low bias despite not being trained with a regression. The PBSA with solvent shell had a moderate bias towards over-prediction. Both models based on the GBSA had a large under-prediction bias.

The unbiased estimation for the 3SPN2 simulation meant that the RMSE was equal to the standard deviation. The NN model had the lowest RMSE which was contributed to mostly by the standard deviation. The PBSA based model had standard deviation similar to the 3SPN2 model which was again mostly from the standard deviation. Due to the high biases in both the GBSA based models, the associated RMSE was very high.

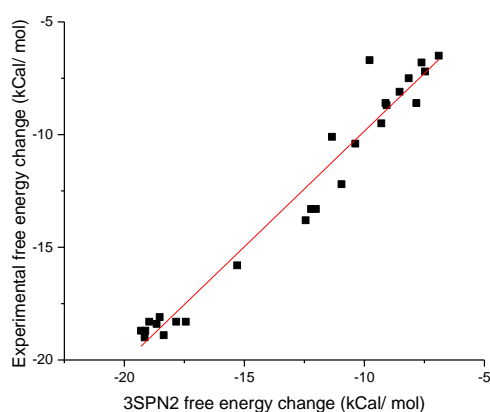


Figure 3.18: Experimental free energy with the 3SPN2 values for the test set. Values corrected using the regression equation given in table 3.3. Red line shows line of best fit for all data points. 3SPN2 energy changes are the average of 200 simulations. Error bars not shown.

With the predictive power of the models benchmarked using the training set, they could then be used to predict values for the test set. The test set was completely separate from the training and none of the sequences used to form the regression model for 3SPN2 are in the test set. It acts as a good test of the ability of the models to predict unknown experimental data. The graph of experimental free energy change versus the predicted value from 3SPN2 is shown in figure 3.18. Visually, the predicted

values appear to correlate well with the experimental result. Statistical analysis of this is given below in table 3.4.

Table 3.4: Statistical measures for the comparison between experimental data and each of the models for the test set.

Simulation model	R ²	Standard deviation	Bias	RMSE
3SPN2	0.96	0.92	-0.08	0.93
NN	0.99	0.57	0.08	0.58
PBSA + shell	0.95	1.33	0.02	1.33
GBSA + shell	0.97	1.07	-4.39	4.52
GBSA	0.97	0.94	-3.27	3.40

For all models, the R² value was relatively high and increased slightly over that from the training and full dataset analysis. This change was small but probably resulted from the lower number of data points centred around the -17 to -20 kcal/ mol area. As these points appeared to be clustered around a central value and not linearly distributed, they are likely to decrease the R² value when included. Again, all R² values were above 0.9, meaning that the models all described a large proportion of the variance in the experimental results.

Standard deviation values showed the same split as for the training set. For the test set, the NN again gave the lowest standard deviation with all other models giving relatively similar values. The models with explicit solvation shells added gave the highest standard deviation.

Against the test set the 3SPN2 model now gives a bias, as expected when moving from training to testing. However, this value is low and is comparable with the bias from the PBSA based model and the NN model. Again the models based on GBSA tended

to give very large under-predictions.

For all models except those based on the GBSA, the RMSE was contributed to mostly be the standard deviation, indicating no systematic error in the model. RMSE for the GBSA based models was again very high due to the large bias. The RMSEs for all models were similar for the test set and the training set, indicating robust predictive models that well represent the data. The regression model used for the 3SPN2 calibration does not appear to add any error to the prediction of experimental free energies beyond the error inherent in the simulation itself. The lower RMSE for the test set was driven by a drop in standard deviation, probably due to the reduction in non-linear data clustered at the more negative free energy changes.

Table 3.5: Linear regression model equations used to correct all of the simulation results.

Simulation model	Regression equation from training set
3SPN2	$y = (545 \pm 17)x - (2.65 \pm 0.39)$
Nearest Neighbour	$y = (0.98 \pm 0.02)x - 0.38 \pm 0.24$
PBSA + shell	$y = (1.22 \pm 0.05)x + (2.71 \pm 0.67)$
GBSA + shell	$y = (0.86 \pm 0.04)x + (1.80 \pm 0.73)$
GBSA	$y = (0.92 \pm 0.03)x + (1.96 \pm 0.51)$

As the 3SPN2 model had to be calibrated by performing a regression using the training set, this regression was also carried out for the other simulation models. This should give an estimation of how the 3SPN2 model compares to these other simulation types when calibrated against the same experimental data. The regression equations shown in table 3.5 were formed from the training set and used to correct the published model data for the test set. These new predictions were then tested against the experimental data.

Table 3.6: Statistical measures for the comparison between experimental data and

each of the models corrected by regression for the test set.

Simulation model	R ²	Standard deviation	Bias	RMSE
3SPN2	0.96	0.92	-0.08	0.93
NN	0.99	0.57	-0.03	0.57
PBSA + shell	0.95	1.02	-0.06	1.03
GBSA + shell	0.97	0.87	-0.03	0.87
GBSA	0.97	0.87	-0.03	0.87

For the test set, whether a regression was used or not the R² value remained the same, indicating the regression models do not influence the inherent linearity of the simulated data as shown in table 3.6.

The most significant effect of using a linear regression to retrain the model is on the bias. The regression should bring the bias close to zero, if it well represents the dataset. For the test set, all models tended to give a very slight under prediction. This was slightly higher for the 3SPN2 model but in all cases was between 3- 8% of the standard deviation, indicating that it was not a major contributor to error in the model. The bias in the GBSA models was reduced by a factor of 100.

By retraining the predictive models, the standard deviation for the PBSA and GBSA based models was slightly reduced. Overall, the standard deviation values remained similar but the GBSA based models now had lower values than the 3SPN2 model.

Due to the great decrease in the bias of the GBSA models when corrected by the regression model, the RMSE for these models was decreased. The predictive powers of these models was therefore increased. For the other models which were less influenced by the bias, RMSE remained very similar.

The NN model always gave the best correlation to the dataset for the simple DNA duplexes. This was probably due to the fact that the empirical nature of the NN model

gave it the closest representation of these simple duplexes, which would be similar to the training data for the original model. Significantly, the NN model can make no prediction on the dynamics of the dehybridisation process or intermediate structures in the process. It also contains no correction terms for the inclusion of mismatched pairs and overhanging or unequal DNA strands. This means the accuracy of the mathematical predictions of the thermodynamic properties of the complex BINDA, the ultimate aim of the simulation, are likely to be compromised.

The 3SPN2 model gave results that predicted the experimental results comparably well with other simulation models. This confirms that the thermodynamic properties estimated from 3SPN2 are likely to give useful information for the BINDA whilst maintaining the advantage of reduced computational requirements. The PBSA model was comparable to the 3SPN2 simulation in all tests but tended to have slightly higher standard deviation values. When using the GBSA based models without correction, the large bias made their predictive power much less than the 3SPN2 model. After performing linear regression with the training set, the predicted values were much closer to the experimental and the RMSE for the GBSA based models was slightly lower than for the 3SPN2. It is not clear why the bias was so high from the published simulated values.

3.4.3 Applying the 3SPN2 Model to the BINDA Assay

In order to apply the 3SPN2 model to the BINDA model, it was necessary to include both the attachment to the target of choice and to include some effect of the attached nanoparticles as shown in figure 3.19. The target was implicitly included, as it was not facile to include a representation of the protein surface in the simulation along with the 3SPN2 model. The key influence of the protein is to hold the end points of the probes at a set distance apart. The space between binding sites on a protein could be determined using the crystallographic structure from the protein databank. Fixing the coarse grain beads of the end base pairs of the probes acted as a good representation of the steric function of the protein. Nanoparticles were also implicitly included, as

the complexity of including material properties was not warranted at this stage. The mobility effect of the nanoparticles was included by adding a weight to the base which was attached to the nanoparticle. This did not include the space occupying effect of the nanoparticle (which was likely to be substantial) but did allow a better representation of the motion of the nanoparticle bound sequences.

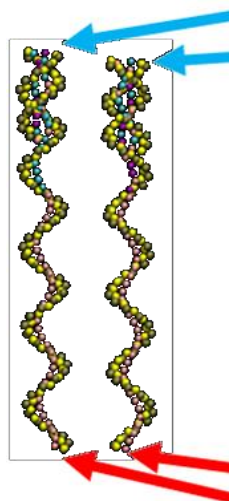


Figure 3.19: Diagram of the BINDA assay model with nanoparticle weight attachments shown by the blue arrows and fixed points simulating the protein shown by red arrows. For comparison with figure 3.1 and 3.2, the red arrows indicate where the binding molecule (antibody or aptamer) would be conjugated to the DNA. This then fixes the DNA to the protein target via these points.

With these modifications the 3SPN2 model was capable of readily making an approximation of the free energy of dehybridisation of the BINDA. One limitation of this set up was the fact that, due to the way the two separate probes were put together, the assembly region of the probes was not hybridised. Under random thermal motion, it was relatively unlikely that the probes would spontaneously hybridise over the short time span in a typical MD simulation. An alternative to the unreasonably long simulation required for the assembled BINDA probe was to use the simulation constraints to apply external work, forming the proposed structure and then allow this structure to equilibrate. This could be done by using SMD to move the two assembly sequences together. Once the BINDA was assembled, the external force

could be removed and another simulation run, using the assembled SMD structure as a starting point. This was allowed to equilibrate under thermal motion for 10 μ s and the result of this simulation could then be used to determine the free energy of dehybridisation of the BINDA assembly section. Only the initial assembly and equilibration steps have been performed thus far and consideration is given to the next steps in this development process in the further work section.

The method of assembling and equilibrating the DNA structure gave a variety of starting structures for the BINDA probes, as shown in figure 3.20. Preliminary results from visual analysis indicated that the position of the nanoparticle attachment sequences and BINDA assembly sequence was not optimal. Within the DNA probes there was no separation between these two parts. The visual analysis indicated that sterically it was not possible for the probes to hybridise into these two separate double stranded sequences within such a confined space. This resulted in the uppermost bases of the assembly sequence being forced apart and reducing their ability to interact. Since the number of base pairs in the assembly sequence was finely balanced to control stability of the assembly, this reduced interaction (which was not previously accounted for) would need to be a consideration for the redesign of the probes. The spacer between the protein binding part and DNA assembly sequence of the BINDA probes seemed unnecessarily long and allowed excess free movement. Some movement is required but this should be balanced against the need to bring the DNA sequences close together as shown in figure 3.1. These design revisions are taken into consideration in the recommended future work for this strand of the research.

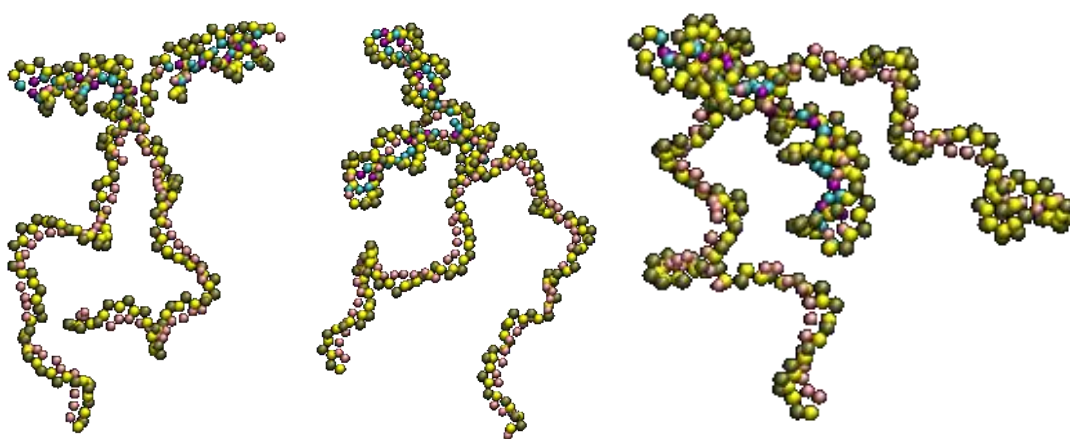


Figure 3.20: Three separate structures adopted by the BINDA assembly during equilibration time after assembly. The ends of the strands towards the bottom of the figure are the points where the DNA would be conjugated to its binding probe. Double stranded DNA that would form the nanoparticle attachment is shown towards the top of the images.

3.5 Conclusions

The BINDA assay format is one which has generated a large amount of interest in the literature. This work showed the first attempt to adapt the assay to a nanoparticle based assembly, in order to exploit the high sensitivities of this assay type. Due to experimental challenges, the systematic understanding of this has been expanded by developing a molecular dynamics model for understanding the process and thermodynamics of the assembly. This model should lead to rational design of probes and DNA sequences for BINDA, based on robust thermodynamic properties of the underlying structure. This will allow the reduction in material expenditure in developing a new assay, at the cost of a modest computational requirement for the simulation.

The 3SPN2 coarse grain simulation gave results that were as good at predicting trends in experimental results as atomistic simulations. The power of the model to predict

free energy changes after forming a regression model was only bettered by the completely empirical NN model. The reduced nature of the coarse grain model and Langevin solvent did not affect the quality of simulation results. This therefore reduces computational time and cost required.

The gains of the coarse grain model coupled with access to a computer cluster are stark; compared with the atomistic simulation and hardware used in literature which achieved around 39 ns of MD trajectory per day [32], the 3SPN2 model and computer cluster employed for this work achieved approximately 5,000,000 ns of MD trajectory per day. This work could therefore mark a significant move forward for future simulation work due to its greater efficiency, without a loss of data quality.

With the capability of the 3SPN2 model for determining thermodynamic properties established, it was prepared for use in further elucidating the BINDA assay. Initial analysis suggested that combining visual and numerical analysis would prove a powerful tool for the rational design of BINDA probes.

3.6 Future Work

The work shown here represents the first steps in the development of the computational model and allows this to lead the development of BINDA probes. Two strands to continue the progression exist. These are development of the computational and mechanistic understanding along with transferring of the current knowledge and model into practical work.

In keeping with the initial aim of the project, the established tools for understanding the BINDA assay should be employed to further progress the assay for use with nanoparticles. The current DNA probes should be redesigned based on the visual analysis, numerical analysis and experimental results. Initial visual analysis points towards reducing the spacing between the protein and DNA assembly and increasing the spacing between the nanoparticle assembly and DNA assembly. New probes

should then be tested by simulation and experiment. A comprehensive comparison of the predicted values of the new probes and the experimental performance would be useful, both to benchmark the utility of the 3SPN2 design and to further inform how the computer design can aid the BINDA development.

The second avenue for developing this project is further development of the computational tools. The benchmarking against experimental results here was based only on simple DNA duplexes. It would be useful to check the relevance of the 3SPN2 model for modelling of more complex structures such as mismatches and overlaps. Other works have related the free energy change to entropic and enthalpic contributions and also to the melting temperature. The former of these would further contribute to the thermodynamic understanding of the assembly and the latter would add to a more practically grounded understanding of the results from the simulations.

Further development of the computer model could employ the power of the simulation code to combine protein binding, DNA assembly and nanoparticle interactions. Including all these elements would comprehensively describe the assembly, through the combination of existing models in the literature. A further development could include plasmonic nanoparticle modelling, allowing the final experimental results to be simulated. This combination of modelling the biomolecular interaction and the physical properties of the nanoparticles would be substantial in scope but would lead to great improvements in understanding assays of this type.

3.7 Experimental

All simulations were run in series using Large-scale Atomic/Molecular Massively Parallel Simulator (LAMMPS) [35] and the 3 Sites per nucleotide.2 (3SPN2) [21] model on the ARCHIE-WEsT computer cluster. Python scripts for the entering of DNA strands and formatting input and outputs for the simulations were provided by David Palmer and modified as required. Scripts for the compilation and processing of data were written in Python. Scripts for the analysis of data were written in R.

The basic simulation was a coupled SMD simulation with the spring constant set at 7.8 kcal/ mol Å² and the constant velocity set at 0.000001 Å/ fs. A tether SMD was set at the centre of mass of the hybridised strand, fixed to the origin by a tether force of 50 kcal/ mol Å². The basic time step was 20 fs and outputs from the simulation were written to the output file every 2000 steps. Total simulation time was 10 μs, unless otherwise stated. The simulation parameters such as the entered DNA sequence, total number of steps or SMD velocity were altered as detailed in experiments in the main text. Simulation features such as time step and output steps were constant throughout the experiments.

Visual analysis was carried out using VMD software [36], which also allowed for distance and angle measurement where required.

DNA sequences modelled were as detailed below in table 3.7.

Table 3.7: DNA sequences used for each of the simulation experiments detailed in the main text

Experiment	DNA sequence
Initial setup/ number of simulations required for converging results	GGCGAACCAGGACGATTACT
Number of hybridising base pairs (10 base pair repeat)	CGGACGGTCT

unit)	
Changed pull point in SMD (10 base pair repeat unit)	CGGACGGTCT
Changing velocity drag gradient	CGGACGGTCTCGGACGGTCT
Simulated BINDA probes	TTTACACCAATCCTGAATGCG/ TACGAGTTGAGATGGTGTT

Full experimental and simulation results for the experimental dataset sequences are detailed in the supporting information tables of reference [32]. Only sequences of 8 base pairs or greater were extracted from this data source.

The most relevant data for the training and test sets is given below in table 3.8 and table 3.9.

Table 3.8: Free energy changes for all sequences in the training set.

Sequence	Free energy change (kcal / mol or arb unit for 3SPN2)					
	Experimental	NN	PBSA + shell	GBSA + shell	GBSA	3SPN2
AAAAAAAAA	-6.1	-5.8	-6	-9.1	-8.5	-0.0103
CGCTCAATACCCAGAA	-17.6	-18.3	-17.2	-23.4	-22.4	-0.0273

GTACGCCTTGATTCTC	-17.9	-18.2	-17.5	-23.5	-22.6	-0.0292
CAAAGAAAAG	-8.4	-8.2	-9.5	-12.7	-11.8	-0.0118
GGAACCTGATGC	-12.9	-12.9	-12.8	-17.1	-15.6	-0.0180
GAGACCAGAGTGATC	-15.6	-16.7	-15.9	-21.9	-20.6	-0.0271
GTATGACGGAAGTGGT	-18.6	-18.5	-16.8	-23.3	-21.7	-0.0292
CAAAGAAAAG	-7.3	-7.3	-9.4	-11.6	-11	-0.0096
CAAAGGAAAAG	-8.6	-9	-10.6	-13.5	-12.2	-0.0124
CAAATTAAG	-7.9	-7.3	-9	-11.8	-10.6	-0.0098
TCGATTAGGACACAGG	-18.2	-18	-16.4	-22.9	-22	-0.0271
GCGAAAAGCG	-11.8	-12.1	-11.9	-14.7	-14.5	-0.0144
CACTCTATGCCCGGCC	-19.2	-20.7	-19.9	-26	-24.8	-0.0296
CTAGAGCGGATGACTT	-18.2	-18.1	-17.4	-17.4	-21.7	-0.0317
CACTCTATGTCCCGGCC	-19.2	-19.7	-18.8	-25.2	-24.1	-0.0291
CAAACAAAG	-7.7	-7.6	-8.2	-10.6	-9.8	-0.0103
CAATCAAAG	-9	-8.3	-9.3	-12.4	-10.3	-0.0114
GGAACAAGATGC	-12.9	-12.9	-13.3	-17.4	-16.1	-0.0188
TAGGTTATAA	-6.8	-7.1	-7.6	-10.9	-11.8	-0.0101
GACTTTAGGAGCGATG	-18.2	-17.9	-17.4	-23.5	-22.5	-0.0303
GCCAGTTAA	-8.9	-8.6	-9.3	-12.1	-12	-0.0108
CAGAGTGATCGAGGC	-19.1	-18.1	-16.4	-22.3	-21.3	-0.0273
CAAAATAAAG	-7.6	-7.3	-12.1	-18.3	-10.8	-0.0099

GTCATATCCAGCGTTC	-18.9	-18.3	-17	-23.5	-22.2	-0.0307
CTTCCTTCCTTC	-13.2	-12.1	-14	-17.7	-16.6	-0.0179
AGCATTAGACGGACCT	-19.9	-18.7	-17.1	-23.9	-21.8	-0.0292
GGTCAGATACAC	-13	-12.5	-12.1	-16.7	-15.4	-0.0171
CAAACGAAAG	-9.5	-9.6	-10.5	-13.5	-13.1	-0.0145
ATAACTGGC	-8.8	-8.6	-9	-11.7	-12.1	-0.0095
GTTGCGGTCTTACATG	-18.5	-18.5	-17.3	-24.1	-22.3	-0.0299
CACTCTATGTCCGGTC	-19.5	-18.7	-17.7	-24.4	-23.2	-0.0289
GTCGTTACTGGGCTAT	-19.1	-18.3	-17.4	-24.5	-21.6	-0.0299
ACATTATTATTACA	-11.1	-11.1	-11	-16.4	-15.1	-0.0168
CACGACTATCTGAACC	-18.7	-18	-16.8	-23.3	-22	-0.0280
CAAATAAAAG	-7.5	-7.3	-9	-11.7	-10.5	-0.0096
GCATTCTGTACCTCGA	-18.2	-18.4	-17.4	-23.8	-22.7	-0.0284
CGCTGTTAC	-9.7	-9.6	-10	-12.8	-12.1	-0.0114
CGCTATGAACCACTTG	-18	-18.3	-16.9	-23.5	-21.7	-0.0283
CGAAATGCTAGTGACC	-19	-18.2	-16.8	-23.3	-21.7	-0.0288
GCGAATTCGC	-13.3	-12.2	-11.4	-14.4	-14.3	-0.0147
TTAGCAGAGTCCATCG	-18.3	-18.2	-14.8	-21.5	-21.3	-0.0290
CGCGAATTCGCG	-16.9	-16.3	-14	-18.2	-17.2	-0.0214
CAAAGAAAG	-8.1	-8.2	-10.1	-12.9	-11.6	-0.0115
GCATCAAGCAGCTCCAGGCA	-24.6	-25.9	-23.2	-31.7	-29.5	-0.0411

CTTGTA CTG	-8.7	-8.9	-9.7	-13	-13.1	-0.0124
CGCTCAATGCCCGGAA	-20.5	-20.9	-19.8	-25.7	-22	-0.0312
ACGTATTATGC	-10.4	-10.7	-10.9	-14.2	-14.3	-0.0136
ACCTGACGGAGACTAT	-17.3	-18.4	-17.8	-24.3	-21.7	-0.0311
GCTGAATGTCCTAG	-15.1	-15	-14.2	-19.4	-19.2	-0.0224
CAAAGCAAAG	-9.3	-9.4	-10.7	-13.5	-13.1	-0.0137
AGCTCCAGGC	-11.8	-12.1	-13.4	-16.4	-13.9	-0.0137
CTAAGGTCGTGTATCC	-17.8	-17.6	-15.4	-22	-23.2	-0.0303
CACCATTCAGAGCCTA	-18.6	-17.8	-16.8	-23.2	-21.5	-0.0290

Table 3.9: Free energy changes for all sequences in the test set.

Sequence	Free energy change (kcal / mol or arb unit for 3SPN2)					
	Experimental	NN	PBSA + shell	GBSA + shell	GBSA	3SPN2
CGGCAAGCGC	-13.3	-14	-13.2	-16.5	-14.9	-0.0172
ATTGGATACAAA	-10.1	-10.6	-10.4	-15.4	-13.5	-0.0160
CAAATAAAG	-6.5	-6.3	-8.5	-10.8	-9.4	-0.0078
CTCAAATGGTACGCAG	-18.3	-18.3	-17.5	-23.9	-22.1	-0.0299
CGATGTTCAGTCA	-15.8	-15.9	-14.3	-20.1	-18.5	-0.0232
GATGCCAGGTCGATAA	-18.7	-18.4	-16.7	-23.5	-21.7	-0.0302
GCGGTAAGGATCTAGT	-18.3	-18	-17.4	-23.7	-22.7	-0.0271

CCATTGCTACC	-12.2	-11.7	-12.7	-16.4	-15.6	-0.0152
CAAATAAGAG	-7.5	-7.9	-9.3	-12.2	-11.7	-0.0101
CGCTCAATGCCTGGAG	-18.1	-20.1	-19.3	-25.2	-23.8	-0.0291
GTCAACAGGCATAGCA	-18.4	-18.5	-17	-23.7	-22.3	-0.0294
CAAAACAAAG	-8.6	-8.5	-10	-13.1	-11.8	-0.0119
CAATTATAAG	-6.8	-6.9	-9.1	-11.8	-11	-0.0091
AAAAAAAAAA	-6.7	-6.7	-6.8	-9.3	-9.2	-0.0131
CAAACAAAAG	-8.7	-8.5	-10	-13	-11.4	-0.0118
ATGAGCTCAT	-10.4	-9.9	-8.9	-12.3	-11.9	-0.0142
CAACCAACCAAC	-13.8	-13	-13.5	-17.9	-17	-0.0180
CAACTAGAAG	-8.1	-8.6	-9.8	-12.9	-12.8	-0.0108
ATCTATCCG	-8.6	-8.4	-8.4	-11	-11.2	-0.0095
CAAAAAAAG	-7.2	-6.7	-8.7	-10.9	-10	-0.0088
CCATCGCTACC	-13.3	-12.8	-13	-16.8	-16.8	-0.0175
GACAGTAGCTCGGAAT	-18.7	-18.4	-17	-23.1	-21.1	-0.0305
CAAACCAAAG	-9.5	-9.3	-10.2	-13.4	-11.8	-0.0122
CATCCGAGTTTACAGC	-18.9	-18.2	-17.4	-23.6	-22.4	-0.0288
GACCTAGACACCATTC	-18.3	-17.5	-17	-23.7	-22.5	-0.0279
GACTTGTGGACGGTAT	-19	-18.5	-17.2	-23.7	-21.6	-0.0303

3.8 References

1. Zhang, H., X.-F. Li, and X.C. Le, *Binding-Induced DNA Assembly and Its Application to Yoctomole Detection of Proteins*. Analytical Chemistry, 2012. **84**(2): p. 877-884.
2. Zhang, H., et al., *Assembling DNA through Affinity Binding to Achieve Ultrasensitive Protein Detection*. Angewandte Chemie International Edition, 2013. **52**(41): p. 10698-10705.
3. Chen, J., et al., *Amplified binding-induced homogeneous assay through catalytic cycling of analyte for ultrasensitive protein detection*. Chemical Communications, 2016. **52**(9): p. 1816-1819.
4. Deng, B., J. Chen, and H. Zhang, *Assembly of Multiple DNA Components through Target Binding toward Homogeneous, Isothermally Amplified, and Specific Detection of Proteins*. Analytical Chemistry, 2014. **86**(14): p. 7009-7016.
5. Hu, J., et al., *A Reusable Electrochemical Proximity Assay for Highly Selective, Real-Time Protein Quantitation in Biological Matrices*. Journal of the American Chemical Society, 2014. **136**(23): p. 8467-8474.
6. Yang, L., et al., *Calibration of Silver Plasmon Rulers in the 1–25 nm Separation Range: Experimental Indications of Distinct Plasmon Coupling Regimes*. The Journal of Physical Chemistry C, 2010. **114**(11): p. 4901-4908.
7. Rivalta, I., et al., *Ab initio simulations of two-dimensional electronic spectra: The SOS//QM/MM approach*. International Journal of Quantum Chemistry, 2014. **114**(2): p. 85-93.
8. Šponer, J., et al., *Aromatic Base Stacking in DNA: From ab initio Calculations to Molecular Dynamics Simulations*. Journal of Biomolecular Structure and Dynamics, 2000. **17**(sup1): p. 1-24.
9. Heifets, E., E.A. Kotomin, and J. Maier, *Semi-empirical simulations of surface relaxation for perovskite titanates*. Surface Science, 2000. **462**(1–3): p. 19-35.
10. Galindo-Murillo, R., D.R. Roe, and T.E. Cheatham Iii, *Convergence and reproducibility in molecular dynamics simulations of the DNA duplex*

- d(GCACGAACGAACGAACGC)*. *Biochimica et Biophysica Acta (BBA) - General Subjects*, 2015. **1850**(5): p. 1041-1058.
11. Seibel, G.L., U.C. Singh, and P.A. Kollman, *A molecular dynamics simulation of double-helical B-DNA including counterions and water*. *Proceedings of the National Academy of Sciences of the United States of America*, 1985. **82**(19): p. 6537-6540.
 12. Pérez, A., F.J. Luque, and M. Orozco, *Frontiers in Molecular Dynamics Simulations of DNA*. *Accounts of Chemical Research*, 2012. **45**(2): p. 196-205.
 13. Swegat, W., et al., *MD Simulation of Protein-Ligand Interaction: Formation and Dissociation of an Insulin-Phenol Complex*. *Biophysical Journal*, 2003. **84**(3): p. 1493-1506.
 14. Han, J., R.H. Gee, and R.H. Boyd, *Glass Transition Temperatures of Polymers from Molecular Dynamics Simulations*. *Macromolecules*, 1994. **27**(26): p. 7781-7784.
 15. Adcock, S.A. and J.A. McCammon, *Molecular Dynamics: Survey of Methods for Simulating the Activity of Proteins*. *Chemical reviews*, 2006. **106**(5): p. 1589-1615.
 16. Chenoweth, K., A.C.T. van Duin, and W.A. Goddard, *ReaxFF Reactive Force Field for Molecular Dynamics Simulations of Hydrocarbon Oxidation*. *The Journal of Physical Chemistry A*, 2008. **112**(5): p. 1040-1053.
 17. Bond, P.J., et al., *Coarse-grained molecular dynamics simulations of membrane proteins and peptides*. *Journal of Structural Biology*, 2007. **157**(3): p. 593-605.
 18. Takada, S., *Coarse-grained molecular simulations of large biomolecules*. *Current Opinion in Structural Biology*, 2012. **22**(2): p. 130-137.
 19. Cheatham, I.T.E. and P.A. Kollma, *Observation of the A-DNA to B-DNA Transition During Unrestrained Molecular Dynamics in Aqueous Solution*. *Journal of Molecular Biology*, 1996. **259**(3): p. 434-444.
 20. Konrad, M.W. and J.I. Bolonick, *Molecular Dynamics Simulation of DNA Stretching Is Consistent with the Tension Observed for Extension and Strand*

- Separation and Predicts a Novel Ladder Structure*. Journal of the American Chemical Society, 1996. **118**(45): p. 10989-10994.
21. Hinckley, D.M., et al., *An experimentally-informed coarse-grained 3-site-per-nucleotide model of DNA: Structure, thermodynamics, and dynamics of hybridization*. The Journal of chemical physics, 2013. **139**(14): p. 144903.
 22. Potoyan, D.A., A. Savelyev, and G.A. Papoian, *Recent successes in coarse-grained modeling of DNA*. Wiley Interdisciplinary Reviews: Computational Molecular Science, 2013. **3**(1): p. 69-83.
 23. Palmer, D.S., et al., *First-principles calculation of the intrinsic aqueous solubility of crystalline druglike molecules*. Journal of chemical theory and computation, 2012. **8**(9): p. 3322-3337.
 24. Ramachandran, G. and T. Schlick, *Solvent effects on supercoiled DNA dynamics explored by Langevin dynamics simulations*. Physical Review E, 1995. **51**(6): p. 6188-6203.
 25. Zhu, J., Y. Shi, and H. Liu, *Parametrization of a Generalized Born/Solvent-Accessible Surface Area Model and Applications to the Simulation of Protein Dynamics*. The Journal of Physical Chemistry B, 2002. **106**(18): p. 4844-4853.
 26. Homeyer, N. and H. Gohlke, *Free Energy Calculations by the Molecular Mechanics Poisson–Boltzmann Surface Area Method*. Molecular Informatics, 2012. **31**(2): p. 114-122.
 27. Jarzynski, C., *Nonequilibrium Equality for Free Energy Differences*. Physical Review Letters, 1997. **78**(14): p. 2690-2693.
 28. Park, S., et al., *Free energy calculation from steered molecular dynamics simulations using Jarzynski's equality*. The Journal of chemical physics, 2003. **119**(6): p. 3559-3566.
 29. Baştuğ, T., et al., *Potential of mean force calculations of ligand binding to ion channels from Jarzynski's equality and umbrella sampling*. The Journal of chemical physics, 2008. **128**(15): p. 155104.
 30. Liphardt, J., et al., *Equilibrium information from nonequilibrium measurements in an experimental test of Jarzynski's equality*. Science, 2002.

- 296**(5574): p. 1832-1835.
31. Douarche, F., et al., *An experimental test of the Jarzynski equality in a mechanical experiment*. EPL (Europhysics Letters), 2005. **70**(5): p. 593.
 32. Lomzov, A.A., Y.N. Vorobjev, and D.V. Pyshnyi, *Evaluation of the Gibbs Free Energy Changes and Melting Temperatures of DNA/DNA Duplexes Using Hybridization Enthalpy Calculated by Molecular Dynamics Simulation*. The Journal of Physical Chemistry B, 2015. **119**(49): p. 15221-15234.
 33. Mosayebi, M., et al., *Force-Induced Rupture of a DNA Duplex: From Fundamentals to Force Sensors*. ACS Nano, 2015. **9**(12): p. 11993-12003.
 34. Neumann, J. and K.-E. Gottschalk, *The Effect of Different Force Applications on the Protein-Protein Complex Barnase-Barstar*. Biophysical Journal. **97**(6): p. 1687-1699.
 35. Plimpton, S., *Fast parallel algorithms for short-range molecular dynamics*. Journal of computational physics, 1995. **117**(1): p. 1-19.
 36. Humphrey, W., A. Dalke, and K. Schulten, *VMD: visual molecular dynamics*. Journal of molecular graphics, 1996. **14**(1): p. 33-38.